The Dissertation Committee for David de Jesus Medellin Salas
certifies that this is the approved version of the following dissertation:

Towards the creation of high-fidelity Fock states of neutral atoms

Committee:

Mark G. Raizen, Supervisor

Alexander Demkov

Gregory Fiete

Ila Fiete

George Shubeita

Towards the creation of high-fidelity Fock states of neutral atoms

by

David de Jesus Medellin Salas, LIC.

DISSERTATION

Presented to the Faculty of the Graduate School of

The University of Texas at Austin

in Partial Fulfillment

of the Requirements

for the Degree of

DOCTOR OF PHILOSOPHY

THE UNIVERSITY OF TEXAS AT AUSTIN

August 2013

A mi papá, mi mamá, Kimberly, Brenda, y Daniel.

Acknowledgments

First, I would like to thank my advisor Mark Raizen for the opportunity to work in his group under his guidance during my Ph.D. Mark comes up with novel and interesting ideas all the time and the enthusiasm with which he approaches physics is contagious and very motivating. This enthusiasm reflects in the group, which I found from the very beginning to be very friendly, motivated, and hard working. It has been a great pleasure and privilege to work in his group.

When I came to the lab, I started working on the sodium Bose-Einstein condensate experiment, under the guidance of Hrishikesh Kelkar and Tongcang Li. Hrishi and Tongcang were my first mentors and I learned most of my basic laboratory skills from them. Hrishi taught me lots of electronics, vacuum, optics, and that sometimes all you need to solve problems is to be patient. Tongcang is a brilliant experimentalist and theorist. He was constantly coming up with very innovative ways of solving problems. With him, I learned that sometimes you really need to think outside the box to solve problems. After work, the three of us would usually go and have dinner at Pho's or Chipotle and talk about life, science, politics, and other stuff. Hrishi was convinced that I was a theorist that somehow ended up in an experimental group. I think I have proven him wrong since now I like applied physics better than theoretical physics! Although I am sure he would say that in my heart I will always be a theorist! I am thankful to them for being my first mentors and being patient with me in my first years. Both of them are exceptional physicists, and I'm sure I will hear more from them in the years to come.

In summer 2009 I started working on the lithium-6 experiment with Gabriel Price and Kirsten Viering. Jianyong Mo joined the experiment in August 2009. Gabriel is extremely organized and very hard working, and under his leadership, the experiment made very fast progress. Gabriel has exceptional machining skills and I never stopped learning from him. After Gabriel left, Kirsten took the lead on the experiment. Kirsten

proved to be an exceptional leader. She is very hard working and her extensive knowledge of vacuum, lasers, and optics was critical when we were assembling the experiment. Jianyong is very hard working and very quickly became an invaluable member of our team. Every time I had an idea, I would discuss it with him and he would almost always point out something I was missing. Both Kirsten and Jianyong are very fine experimentalists, and I thank them for everything I learned from them.

In fall 2012, Felix Schmidt joined the lithium-6 experiment for a brief period of time. Felix is a young and talented experimentalist from whom I expect many great things. Not only were we coworkers but we also became good friends. I wish him the best.

I also want to thank Adam Libson for helping us assemble the Lithium experiment and all his advice on vacuum, physics, and other subjects. He was always very friendly and willing to help and his general knowledge on almost every subject is impressive. I also thank him for teaching me his secret bowling technique and the basics of rock climbing.

I would like to thank Tom Mazur, Jamie Gardner, Simon Kheifets, Jianyong Mo, and Allyson Rice for taking time to proofread my thesis. I also want to thank other members and former members of the Raizen lab that made it a fun place to work: Ed Narevicius, Max Riedel, Christian Parthey, Cristoph Shaeff, Travis Bannerman, Isaac Chavez, Melissa Jerkins, Charlotte Sanders, Julia Majors, Geneva White, Maria Becker, Rob Clark, Shoupu Wan, Akarsh Simha, Bruce Klappauf, Rodrigo Castillo Garza, Kevin Melin, Camilo Perez, Sagi Zisman, Tharon Morrison, Willam Watson, Daniel Raimi-Zlatic, and Nick Bhattacharya.

A special thanks goes to the administrative staff of the Center for Nonlinear Dynamics, Olga Vera, Rachael Salge, Marybeth Casias, and Elena Simmons, for dealing with all the University's bureaucracy and allowing us to focus on research. I also thank our machine shop and cryo shop staff, Allan Shroeder, Jack Clifford, Lanny Sandefur, and Ed Baez, for all their support.

Quiero tambien agradecer a mi familia por todo el apoyo que me brindaron du-

rante todos estos años. A mis padres por haberme dado una buena educación y un hogar lleno de amor. Si he podido llegar tan lejos, es porque me he parado sobre los hombros de mis padres. Quiero tambien agradecer a mis hermanas Kimberly y Brenda, y a mi hermano Daniel, por su amor y apoyo incondicional.

I wish to thank Prof. Sergio Mejía, Prof. Rubén Morones, and Prof. Jesus Rivero at UANL for believing in me and all their advice.

Life outside the lab wouldn't have been the same without Alan Dávila, Ignacio Gallardo, Wilberth Herrera, Erick Leuro, and Rafael Longoria. Our discussions on almost any topic were long and epic. I learned a lot from every one of them and for that I am thankful.

A very special thanks goes to Allyson Rice. Allyson made the last year of my Ph.D. the happiest of all. I am very grateful to her for all the motivation and love she has given me. I'm looking forward to spending much more time with her.

Austin, TX

David Medellin

Towards the creation of high-fidelity Fock states of neutral atoms

David de Jesus Medellin Salas, Ph.D.
The University of Texas at Austin, 2013

Supervisor: Mark G. Raizen

This dissertation presents the implementation of a technique to generate atomic Fock states of Lithium 6 with ultra-high fidelity, called laser culling. Fock states, atomic states with a definite number of particles, are a mandatory step for studying few-body quantum phenomena such as quantum tunneling, quantum entanglement, and serve as building blocks for quantum simulators. The creation of ultra-high fidelity Fock states begins with a degenerate Fermi gas in an optical dipole trap. Being fermions, lithium-6 atoms fill the energy levels of the dipole trap with 2 atoms per energy level. Introducing a magnetic field gradient creates a linear potential that tilts the potential produced by the optical dipole trap. The initially bound energy levels become quasi-bound states, each with a different lifetime. By exploiting the difference between these lifetimes, one can generate a single pair of atoms in the ground state of the trap with fidelities that can exceed 99.9%. This dissertation first presents the details of the design and construction of an apparatus for laser culling, and then reports on the progress made towards the creation of atomic Fock states with ultra-high fidelity.

Table of Contents

List of Tables

List of Figures

Part I

Background and Theory

Chapter 1

Quantum Simulation

1.1 Introduction

In our quest to understand nature, we have invented physical theories that describe matter, energy, space, and time. Knowing these laws, however, does not always allow us to make analytic predictions of the behavior of nature. In Newtonian mechanics, for example, the three-body problem does not have a general analytic solution. The solution must be either approximated or calculated numerically. Sometimes, even an approximation is not possible, and the only option is a numerical calculation.

Just as we have built machines that do physical work, we have built machines that can perform computations faster and with more precision than us. The most famous ancient analog computer designed to calculate astronomical positions, the Antikythera mechanism [1], appeared as early as the 1st century B.C. As technology progressed, computers evolved from simple gear mechanisms, to mechanical integrators, to powerful digital electronic computers capable of simulating the weather and the evolution of galaxies.

However, all these computers are classical in nature, and as Richard Feynman pointed out at the end of his keynote speech "Simulating Physics with Computers",

"*Nature isn't classical, dammit, and if you want to make a simulation of nature, you'd better make it quantum mechanical, and by golly it's a wonderful problem, because it doesn't look easy.*"

Quantum mechanics allows us to understand matter at its most fundamental level and opens the possibility for new technologies. At the same time, it poses new challenges to our computation capabilities. Many important problems in physics, especially low temperature physics, remain poorly understood because the computational requirements

demanded by the underlying theory are very complex and vast. Classical computers, even the most powerful supercomputers, are inadequate for simulating quantum systems with as few as 32 particles [2].

The inadequacy of classical computers for quantum mechanical simulations stems from the fact that the necessary resources needed to simulate a quantum system scale exponentially with the system's size. For example, it takes 2^N complex numbers to specify the wavefunction of an arbitrary state of N spin-1/2 particles. If we were to store a single complex number in each baryon of the universe, we could store at most 10^{80} complex numbers. The maximum number of spin-1/2 particles whose wavefunction we can represent with 10^{80} complex numbers is approximately 265 ($2^{265} \approx 10^{80}$). Using the entire universe as our memory module, we can only afford to write the wavefunction of a 265 spin-1/2 particle system! Clearly, if progress is to be made, a quantum computer must be used to simulate quantum systems.

Although in the past years progress has been made in building quantum simulators and computers, the main question still remains: What is the best system to realize a quantum computer? The quest for a scalable quantum computer has led to the development of several competing platforms and physical realizations [3–6]. The challenge is to simultaneously satisfy a number of conditions, known as the five DiVicenzo criteria [7] :

1. Be a scalable physical system with well-defined qubits.
2. Be initializable to a simple fiducial state
3. Have long enough decoherence times.
4. Have a universal set of quantum gates.
5. Permit high quantum efficiency, qubit-specific measurements.

Although not stated explicitly, it is also assumed that each step must be done at ultra-high fidelity.

This dissertation presents a system that can potentially satisfy all the DiVicenzo criteria, and maintain ultra-high fidelity; however, the main emphasis will be the preparation of a simple fiducial state, with the fiducial state being a Fock state of lithium-6 atoms in the ground state of an optical dipole trap.

The creation of Fock states with ultra-high fidelity begins with a degenerate Fermi gas in an optical dipole trap. Being fermions, lithium-6 atoms fill the energy levels of the dipole trap with two atoms per energy level. Introducing a magnetic field gradient creates a linear potential that tilts the potential produced by the optical dipole trap. The initially bound energy levels become quasi-bound states, each with a different lifetime. By exploiting the difference between these lifetimes, one can generate a single pair of atoms in the ground state of the trap with fidelities that can exceed 99.9%. This dissertation first presents the details of the design and construction of an apparatus for laser culling, and then reports on the progress made towards the creation of atomic Fock states with ultra-high fidelity .

Chapter 2

Atomic Physics for Lithium 6

This chapter serves both as review of the atomic physics topics relevant for this thesis, and to introduce the notation that will be used.

2.1 Physical Properties of Lithium 6

Lithium, from the Greek lithos ($\lambda\acute{\iota}\theta o\zeta$), meaning "stone", is the lightest metal of the periodic table. It has three electrons, two in the inner closed shell ($1s^2$), and one valence electron ($2s^1$). Some relevant physical properties of lithium are summarized in table 2.1:

Property	Symbol	Value	Reference
Density (300 K)	ρ	0.534 g$\cdot$ cm^{-3}	[8]
Melting Point	T_M	453.69 K 180.54 °C	[8]
Boiling Point	T_B	1615 K 1341.85 °C	[8]

Table 2.1: Physical properties of Lithium

The starting point of most cold atom experiments is an effusive beam of the atom under study. The vapor pressures of solid and liquid lithium as a function of temperature are given by [9]:

$$\log_{10} P_{V_{sol}} = -54.87864 - \frac{6450.944}{T} - 0.01487480T + 24.82251 \log_{10} T \quad (2.1)$$

$$\log_{10} P_{V_{liq}} = 10.34540 - \frac{8345.574}{T} - 0.00008840T - 0.68106 \log_{10} T \quad (2.2)$$

At 350 °C (623 K), we obtain a high enough vapor pressure (10^{-5} torr) to load around 10^8 atoms in a few seconds; we can operate the oven at this temperature for about 4

years before depleting the lithium reservoir. The spectroscopy cell runs at 420 °C (693 K), but since it is closed it doesn't run out of lithium and can be run almost indefinitely. Figure 2.1 shows a plot of the vapor pressure of liquid lithium versus temperature.

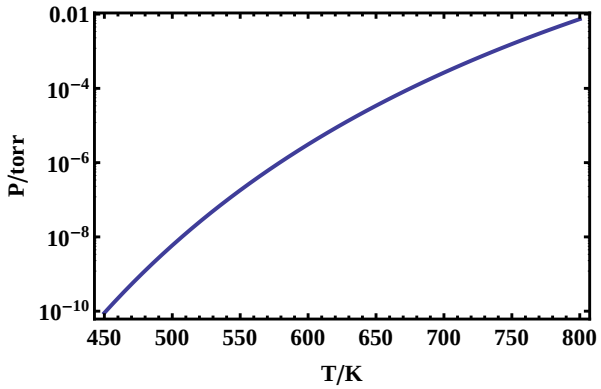

Figure 2.1: Vapor pressure of lithium as function of temperature. *Figure courtesy of Kirsten Viering.*

2.2 Atomic Structure of Lithium 6

There are two stable isotopes of lithium: ^{6}Li and ^{7}Li. The work of this thesis was made with ^{6}Li, so from now on all references to lithium will refer to ^{6}Li. Since the natural abundance of ^{6}Li is only 7.6%, it must be enriched before we use it. We use 95% enriched lithium 6 from Sigma-Aldrich and Medical Isotopes Inc. Table 2.1 summarizes some relevant properties of ^{6}Li,

Property	Symbol	Value	Reference
Atomic numer	Z	3	
Nucleons	Z+N	6	
Natural abundance	η	7.6%	[8]
Nuclear lifetime	τ_n	stable	[8]
Atomic mass	m	6.015 121 4 u 9.988 341 4 $\times 10^{-25}$ kg	[10]
Nuclear spin	I	1	
Electronic spin	S	1/2	

Table 2.2: Atomic Properties of ^{6}Li

Being an alkali metal, ^{6}Li has a single valence electron. Its ground state configuration, $1s^2 2s^1$, has one electron in an s orbital with zero angular momentum. Its spectroscopic notation is ^{2}S. The excited state configuration, $1s^2 2p^1$, has one electron in a p orbital with angular momentum one. Its spectroscopic notation is ^{2}P. The simplest way to describe the energy levels of lithium is to use the central potential approximation. In this approximation, the potential felt by the electron is assumed to be spherically symmetric, and takes into account the charge of the nucleus and the electrons in the inner shell.

In hydrogenic atoms, for which all electrons but one have been ripped off, the gross energy depends only on the quantum number n. This means that the states 2s and 2p will have the same energy. This is not true for atoms with more than one electron, since the electronic wave functions will interact with the inner electrons in different ways: s electrons will penetrate inside the core and "see" more nuclear charge than electrons with higher l. Thus, charge screening by the inner core electrons is more effective the farther away the electron moves, i.e. the higher the value of l. This changes the absolute energies of the 2s and 2p states and destroys the degeneracy between these two states, making the 2s state a ground state and the 2p state an excited state. The transition between these two states gives rise to lithium's D line. The energy of each state can be approximated by a modification to Bohr's formula:

$$E = -\frac{hc}{n^{*2}} R_\infty \tag{2.3}$$

where R_∞ is Rydberg's constant and n^* is an effective principal quantum number of the transition. n^* differs from the original n by $n^* = n - \delta_l$, where δ_l is called the ***quantum defect***. For the 2s and 2p states of lithium, $\delta_S = 0.412$, and $\delta_P = 0.041$. $\delta_l = 0$ for $l > 2$. Using equation (2.3) we can calculate the gross energy splitting between the ^2S and the ^2P state, $\lambda_D = 670.1$ nm, which is very close to the actual experimental value $\lambda_D = 670.98$ nm.

In addition to this energy splitting, we must consider the fine structure splitting. Any charge with angular momentum will give rise to a magnetic moment. The electron has an intrinsic angular momentum, $\hat{\mathbf{S}}$, that will produce a magnetic moment. It also has

an orbital angular momentum, $\hat{\mathbf{L}}$, that will give rise to a second magnetic moment. The interaction between the spin and orbital magnetic moments gives rise to the spin-orbit coupling Hamiltonian , that can be written as,

$$\hat{\mathbf{H}}_{\text{S-O}} = (g_s - 1)\frac{1}{2m_e^2c^2\hbar^2}\left(\frac{1}{r}\frac{\partial V(r)}{\partial r}\right)\hat{\mathbf{S}}\cdot\hat{\mathbf{L}} \tag{2.4}$$

with $g_s - 1 \approx 1$

$$\hat{\mathbf{H}}_{\text{S-O}} = \frac{1}{2m_e^2c^2\hbar^2}\left(\frac{1}{r}\frac{\partial V(r)}{\partial r}\right)\hat{\mathbf{S}}\cdot\hat{\mathbf{L}} \tag{2.5}$$

where $\hat{\mathbf{L}}$ and $\hat{\mathbf{S}}$ are the orbital angular momentum and spin operators, respectively, and $V(r)$ is the electric potential produced by the nucleus and the inner electrons. In the absence of strong external magnetic or electric fields, $\hat{\mathbf{L}}$ and $\hat{\mathbf{S}}$ couple to form:

$$\hat{\mathbf{J}} = \hat{\mathbf{L}} + \hat{\mathbf{S}} \tag{2.6}$$

where

$$|L - S| \leq J \leq |L + S| \tag{2.7}$$

The spin-orbit coupling gives rise to the fine structure splitting in the ^2P excited state, which is 10.053044 GHz for ^{6}Li [11]. The transition $^2S_{1/2} \leftrightarrow {}^2P_{1/2}$ is known as the D_1 line, while the transition $^2S_{1/2} \leftrightarrow {}^2P_{3/2}$ is known as the D_2 line.

The excited states further split due to the much weaker hyperfine structure interaction. The hyperfine interaction arises from the interaction between the electron and the atomic nucleus. The hyperfine Hamiltonian can be written as,

$$\hat{\mathbf{H}}_{HF} = -\hat{\mu}\cdot\hat{\mathbf{B}}(0) + \frac{1}{6}e\sum_{\alpha\beta}\hat{Q}_{\alpha\beta}\frac{\partial^2\phi(0)}{\partial x_\alpha \partial x_\beta} \tag{2.8}$$

where $\hat{\mu}$ and $\hat{Q}$ are the nuclear magnetic dipole moment and nuclear electric quadrupole moment operators respectively. $\hat{\mathbf{B}}$ is the magnetic field operator at the location of the nucleus, and ϕ is the electric potential at the nucleus. The first term is analogous to the spin-orbit coupling. The second term gives a non-zero contribution only for the $2^2P_{3/2}$ state. As with the fine interaction, in the absence of strong external fields, $\hat{\mathbf{J}}$ and $\hat{\mathbf{I}}$ couple to form

$$\hat{\mathbf{F}} = \hat{\mathbf{J}} + \hat{\mathbf{I}} \tag{2.9}$$

with

$$|J - I| \leq F \leq |J + I| \tag{2.10}$$

In the $\hat{\mathbf{F}}$ basis, the hyperfine splitting energy is given by,

$$\Delta E_{HF} = \frac{1}{2}AC + \frac{3}{8}B\frac{C(C+1)}{I(2I-1)J(2J-1)} \tag{2.11}$$

where $C = F(F+1) - J(J+1) - I(I+1)$, and A and B are the *magnetic dipole hyperfine constant* and the *electric quadrupole hyperfine constant*, respectively for the F state of interest. Table 2.3 and 2.4 summarize some relevant optical properties of the ^{6}Li D_1 and D_2 line. Table 2.5 contains the values of the hyperfine constants for the 2S and 2P levels of lithium. Figure 2.2 illustrates the fine and hyperfine splitting of the ground and 2P excited states of ^{6}Li .

Property	Symbol	Value	Reference
Wavelength (vacuum)	λ	670.992 421 nm	[12]
Wavenumber (vacuum)	$k/2\pi$	14 903.298 cm^{-1}	[13]
Frequency	ν	446.789 634 THz	[12]
Lifetime	τ	27.102 ns	[14]
Natural linewidth	γ	$36.898\times10^6\text{s}^{-1}$	[12]
$\gamma = 2\pi\Gamma$	Γ	5.8724 MHz	
Atomic tecoil velocity	v_{rec}	9.886 554 cm·sec^{-1}	[12]
Recoil temperature	T_{rec}	3.535 652 56 μK	[12]

Table 2.3: Optical Properties of the ^{6}Li D_1 line

2.3 Interaction With Static Magnetic Fields

2.3.1 Zeeman Effect

As we saw in the previous section, a charge possessing any kind of angular momentum acts like a magnetic dipole, and it will interact with other dipoles and any external magnetic field. The shift of the energy levels of the atom due to its interaction with external magnetic fields is known as the ***Zeeman effect***. For a static magnetic

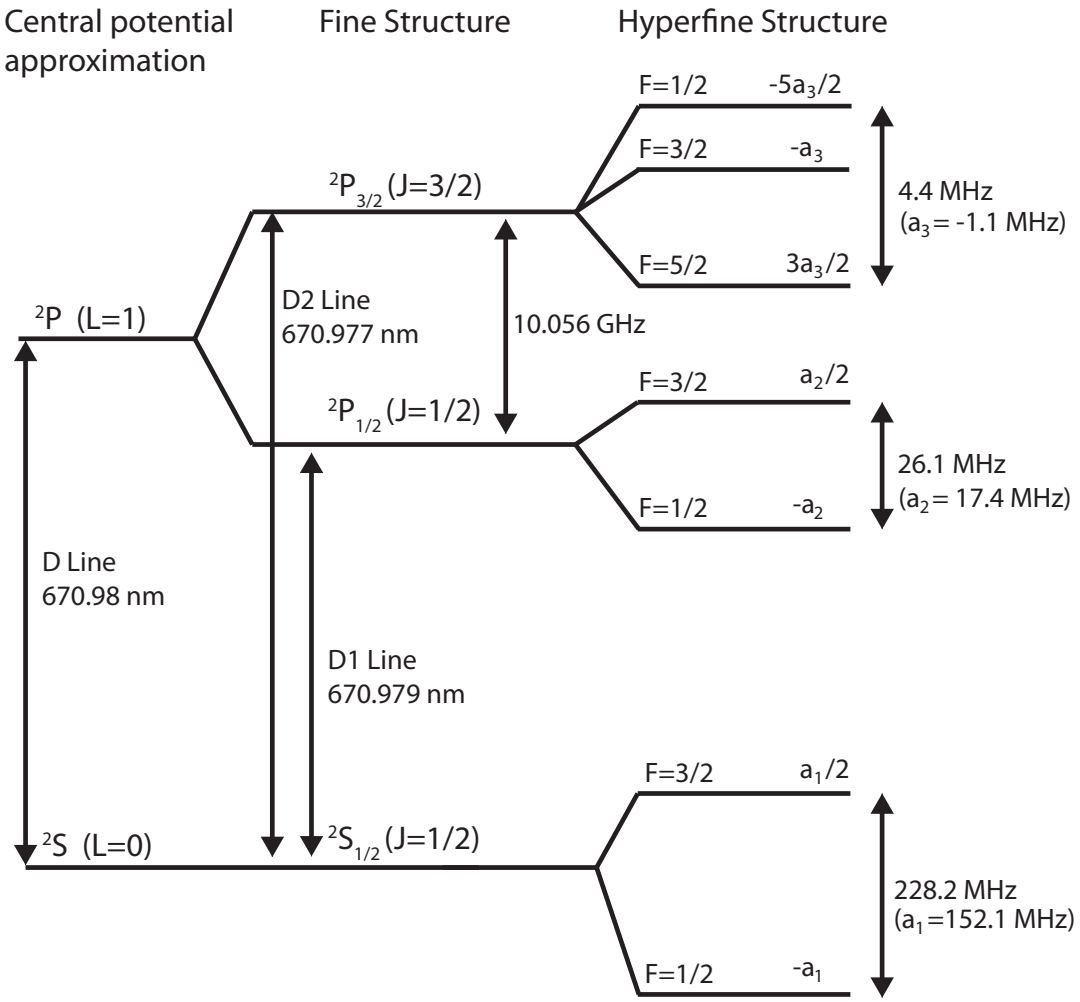

Figure 2.2: ^{6}Li energy level structure

Property	Symbol	Value	Reference
Wavelength (vacuum)	λ	670.977 338 nm	[12]
Wavenumber (vacuum)	$k/2\pi$	14 903.633 cm^{-1}	[13]
Frequency	ν	446.799 677 THz	[12]
Lifetime	τ	27.102 ns	[14]
Natural linewidth	γ	$36.898\times10^{6}\text{s}^{-1}$	[12]
$\gamma = 2\pi\Gamma$	Γ	5.8724 MHz	
Atomic recoil velocity	v_{rec}	9.886 776 cm·sec^{-1}	[12]
Recoil temperature	T_{rec}	3.535 811 52 μK	[12]

Table 2.4: Optical Properties of the ^{6}Li D_2 line

Property	Symbol	Value	Reference
$2^2S_{1/2}$ Magnetic dipole constant	$A_{2^2S_{1/2}}$	152.136 840 7 MHz	[15]
$2^2P_{1/2}$ Magnetic dipole constant	$A_{2^2P_{1/2}}$	17.386 MHz	[11]
$2^2P_{3/2}$ Magnetic dipole constant	$A_{2^2P_{3/2}}$	-1.155 MHz	[15]
$2^2P_{3/2}$ Electric quadrupole constant	$B_{2^2P_{3/2}}$	-0.10 MHz	[15]

Table 2.5: Hyperfine constants for the 2S and 2P levels of ^{6}Li

field, the interaction can be written as,

$$\begin{aligned} \hat{H}_B &= \frac{\mu_B}{\hbar}\left(g_S\hat{\mathbf{S}} + g_L\hat{\mathbf{L}} + g_I\hat{\mathbf{I}}\right)\cdot\mathbf{B} \\ &= \frac{\mu_B}{\hbar}\left(g_S\hat{S}_z + g_L\hat{L}_z + g_I\hat{I}_z\right)B_z \end{aligned} \tag{2.12}$$

where g_S, g_L, and g_I are the electron spin, electron orbital, and nuclear Landé g-factors respectively. When the interaction energy with the external field is much less than the fine structure splitting, the influence that $\hat{\mathbf{L}}$ and $\hat{\mathbf{S}}$ have on each other is stronger than that of the magnetic field; they couple to form a new quantum number $\hat{\mathbf{J}} = \hat{\mathbf{L}} + \hat{\mathbf{S}}$. For lithium-6, this means that $\hat{\mathbf{J}}$ is a good quantum number for fields much smaller than,

$$B \approx \frac{h}{\mu_B}\Delta E_{FS} = 7180\,\text{G} \tag{2.13}$$

For B $\ll$ 7180 G, the Hamiltonian then takes the form

$$\begin{aligned} \hat{H}_B &= \frac{\mu_B}{\hbar}\left(g_J\hat{\mathbf{J}} + g_I\hat{\mathbf{I}}\right)\cdot\mathbf{B} \\ &= \frac{\mu_B}{\hbar}\left(g_J\hat{J}_z + g_I\hat{I}_z\right)B_z \end{aligned} \tag{2.14}$$

where g_J is the total electronic Landé g-factor, given by

$$\begin{aligned} g_J &= g_L \frac{J(J+1) - S(S+1) + L(L+1)}{2J(J+1)} + g_S \frac{J(J+1) + S(S+1) - L(L+1)}{2J(J+1)} \\ &\approx 1 + \frac{J(J+1) + S(S+1) - L(L+1)}{2J(J+1)} \end{aligned} \tag{2.15}$$

where the values $g_L \approx 1$ and $g_S \approx 2$ have been used. $\hat{\mathbf{J}}$ starts to break up for fields of around 1000 G.

If the interaction with the external magnetic field is much smaller than the hyperfine structure energy splitting, then $\hat{\mathbf{I}}$ will couple with $\hat{\mathbf{J}}$ to form $\hat{\mathbf{F}} = \hat{\mathbf{I}} + \hat{\mathbf{J}}$, and the Hamiltonian takes then the simple form,

$$\begin{aligned} \hat{H}_B &= \frac{\mu_B}{\hbar} g_F \hat{\mathbf{F}} \cdot \mathbf{B} \\ &= \frac{\mu_B}{\hbar} g_F \hat{F}_z B_z. \end{aligned} \tag{2.16}$$

Where g_F is a Landé g-factor that contains contributions from both g_I and g_J, and it is given by,

$$\begin{aligned} g_F &= g_J \frac{F(F+1) - I(I+1) + J(J+1)}{2F(F+1)} + g_I \frac{F(F+1) + I(I+1) - J(J+1)}{2F(F+1)} \\ &\approx g_J \frac{F(F+1) - I(I+1) + J(J+1)}{2F(F+1)}. \end{aligned} \tag{2.17}$$

The second expression ignores the nuclear term, whose contribution is at a level of 0.1%. Table 2.6 summarizes the g-factors and the fine splitting energy of lithium-6.

Property	Symbol	Value	Reference
2P Fine Structure Splitting	ΔE_{FS}	10.053 044 GHz	[11]
Electron Spin g-Factor	g_S	2.002 319 304 373 7	[16]
Electron $L = 1$ Orbital g-factor	g_L	0.999 9995 87	[12]
Total Electronic g-factor	g_J $(2^2S_{1/2})$	2.002 301 0	[15]
	g_J $(2^2P_{1/2})$	0.666 8	[15]
	g_J $(2^2P_{3/2})$	1.335	[15]
Total Nuclear g-factor	g_I	-0.000 447 654 0	[15]

Table 2.6: g-factors and fine structure splitting for lithium-6

Unfortunately, the hyperfine energy splitting of lithium-6 are small: 228.2 MHz for the $2^2S_{1/2}$ ground state, 26.1 MHz for the $2^2P_{1/2}$ excited state, and 4.4 MHz for the $2^2P_{3/2}$ excited state. This means that $\hat{\mathbf{F}}$ is a good quantum number for fields much smaller than 163 G for the $2^2S_{1/2}$ ground state, 19 G for the $2^2P_{1/2}$ excited state, and 3 G for the $2^2P_{3/2}$ excited state. Since the transition we use is the ${}^2S_{1/2} \leftrightarrow {}^2P_{3/2}$ transition, we need to use the full Hamiltonian for fields as small as a few gauss. In general, diagonalizing the full Hamiltonian is not a trivial task, but when there is only one valence electron, the Breit-Rabi formula can be applied. The Zeeman splitting for the ground state ${}^2S_{1/2}$ is shown in figure 2.3. At high fields, the two lowest states of the ground state ${}^2S_{1/2}$ are high-field seekers. Since only low-field seekers can be trapped in magnetic traps, lithium-6 cannot be magnetically trapped and optical traps must be used.

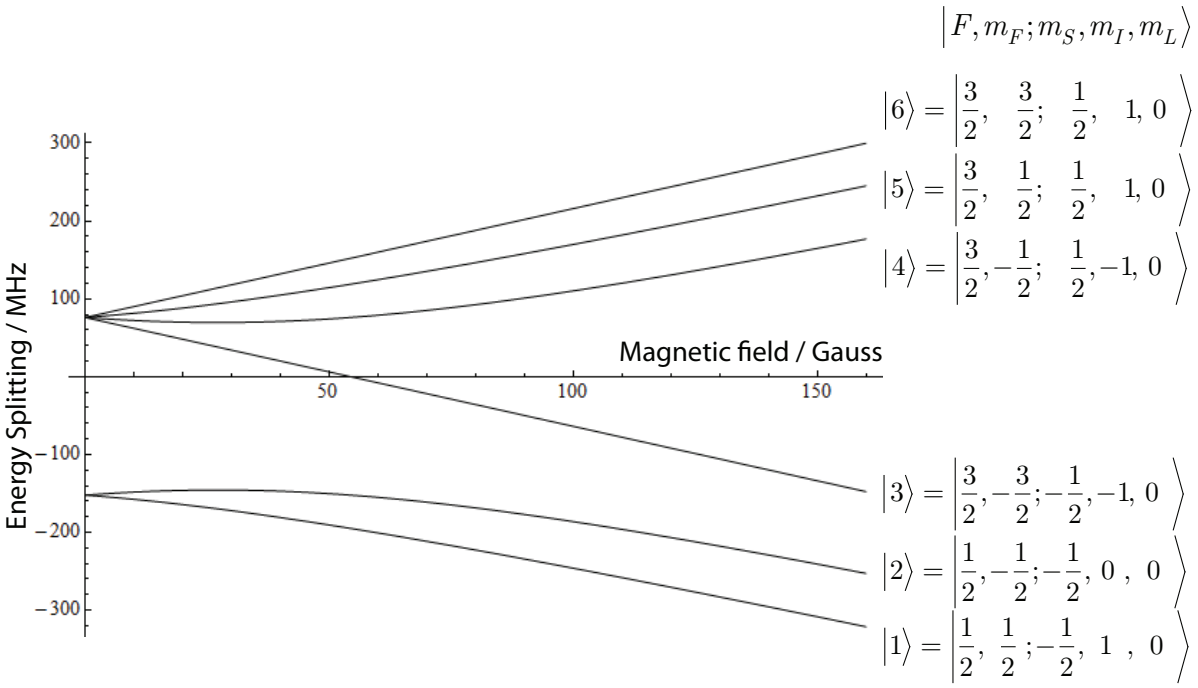

Figure 2.3: Zeeman splitting for the ground state ${}^2\mathrm{S}_{1/2}$ of lithium-6. Notice how $\hat{\mathbf{F}}$ stops being a good quantum number around 20 G

2.3.2 Feshbach Resonances

Feshbach resonances allow us to control the scattering length between lithium's atomic states. This has several advantages: by tuning the scattering length to zero, we can make a non-interacting sample of atoms; and by making the scattering length very large, we can make evaporative cooling much more efficient. For a more detailed treatment of Feshbach resonances, see reference [17]

Consider two molecular potentials: $V_{bg}(r)$ and $V_C(r)$ (see figure 2.4) . $V_{bg}(r)$ represents the potential between two free atoms in the ultracold gas. For a very low energy collision with energy E, $V_{bg}(r)$ represents the energetically open channel. $V_C(r)$, on the other hand, represents the potential between two bound atoms and can support a bound state near the threshold of the open channel. $V_C(r)$is called the closed channel potential.

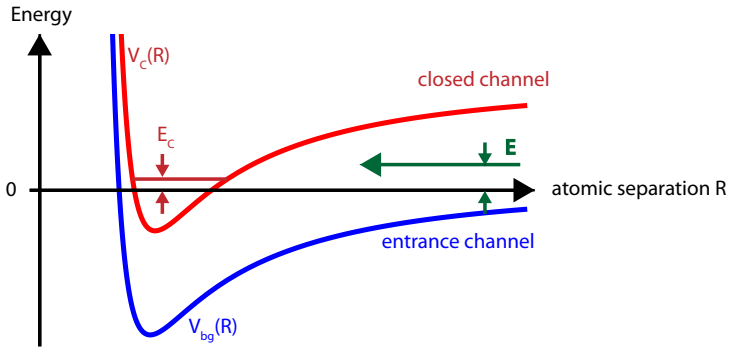

Figure 2.4: Feshbach Resonance Potentials. *Figure courtesy of Kirsten Viering.*

A Feshach resonance occurs when then bound molecular state energy of the closed channel approaches the free atom energy of the open channel. When this happens, even weak coupling between the two molecular states can lead to a strong mixing between the two potentials. The energy difference between the two channels can be controlled magnetically if they have different magnetic moments. This leads to a magnetically tuned Feshbach resonance. For low energy collisions, only the s-wave scattering length is important. A Feshbach resonance changes the scattering length as

$$a(B) = a_0 \left(1 - \frac{\Delta}{B - B_0}\right) \tag{2.18}$$

The Feshbach resonance at 834 G of lithium-6 can be found in [18–20]. The background

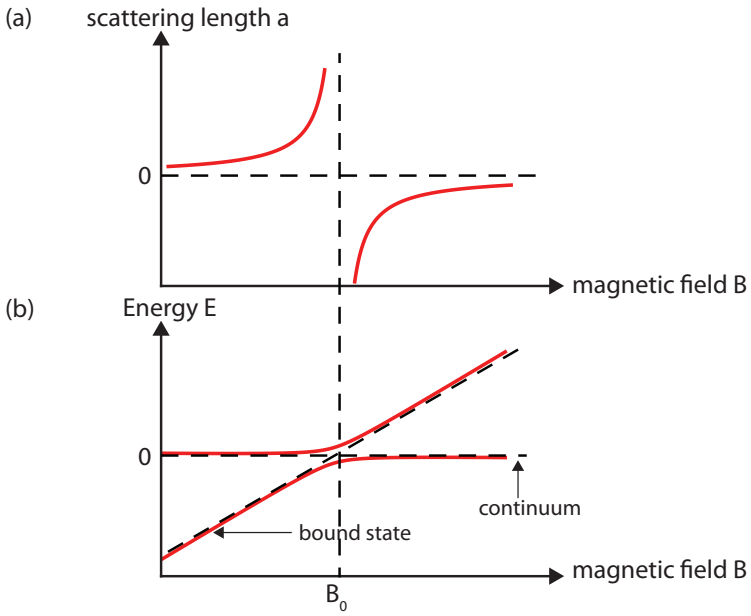

Figure 2.5: Feshbach resonance. *Figure courtesy of Kirsten Viering.*

scattering length, a_0, is the scattering length associated with $V_{bg}(r)$, and it represents the off-resonance value of the background scattering length. B_0 is the resonance position, and Δ is the resonance width. Feshbach resonances allow us to tune the s-wave scattering length, which is very useful when doing evaporation. Since lithium-6 is a fermion, only atoms in different atomic states can undergo s-wave collisions. Fortunately, lithium-6 has a broad Feshbach resonance between the states $|1\rangle$ and $|2\rangle$ (see figure 2.5) that occurs at 834 G with a width of about -300 G. Table 2.7 lists the widest Feshbach resonances between the three lowest hyperfine states of lithium-6.

Channel	Center	Width	Reference
$\|1\rangle$ $\|2\rangle$	834 G	-300 G	[17, 20]
$\|2\rangle$ $\|3\rangle$	691 G	-122.3 G	[20]
$\|1\rangle$ $\|3\rangle$	811 G	-222.3 G	[20]

Table 2.7: Feshbach resonances of the three lowest hyperfine states of lithium-6 as defined in figure 2.3.

2.4 Near Resonant Atom-Light Interactions

Solving Schrödinger's equation exactly for an atom interacting with a near-resonant field is hard, if not impossible. Fortunately, most of the time one can make some approximations that simplify the problem considerably while still giving a very good approximate solution. The equations that govern the interaction of near-resonant light with atoms are the optical Bloch equations, also known as the Maxwell-Bloch equations. The Maxwell-Bloch equations are derived in appendix B.

2.4.1 The Maxwell-Bloch Equations

These are obtained under the following approximations: 1) **Two-level atom approximation**, the atom is assumed to have only one ground and one excited state; 2) **Classical fields**, since we are dealing with large number of photons, we can use a classical description for the light fields; 3) **Electric dipole approximation**, since the wavelength of the light field is larger than the size of our atoms, we can consider it to be nearly constant across the atom; 4) **Rotating wave approximation**, since the light field is near resonant, we can assume that $|\omega_{\text{laser}} - \omega_{\text{transition}}| \ll |\omega_{\text{laser}} + \omega_{\text{transition}}|$. Under these assumptions, the Maxwell-Bloch equations are:

$$\dot{\widetilde{\rho}}_{ee} = -\frac{i}{2}(\Omega\widetilde{\rho}_{ge} - \Omega^*\widetilde{\rho}_{eg}) - \gamma\widetilde{\rho}_{ee} \tag{2.19}$$

$$\dot{\widetilde{\rho}}_{gg} = \frac{i}{2}(\Omega\widetilde{\rho}_{ge} - \Omega^*\widetilde{\rho}_{eg}) + \gamma\widetilde{\rho}_{ee} \tag{2.20}$$

$$\dot{\widetilde{\rho}}_{ge} = -\frac{i\Omega^*}{2}(\widetilde{\rho}_{ee} - \widetilde{\rho}_{gg}) - i\delta\widetilde{\rho}_{ge} - \frac{\gamma}{2}\widetilde{\rho}_{ge} \tag{2.21}$$

$$\dot{\widetilde{\rho}}_{eg} = \frac{i\Omega}{2}(\widetilde{\rho}_{ee} - \widetilde{\rho}_{gg}) + i\delta\widetilde{\rho}_{eg} - \frac{\gamma}{2}\widetilde{\rho}_{eg}. \tag{2.22}$$

Here

$$\Omega \equiv \frac{\widetilde{E}}{\hbar}\langle e| - e\vec{\mathbf{r}}\cdot\hat{\epsilon}\,|g\rangle \tag{2.23}$$

$$\hat{\mu}_{eg} \equiv \langle e| - e\vec{\mathbf{r}}\cdot\hat{\epsilon}\,|g\rangle \tag{2.24}$$

$$\gamma = \frac{\omega_0^3\mu^2}{3\pi\epsilon_0\hbar c^3} = 1/\tau \tag{2.25}$$

$$\delta = \omega - \omega_0, \tag{2.26}$$

where γ[1] is the natural decay rate and τ is the lifetime of the transition, $\hat{\mu}_{eg}$ is the electric dipole matrix coefficient, δ is the detuning from the atomic transition frequency $\omega_0 = 2\pi\nu_0$, and Ω is the "Rabi Frequency".

The steady state solutions are:

$$\widetilde{\rho}_{ee} = \frac{s}{2(1+s)} \tag{2.27}$$

$$\widetilde{\rho}_{eg} = \frac{-i\Omega}{2(\gamma/2 - i\delta)} \frac{1}{1+s}, \tag{2.28}$$

where

$$s \equiv \frac{|\Omega|^2/2}{\delta^2 + \gamma^2/4} = \frac{2|\Omega|^2/\gamma^2}{1 + (2\delta/\gamma)^2} = \frac{s_0}{1 + (2\delta/\gamma)^2} \tag{2.29}$$

with

$$s_0 \equiv 2|\Omega|^2/\gamma^2 = I/I_{sat} \tag{2.30}$$

$$I_{sat} \equiv \frac{2\pi^2\hbar\gamma c}{3\lambda_0^3}. \tag{2.31}$$

s is called the *saturation parameter*, and s_0 the *on-resonance saturation parameter*. I_{sat} is called the saturation intensity; it defines the on-resonance intensity level at which the transition starts to saturate. λ_0 is the on-resonance transition's wavelength.

2.4.2 Scattering Rate and Absorption Cross Section

Using equation (2.28) we can rewrite (2.19) as

$$\frac{d\widetilde{\rho}_{ee}}{dt} = \frac{|\Omega|^2}{2} \frac{\gamma/2}{(\gamma/2)^2 + \delta^2} (\widetilde{\rho}_{gg} - \widetilde{\rho}_{ee}) - \gamma\widetilde{\rho}_{ee} \tag{2.32}$$

The third term, $\gamma\widetilde{\rho}_{ee}$, is the photon spontaneous decay rate,

$$\gamma_p = \gamma\widetilde{\rho}_{ee} = \frac{\gamma}{2}\left(\frac{s_0}{1 + s_0 + (2\delta/\gamma)^2}\right) \tag{2.33}$$

the first and the second term differ only in a minus sign, and they are the absorption and stimulated emission terms respectively. The absorption coefficient per atom is then,

$$R_{abs} = \frac{|\Omega|^2}{2} \frac{\gamma/2}{(\gamma/2)^2 + \delta^2} \tag{2.34}$$

[1]Note that the units of γ are s^{-1}, while the units of Γ are Hz. γ, with units s^{-1}, should be used when dealing with scattering rates and lifetimes. While Γ, in units of Hz, should be used when dealing with detunings and line broadenings.

The absorption cross section is defined as

$$\sigma_{abs} \equiv \frac{\text{Photon energy absorption rate}}{\text{Incoming photon intensity}} \tag{2.35}$$

therefore,

$$\sigma_{abs} = \frac{\hbar\omega R_{abs}}{\frac{1}{2}\epsilon_0 c\left|\vec{\mathbf{E}}\right|^2} = \frac{k\mu^2}{\epsilon_0\hbar(\gamma/2)}\frac{1}{1+(2\delta/\gamma)^2} = \sigma_0\frac{1}{1+(2\delta/\gamma)^2} \tag{2.36}$$

$$\sigma_0 \equiv \frac{k\mu^2}{\epsilon_0\hbar(\gamma/2)} = \frac{3\lambda^2}{2\pi} \tag{2.37}$$

Where σ_0 is the on resonance absorption cross section. It is remarkable that the resonant absorption cross section depends solely on the wavelength of the transition!

2.4.3 Near-resonant Forces on Atoms

The force exerted by near-resonant light on an ensemble of atoms can be calculated using Eherenfest's theorem

$$F = \left\langle \hat{\mathbf{F}} \right\rangle = \left\langle \frac{d\hat{\mathbf{p}}}{dt} \right\rangle \tag{2.38}$$

and the steady state solutions of the Maxwell-Bloch equations. The total force is [2]

$$F = \frac{\hbar}{2}\frac{1}{(1+I/I_{sat}+(2\delta/\gamma)^2)}\left(k\gamma\frac{I}{I_{sat}} - \delta\frac{\partial}{\partial z}\left(\frac{I}{I_{sat}}\right)\right), \tag{2.39}$$

which can be split into $F = F_{scattering} + F_{dipole}$

$$F_{scatt} = \frac{\hbar k\gamma}{2}\frac{I/I_{sat}}{(1+I/I_{sat}+(2\delta/\gamma)^2} \tag{2.40}$$

$$F_{dipole} = -\frac{\hbar\delta}{2}\frac{1}{(1+I/I_{sat}+(2\delta/\gamma)^2)}\frac{1}{I_{sat}}\frac{\partial I}{\partial z} \tag{2.41}$$

The dipole force is proportional to the gradient of the intensity, thus it can be derived from a potential:

$$U_{dipole} = \frac{\hbar\delta}{2}\ln\left(1+I/I_{sat}+(2\delta/\gamma)^2\right) \tag{2.42}$$

The dipole force is conservative; it cannot be used to cool atoms, but it can be used to trap them. The scattering force is not conservative because the spontaneous emission of photons is an irreversible process, thus it can be used to cool but not to trap. Both forces can be used together to trap and cool atoms.

[2] See Appendix B for derivation

2.5 Far-Off-Resonance Atom Light Interactions

Far-off resonance optical dipole traps are used in the experiment to do optical evaporation and culling. Equation (2.42) for the optical dipole trap assumes the rotating wave approximation, that is

$$\left|\frac{\omega_{\text{laser}} + \omega_{\text{transition}}}{\omega_{\text{laser}} - \omega_{\text{transition}}}\right| \gg 1 \tag{2.43}$$

This is not valid for the CO_2 laser ($\lambda_{CO_2} = 10.6\mu m$) or the YAG laser ($\lambda_{\text{YAG}} = 1064nm$), for which

$$\left|\frac{\omega_{CO_2} + \omega_{D_2}}{\omega_{CO_2} - \omega_{D_2}}\right| = 1.13 \tag{2.44}$$

$$\left|\frac{\omega_{\text{YAG}} + \omega_{D_2}}{\omega_{\text{YAG}} - \omega_{D_2}}\right| = 4.41 \tag{2.45}$$

So expressions (2.40) and (2.41) cannot be used for the CO_2 laser or the YAG laser. Obtaining the Maxwell-Bloch equations without the rotating wave approximation is not easy. Fortunately, a classical approach can be used as long as the saturation parameter is small, which is the case for our two lasers:

$$s_{CO_2} \approx 10^{-8} \tag{2.46}$$

$$s_{\text{YAG}} \approx 10^{-11} \tag{2.47}$$

In the limit of low saturation we can use a classical model to obtain the dipole force and the scattering rate of a far-off resonant laser. The only non-classical consideration in our analysis will be the use of the quantum decay rate, γ, instead of the classical damping rate γ_0 obtained from Larmor's formula. When an atom is exposed to laser light, the electric field $\vec{\mathbf{E}}$ induces a dipole moment $\vec{\mathbf{p}}$ that oscillates at the driving frequency ω. We can express the electric field and the polarization in complex form as $\vec{\mathbf{E}}(\vec{\mathbf{r}}, t) = \hat{e}\widetilde{E}(\vec{\mathbf{r}})e^{-i\omega t} + c.c.$, and $\vec{\mathbf{p}}(\vec{\mathbf{r}}, t) = \hat{e}\widetilde{p}(\vec{\mathbf{r}})e^{-i\omega t} + c.c.$, where the complex amplitudes are related by,

$$\widetilde{p} = \alpha\widetilde{E} \tag{2.48}$$

Here α is the complex polarizability, which depends on the driving frequency ω. The interaction potential of the induced dipole moment is,

$$U_{dip} = \frac{1}{2}\langle \mathbf{p} \cdot \mathbf{E} \rangle = -\frac{1}{2\epsilon_0 c}\text{Re}(\alpha)I \tag{2.49}$$

The angular brackets denote time average over the rapid oscillatory terms, the 1/2 factor accounts for the fact that it is an induced polarizability, rather than a permanent one, and the field intensity in this notation is $I = 2\epsilon_0 c \left|\widetilde{E}\right|^2$. The dipole potential is therefore proportional to the intensity of the light field, and the dipole force is proportional to it's gradient:

$$\vec{\mathbf{F}}_{dip} = -\nabla U_{dipole}(\vec{\mathbf{r}}) = \frac{1}{2\epsilon_0 c}\mathrm{Re}(\alpha)\nabla I \tag{2.50}$$

The dipole force is a conservative potential. On the other hand, the force resulting from the absorbed power from the field gives rise to the scattering force, a non-conservative force. The power absorbed by the atom is:

$$P_{abs} = \langle \dot{\mathbf{p}}\mathbf{E} \rangle = \frac{\omega}{\epsilon_0 c}\mathrm{Im}(\alpha) I \tag{2.51}$$

which implies a scattering rate of

$$R_{scat} = \frac{P_{abs}}{\hbar\omega} = \frac{1}{\hbar\epsilon_0 c}\mathrm{Im}(\alpha) I \tag{2.52}$$

The complex polarizability can be calculated by integrating the equation of motion for the driven oscillation of the electron.

$$\ddot{x} + \gamma_\omega \dot{x} + \omega_0^2 x = -eE(t)/m_e \tag{2.53}$$

where

$$\gamma_\omega = \frac{e^2\omega^2}{6\pi\epsilon_0 m_e c^3} \tag{2.54}$$

is the classical damping rate due to radiative energy loss. In terms of the on-resonance damping rate $\gamma_{\omega_0} \equiv (\omega_0/\omega)^2\gamma_\omega$, the complex polarizability is [21],

$$\alpha = 6\pi\epsilon_0 c^3 \frac{\gamma_{\omega_0}/\omega_0^2}{\omega_0^2 - \omega^2 - i(\omega^3/\omega_0^2)\gamma_{\omega_0}} \tag{2.55}$$

In a semi-classical approach, the atomic polarizability can be calculated by treating the atom as a two-level system interacting with a classical radiation field. When saturation effects can be neglected, the classical approximation gives the same results as the semi-classical with only one modification: the classical damping rate γ_{ω_0} can no longer be

calculated from Larmor's formula, but must be calculated from the dipole matrix element between the ground and excited states, as in section 2.6:

$$\gamma_{\omega_0} \to \gamma = \frac{\omega_0^3}{3\pi\epsilon_0\hbar c^3} \left|\langle e| \mu |g\rangle\right|^2 . \tag{2.56}$$

In the limit of small saturations, the optical dipole potential and the scattering rate are given by [21],

$$U_{dip}(\vec{\mathbf{r}}) = -\frac{3\pi c^2}{2\omega_0^3}\left(\frac{\gamma}{\omega_0-\omega}+\frac{\gamma}{\omega_0+\omega}\right) I(\vec{\mathbf{r}}) \tag{2.57}$$

$$R_{scat}(\vec{\mathbf{r}}) = \frac{3\pi c^2}{2\hbar\omega_0^3}\left(\frac{\omega}{\omega_0}\right)^3\left(\frac{\gamma}{\omega_0-\omega}+\frac{\gamma}{\omega_0+\omega}\right)^2 I(\vec{\mathbf{r}}) \tag{2.58}$$

where *no rotating wave approximation has been made.* For an 86 Watts CO_2 laser beam focused down to a waist of 50 μm, we get a scattering rate of **2.5 photons per hour**, while for a 30 μW YAG beam focused down to a waist of 1.8 μm, merely **1.9 photons per hour**.

2.6 Electric Dipole Transition Coefficients

The electric dipole transition coefficient describes how one internal state of the atom couples to another via the electric dipole interaction with the near resonant field. Other kinds of transitions – such as magnetic and higher multipolar ones exist – but they are much weaker than the electric dipole and will not be considered here. The matrix element for a transition that drives an atom from the state $|(JI)Fm_F\rangle$ to the state $|(J'I')F'm_{F'}\rangle$ is given by,

$$\langle (J'I')F'm_{F'}|\, \vec{\mu}\, |(JI)Fm_F\rangle \tag{2.59}$$

Calculating the integral (2.59) is not a trivial task. Fortunately, we can use the Wigner-Eckart theorem to simplify the calculations considerably. Realizing that the electric dipole operator can be written in the irreducible spherical tensor basis as

$$\langle (J'I')F'm_{F'}|\, \mu_q^1\, |(JI)Fm_F\rangle\,, \tag{2.60}$$

we can use the Wigner-Eckart theorem to factor out the F' and F dependence,

$$\langle (J'I')F'm_{F'}|\, \mu_q^1\, |(JI)Fm_F\rangle = (-1)^{F'-mf'} \begin{pmatrix} F' & 1 & F \\ -m_{F'} & q & m_F \end{pmatrix} \left\langle (J'I')F'||\mu^1||(JI)F\right\rangle , \tag{2.61}$$

where the term in parenthesis is the Wigner 3-j symbol and the term with double bars is the reduced matrix element. Since the electric dipole operator changes only J and not I, we can use identity (A.8) to express $\langle (J'I')F'||\mu^1||(JI)F\rangle$ in terms of $\langle (L'S')J'||\mu^1||(LS)J\rangle$,

$$\begin{aligned}\left\langle (J'I')F'||\mu^1||(JI)F\right\rangle =&\delta_{II'}(-1)^{J'+I+F+1}\sqrt{(2F+1)(2F'+1)}\\ &\begin{Bmatrix} J' & F' & I \\ F & J & 1 \end{Bmatrix}\left\langle (L'S')J'||\mu^1||(LS)J\right\rangle\end{aligned} \tag{2.62}$$

where the term in curly brackets is a Wigner 9-j symbol. Again, since the electric dipole operator changes L and not S, we can use equation (A.8) to reduce the matrix element $\langle (L'S')J'||\mu^1||(LS)J\rangle$ and express it in terms of $\langle L'||\mu^1||L\rangle$

$$\begin{aligned}\left\langle (L'S')J'||\mu^1||(LS)J\right\rangle =&\delta_{SS'}(-1)^{L'+S+J+1}\sqrt{(2J+1)(2J'+1)}\\ &\begin{Bmatrix} L' & J' & S \\ J & L & 1 \end{Bmatrix}\left\langle L'||\mu^1||L\right\rangle\end{aligned} \tag{2.63}$$

The reduced matrix elements for the D, D_1, and D_2 line are given in table 2.8

Property	Symbol	Value	Reference
D-Line Reduced Matrix Element	$\langle L'=1\|\|\mu^1\|\|L=0\rangle$	1.148×10^{-29} C·m	[12]
		3.443×10^{-18}esu·cm	[12]
		3.443 Debye	[12]
		$\sqrt{3}\mu_0$	[12]
D_1-Line Reduced Matrix Element	$\langle J'=1/2\|\|\mu^1\|\|J=1/2\rangle$	-2.812×10^{-29} C·m	[12]
		-8.433×10^{-18} esu·cm	[12]
		-8.433 Debye	[12]
		$-\sqrt{2}\mu_0$	[12]
D_2-Line Reduced Matrix Element	$\langle J'=1/2\|\|\mu^1\|\|J=1/2\rangle$	3.977×10^{-29} C·m	[12]
		11.925×10^{-18}esu·cm	[12]
		11.925 Debye	[12]
		$2\mu_0$	[12]

Table 2.8: Reduced matrix elements for ^{6}Li

2.7 Fermi Gases

At high temperatures gases obey Maxwell-Boltzmann statistics, while at low temperatures they obey Fermi-Dirac or Bose-Einstein statistics depending whether they are made of fermions or bosons. Ultra-cold bosons will condense into a Bose-Einstein condensate with all the atoms occupying the same ground state, while fermions will occupy only one energy level per spin state up to the Fermi surface. This natural splitting that arises from the Pauli exclusion principles makes fermions more suitable to prepare Fock states using the culling process.

For a system of indistinguishable fermions, equation (2.64) gives the occupation number of a phase space cell at temperature T,

$$f(\vec{\mathbf{r}}, \vec{\mathbf{p}}) = \frac{1}{e^{\left(\frac{\vec{\mathbf{p}}^2}{2m} + V(\vec{\mathbf{r}}) - \mu\right)/k_B T} + 1} \tag{2.64}$$

where μ is the chemical potential [22] . Sometimes, however, it is simpler to work in terms of the total energy rather than with $\vec{\mathbf{p}}$ and $\vec{\mathbf{r}}$. In terms of the energy, the mean occupation number of each energy level with energy ϵ is given by

$$f(\epsilon) = \frac{1}{e^{(\epsilon-\mu)/kT} + 1}, \tag{2.65}$$

The chemical potential μ can be calculated by requiring that the total number of particles be N, that is

$$N = \int_0^\infty f(\epsilon) g(\epsilon) d\epsilon \tag{2.66}$$

where $g(\epsilon)$ is the density of states for the given potential. For a three dimensional harmonic potential,

$$V(\vec{\mathbf{r}}) = \frac{1}{2} m(\omega_x^2 x^2 + \omega_y^2 y^2 + \omega_z^2 z^2), \tag{2.67}$$

the density of states is given by [23]

$$g(\epsilon) = \frac{\epsilon^2}{2\hbar^3 \omega_x \omega_y \omega_z} = \frac{\epsilon^2}{2\hbar^3 \bar{\omega}^3}, \tag{2.68}$$

where $\bar{\omega} = (\omega_x \omega_y \omega_z)^{1/3}$ is the geometric mean of the trapping frequencies. At $T = 0$, it is easy to see that $f(\epsilon) = 1$ for $\epsilon < \mu(T = 0)$, and $f(\epsilon) = 0$ for $\epsilon > \mu(T = 0)$. The integral (2.66) then becomes

$$E_F = \hbar\bar{\omega}(6N)^{1/3} = k_B T_F, \tag{2.69}$$

where $E_F \equiv \mu(T=0)$ is called the Fermi energy, and T_F the Fermi temperature. E_F is the highest energy an atom can have when $T = 0$. When the confining potential is harmonic, the radius of the cloud is,

$$R_F = \sqrt{\frac{2E_F}{m\bar{\omega}^2}} \tag{2.70}$$

At $T = 0$, equation (2.64) can also be easily integrated in momentum space to obtain the density distribution,

$$n(\vec{\mathbf{r}}) = \int_{|\vec{\mathbf{p}}| \leq \sqrt{2m(E_F - V(\vec{\mathbf{r}}))}} \frac{d^3\vec{\mathbf{p}}}{(2\pi\hbar)^3} = \frac{1}{6\pi^2}\left(\frac{2m}{\hbar^2}\right)^{3/2}(E_F - V(\vec{\mathbf{r}}))^{3/2} \tag{2.71}$$

where $f(\vec{\mathbf{r}}, \vec{\mathbf{p}}) = 1$ for $|\vec{\mathbf{p}}| \leq \sqrt{2m(E_F - V(\vec{\mathbf{r}}))}$ and $f(\vec{\mathbf{r}}, \vec{\mathbf{p}}) = 0$ otherwise.

For non-zero temperatures, $T \leq T_F$, the chemical potential can be approximated by a Sommerfeld expansion,

$$\mu(T) = E_F\left(1 - \frac{\pi^2}{3}\left(\frac{T}{T_F}\right)^2\right) \tag{2.72}$$

The number density integral is not as easy as before, and it evaluates to a poly-logarithmic function,

$$n(\vec{\mathbf{r}}) = -\left(\frac{mk_BT}{2\pi\hbar^2}\right)^{3/2} Li_{3/2}\left(-e^{\left(\frac{\mu - V(\vec{\mathbf{r}})}{k_BT}\right)}\right) \tag{2.73}$$

From equation (2.65) it can be seen that the occupation probability of the lowest state increases when we increase the chemical potential and when we decrease the temperature. However, from equation (2.69) it can be seen that E_F depends on $N^{1/3}$, which makes E_F not very sensitive to variations in atom number. Even so, we strive to increase the atom number as much as possible, since the efficiency of evaporative cooling increases as the atom number increases. Figure 2.6 shows the mean occupation number for four different temperatures and energies both in units of the chemical potential.

How much should we cool a sample of atoms to reach the quantum regime? The temperature of the sample is not the only parameter that determines if the sample is

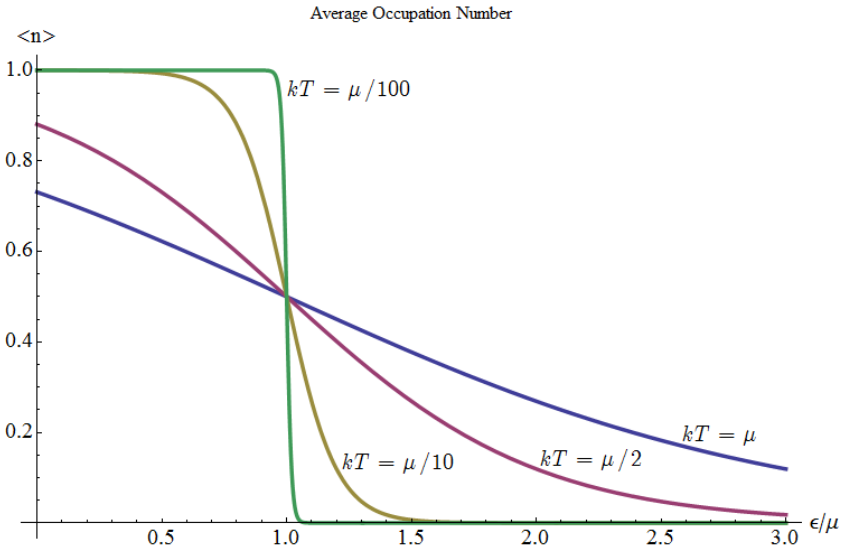

Figure 2.6: Fermi-Dirac Distribution. The Fermi-Dirac distribution (equation (2.65)) is shown for four different values of kT: $kT = \mu$, $kT = \mu/2$, $kT = \mu/10$, $kT = \mu/100$. For $T/T_F = 0.1$, $kT \approx \mu/10$ and the occupation probability of the ground state exceeds 0.9999.

or not in the quantum regime. The density of the sample is important as well, since a very cold but dilute system will not exhibit macroscopic quantum behavior. Degeneracy occurs when the mean separation between particles, $n^{-1/3}$, is close to the thermal de Broglie wavelength,

$$\lambda_{dB} = \sqrt{\frac{2\pi\hbar^2}{mk_BT}}$$

In other words, a cold gas is said to be in the quantum regime when the phase-space density $\rho = n\lambda_{dB}^3$ approaches unity, $\rho \approx 1$. For a gas of bosons, degeneracy is reached when $\rho \geq 2.6$. At this point, the system undergoes a phase transition and the ground states become macroscopically occupied. For a gas of fermions there is not such phase transition; the gas undergoes a smooth transition from the classical to the quantum regime. However, by analogy to the Bose-Einstein case, it is widely accepted by the cooling community that the Fermi gas has reached the quantum regime when the phase space density exceeds $\rho = 1$. The expression for the phase-space density of a classical gas in a three dimensional harmonic potential is:

$$\rho = N\left(\frac{\hbar\bar{\omega}}{k_BT}\right)^3. \tag{2.74}$$

This equation breaks down close to $T = 0$, but can be used as a simple approximation to estimate the degeneracy factor of the gas. As it is, equation (2.74) is not very useful since it involves parameters that are not of physical relevance for us. Instead, by substituting equation (2.69) into (2.74) and setting $\rho \geq 1$, we find that a gas of fermions becomes quantum degenerate when $T/T_F < 0.55$, where T/T_F is called the *degeneracy factor*. To achieve ultra-high fidelity, we must have $kT \leq \mu/10$, for then the occupation probability of the ground state will exceed $P_{gnd} \geq 0.9999$, and will not affect the single atom preparation scheme.

Part II

Atomic Physics Techniques

Chapter 3

Laser Locking

Lithium 6's D_2 line natural linewidth is 5.87 MHz, this means that if we want to control the light-atom interactions of near resonant light, we need to have a stability in the laser frequency of a few hundreds or even tens of kilohertz. Different detunings are used at different stages of the experimental sequence. One of the Toptica lasers is used as the master frequency reference and it is locked to the D_2 line of lithium 6 using frequency modulation (FM) spectroscopy [24]. The other two lasers, are locked to the spectroscopy laser using a beat-lock technique [25].

3.1 FM Spectroscopy

For small modulation index $M \ll 1$, the electric field $E_2(t)$ exiting the electro optic modulator shown in figure 3.1 is described by $E_2(t) = 1/2\widetilde{E}_2(t) + c.c.$, where

$$\widetilde{E}_2(t) = E_0 \left(-\frac{M}{2} e^{i(\omega_c - \omega_m)t} + e^{i\omega_c t} + \frac{M}{2} e^{i(\omega_c + \omega_m)t} \right) \tag{3.1}$$

and E_0 is the unmodulated electric field amplitude. The beam exiting the electro optic modulator consists of a central carrier frequency at ω_c, and two sidebands at $\omega_c \pm \omega_m$. The beam exiting the modulator then passes through our lithium 6 vapor cell. If the lenght of the sample is L and has an intensity absorption coefficient α and index of refraction n, we can calculate the total attenuation and phase shift that each frequency component experiences. The amplitude transmission coefficient for each spectral component is $T_j = \exp(-\kappa_j - i\phi_j)$, $\kappa_j = \alpha_j L/2$, $\phi_j = n_j L(\omega_c + j\omega_m)/c$, where $j = 0, \pm 1$ denotes the components at ω_c and $\omega_c \pm \omega_m$.

The transmitted field is then,

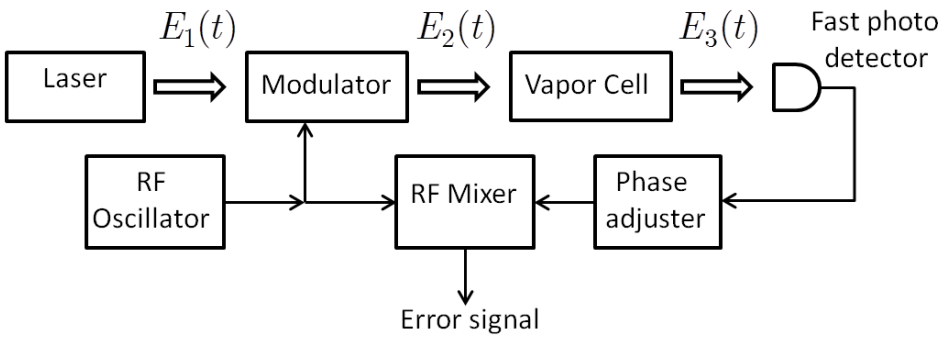

Figure 3.1: Frequency Modulation Spectroscopy

$$\widetilde{E}_3(t) = E_0 \left(-T_{-1}\frac{M}{2}e^{i(\omega_c-\omega_m)t} + T_0 e^{i\omega_c t} + T_1\frac{M}{2}e^{i(\omega_c+\omega_m)t} \right) \tag{3.2}$$

The intensity of the beam impinging on the photodetector is then $I_3(t) = 1/2\epsilon_0 c \left|\widetilde{E}_3(t)\right|^2$. Keeping only first order terms in M, and assuming that $|\kappa_0 - \kappa_1|$, $|\kappa_0 - \kappa_{-1}|$, $|\phi_0 - \phi_1|$, and $|\phi_0 - \phi_{-1}|$ are all $\ll 1$, the intensity can be written as

$$I_3(t) = \frac{1}{2}\epsilon_0 c \mathrm{e}^{-2\kappa_0} \left\{ (1 + (\kappa_{-1} - \kappa_1)M\cos(\omega_m t) + (\phi_1 + \phi_{-1} - 2\phi_0)M\sin(\omega_m t) \right\} \tag{3.3}$$

The photocurrent, being proportional to $I_3(t)$, will have a beat signal at ω_m as long as $\kappa_{-1} - \kappa_1 \neq 0$ or $\phi_1 + \phi_{-1} - 2\phi_0 \neq 0$. If ω_m is small compared to the transition's linewidth, then the $\cos(\omega_m t)$ component is proportional to the derivative of the absorption, and the $\sin(\omega_m)t$ is proportional to the second derivative of the dispersion. Equations (C.11) and (C.12) give the frequency dependence of the absorption and dispersion profiles of typical Lorentzian spectral feature. For low saturation intensities,

$$\kappa(\delta) = n\sigma_0 \frac{1}{(2\delta/\gamma')^2 + 1} \tag{3.4}$$

$$\phi(\delta) = n\sigma_0 \frac{(2\delta/\gamma')}{(2\delta/\gamma')^2 + 1} \tag{3.5}$$

δ is the detuning from the atomic transition, and γ' is the transition linewidth, which might be collision or Doppler broadened. For locking purposes, we use the $\sin(\omega_m t)$ term, which depends on the dispersion and does not depend on the intensity of the

beam. Care should be taken to adjust the phase correctly to pick only the dispersive term, so that any laser intensity noise does not couple with the frequency stabilization.

The error signal we get in our system is not as simple as the one in equation (3.3), since we have not one but two hyperfine transitions: the MOT transition, from the $^2S_{1/2}$ $|F = 3/2\rangle$ to the $^2P_{3/2}$ manifold; and the repump transition, from the $^2S_{1/2}$ $|F = 1/2\rangle$ to the $^2P_{3/2}$ state manifold. Furthermore, since the transitions are Doppler broadened, the beam is retroreflected to reduce the Doppler broadening as much as possible. This introduces an extra "cross over" transition that shows up in the error signal. This cross over transition [26] occurs right at the middle between the two real transitions, when the Doppler shift of the atoms is enough for the MOT transition to excite the repump transition or vice versa. The total error signal can be seen in figure 3.2; it contains contributions from the two hyperfine transitions and the cross over transition, each weighted by their transition strength.

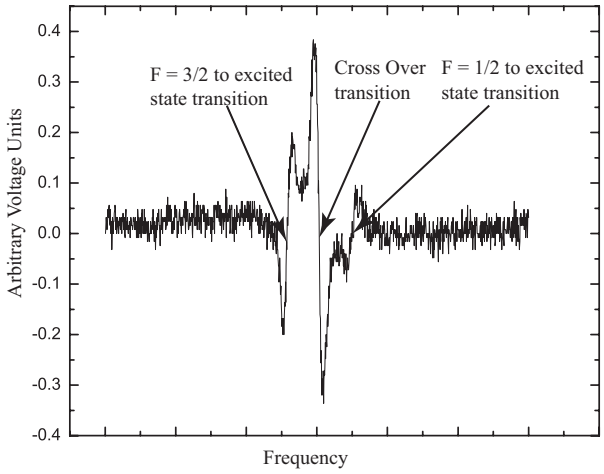

Figure 3.2: Error Signal from the Spectroscopy Cell. The figure shows the error signal derived from the spectroscopy signal. The distance between the $F = 3/2$ and $F = 1/2$ transitions is the hyperfine splitting, 228 MHz. The cross over is located exactly half way in between the transitions. The height of each peak depends on the relative strengths of each transition. Data courtesy of Kirsten Viering.

We lock the spectroscopy laser to the $^2S_{1/2}$ $|F = 3/2\rangle \rightarrow {}^2P_{3/2}$ transition. The Tapered Amplifier and the Imaging laser are then locked to the spectroscopy laser using a beat-lock technique.

3.2 Beat-Locking Technique

The beat-locking technique [25] allows one to lock one laser to another with a tunable frequency offset. This is very useful to us because we need to change the detuning of the laser beams at different stages of the experiment. The scheme works as follows: the reference laser beam and the slave laser beam are both focused on a fast photodiode that records their beat signal. The beat signal contains two frequencies, one at $\nu_{master} + \nu_{slave}$ and another one at $|\nu_{master} - \nu_{slave}|$. The high frequency component is eliminated by using a low pass filter. The resulting component with frequency $\Delta\nu = |\nu_{master} - \nu_{slave}|$, is mixed with another signal with frequency ν_{VCO} coming from a voltage controlled oscillator. This produces two new frequencies, and the higher one is eliminated again with a low pass filter.

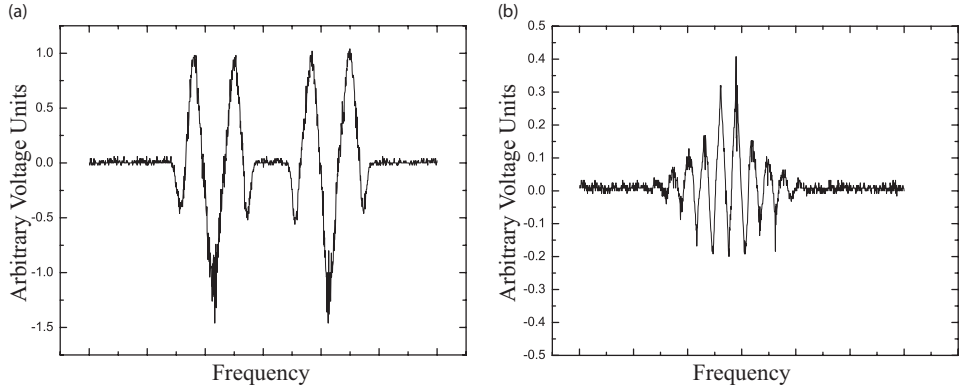

Figure 3.3: Error Signals from the beat-lock setup. (a) error signal from the Tapered Amplifier, (b) error signal from the imaging laser. The lasers are locked to the points were the signals are zero. The difference between the two signals reflect the different bandwidths of the RF components used on each locking setup. *Data courtesy of Kirsten Viering.*

The resulting signal has a frequency of $|\Delta\nu - \nu_{VCO}|$. This signal is split into two equal parts by a signal splitter, and one of them is delayed by a cable of length L. The non-delayed signal is proportional to $\cos(2\pi\,|\Delta\nu - \nu_{VCO}|\,t)$, while the delayed signal is proportional to $\cos(2\pi\,|\Delta\nu - \nu_{VCO}|\,t + \Phi)$, where $\Phi = 2\pi\,|\Delta\nu - \nu_{VCO}|\,\tau$. The delayed and non-delayed signals are then recombined in a mixer and the component with the sum of the frequencies is again eliminated with a low pass filter. The component with the difference of the frequencies is then proportional to $\cos(2\pi\,|\Delta\nu - \nu_{VCO}|\,\tau)$. This error

signal can be then used to lock the difference in the frequencies between the spectroscopy laser and the slave laser. The error signal from the tapered amplifier and the imaging laser can be seen in figure 3.3. The envelope of the error signal reflects the bandwidth of the photodetector and all the electronic components used in the scheme. The zero crossings of the signal provide locking points and their separation in frequency depends on the delay introduced by the cable, $\delta\nu = \frac{1}{2\tau}$. Once the lasers are locked, the frequency offset can be verified by using a digital counter.

Chapter 4

Atomic Cooling and Trapping

The forces that light exerts on atoms can be used to cool and trap them. The Zeeman Slower and the Magneto Optical Trap (MOT) make use of non-conservative near resonant light-induced forces to slow, cool, and compress the atoms. In contrast, the CO_2 dipole trap and the YAG dipole trap use far off resonance, conservative, light-induced forces to trap the atoms. I will now describe the theory of how each of these work. The technical details on their construction and calibration will be described in chapter 6. Finally, their performance will be described in chapter 7.

4.1 Zeeman Slower

The starting point of our experiment is a solid piece of lithium 6 inside the oven. At room temperature, the vapor pressure does not produce high enough flux to run the experiment. Therefore, to increase the vapor pressure, the oven is heated to 350 °C. At this temperature, lithium melts and its vapor escapes through a small hole and forms an effusive beam. Although the flux is now high enough to run the experiment, the atoms are moving too fast for the MOT to capture them. Therefore, we must first slow them from an initial speed of 1000 m/s to around 50 m/s – the MOT's trapping velocity. To accomplish this, we use the scattering force of a near-resonant beam of light to slow down the atoms.

An atom moving at a speed of 1050 m/s has momentum of around $p_{\mathrm{Li}} = 10^{-23}$ kg·m/s, while a photon of near 671 nm light has a momentum of, $p_{670\ \mathrm{nm}} = 10^{-27}$ kg·m/s. Therefore, we need around 10,000 scattering events to slow down the atom from 1050 m/s to 50 m/s. This means we need to be able to use the same transition over and over; we need to use a cycling transition. The transition that we chose is the ${}^2S_{1/2}\,|m_J = 1/2\rangle \rightarrow$

$^2P_{3/2}\,|m_J = 3/2\rangle$, for which we need circularly polarized light, σ^+. At high fields this is a closed transition. At low fields, however, it is not completely a closed transition and a repump beam $^2S_{1/2}\,|F = 1/2\rangle \rightarrow {}^2P_{3/2}\,|F = 3/2\rangle$ must be added, thus we derive the power of the Zeeman slower from the same beam that powers the MOT. Typical powers in the Zeeman slower are 30 mW for the MOT component, and 10 mW for the repump component.

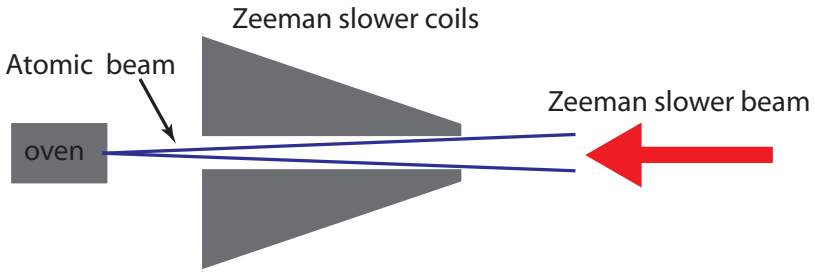

Figure 4.1: Zeeman Slower. An effusive beam coming from the oven propagates through the Zeeman slower coils (shown propagating to the right). A red-detuned near-resonant beam propagates in the opposite direction to the effusive beam (here shown propagating to the left). *Figure courtesy of Kirsten Viering.*

The Zeeman slower consists of a near resonant red detuned laser beam propagating in opposite direction relative to the atoms, and a set of coils that generate either an increasing, decreasing, or inverting magnetic field. Each way of building a Zeeman slower has its own advantages and disadvantages. We chose the decreasing field Zeeman slower (high field near the oven, low field close to the MOT) to perturb the magnetic fields of the MOT as little as possible.

A red-detuned near-resonant beam of light ($\delta_0 = \omega_{laser} - \omega_{transition} < 0$) is placed counter propagating along the effusive beam, as seen in figure 4.1. The Doppler shift that the atom experiences is,

$$\Delta\omega = -\vec{\mathbf{k}}_{670} \cdot \vec{\mathbf{v}}_{\mathrm{Li}} > 0$$

so the total detuning is

$$\delta_{\text{total}} = \delta_0 - \vec{\mathbf{k}}_{670} \cdot \vec{\mathbf{v}}_{\text{Li}} > \delta_0. \tag{4.1}$$

Fast moving atoms see the Zeeman beam closer to resonance than slow moving atoms. As a result, they scatter photons and slow down. At this point, the Doppler shift decreases and the Zeeman beam appears to be farther from resonance. A magnetic field is introduced to compensate for the decrease in Doppler shift due to the decrease in velocity. We use the $\hat{\mathbf{J}}$ basis since the fields involved are in the range of hundreds of Gauss for the most part of the slower. The Zeeman splitting for the excited state $^2\mathrm{P}_{3/2}$ is

$$\Delta E_{^2\mathrm{P}_{3/2}} = \mu_B g'_{3/2} m'_{3/2} B_z \tag{4.2}$$

while the Zeeman splitting for the ground state $^2\mathrm{S}_{1/2}$, is

$$\Delta E_{^2\mathrm{S}_{1/2}} = \mu_B g_{1/2} m_{1/2} B_z \tag{4.3}$$

which gives a total Zeeman splitting of

$$\Delta E_Z = \mu_B (g'_{3/2} m'_{3/2} - g_{1/2} m_{1/2}) B_z \tag{4.4}$$

using equation (2.15), and using the quantum numbers for the cycling transition, $g'_{3/2} = 4/3$, $g_{1/2} = 2$, $m'_{3/2} = 3/2$ and $m_{1/2} = 1/2$, we get,

$$\Delta E_Z = \mu_B B_z \tag{4.5}$$

or in frequency,

$$\Delta\omega_Z = \frac{\mu_B}{\hbar} B_z \tag{4.6}$$

$$\delta_{\text{total}} = \delta_0 - \vec{\mathbf{k}}_{670} \cdot \vec{\mathbf{v}}_{\text{Li}} + \frac{\mu_B}{\hbar} B_z \tag{4.7}$$

setting the total detuning equal to zero, we can solve for B(z) and get,

$$B(z) = -\frac{h}{\mu_B} \left(\Delta_0 + \frac{1}{\lambda} v(z) \right) \tag{4.8}$$

where $\Delta_0 = \nu_{laser} - \nu_{transition}$. Assuming that the atom experiences a uniform deceleration, we can write the speed as $v(z) = \sqrt{v_0^2 - 2az}$, so equation (4.8) becomes,

$$B(z) = -\frac{h}{\mu_B} \left(\Delta_0 + \frac{1}{\lambda} \sqrt{v_0^2 - 2az} \right) \tag{4.9}$$

For our system, $\Delta_0 = 120$ MHz, $\lambda = 671$ nm, v_0= 700 m/s, and a is taken to be half the maximum acceleration $a = a_{max}/2 = \hbar k\gamma/4m_{\mathrm{Li}} = 9.146 \times 10^5$ m/s^2. The predicted field and the measured field can be seen in section 6.2.1.

While the absorption of photons always gives a momentum kick in the direction opposing propagation, the spontaneous emission of the photon occurs in a random direction and will lead to heating and beam dispersion in the transverse direction. Thus, the Zeeman slower cannot be made arbitrarily long because the beam would spread too much, reducing the loading rate of the MOT.

4.2 Magneto Optical Trap

Following the Zeeman slower, the atoms are now moving slow enough to be trapped by the magneto optical trap (MOT). Just like the Zeeman slower, the MOT uses red-detuned, near resonant beams to slow down atoms. Unlike the Zeeman slower, it uses the magnetic field to introduce a position dependent light-force. It does not confine the atoms magnetically; rather, it uses the magnetic field to induce a position-dependent scattering force that the atoms feel. Since each atom has to scatter many photons to be cooled and trapped, a cycling transition must be used as well. However, unlike the Zeeman slower, the magnetic fields in the MOT are sufficiently small that the splitting of the two ground states due to the hyperfine interaction becomes important. Figure 4.2 shows the relevant transitions for our MOT. Exciting the transition $^2\mathrm{S}_{1/2}\ |F = 3/2\rangle \rightarrow {}^2\mathrm{P}_{3/2}\ |F = 5/2\rangle$ inevitably sends some atoms into the $^2\mathrm{S}_{1/2}\ |F = 1/2\rangle$ ground state. Once in the $^2\mathrm{S}_{1/2}\ |F = 1/2\rangle$ state, the original light field can no longer excite them to the $^2\mathrm{P}_{3/2}\ |F = 5/2\rangle$ excited state. Therefore, a second laser beam, a repump, has to be added to pump the atoms back into the cycle. In ^{6}Li , the amount of light required for the repumper is comparable to the one needed for the main cooling beam. The ratio is approximately MOT:RP = 3:1. Since the power of the repumper is on the same order as that of the cooling beam, they both are considered cooling beams and the total cooling power is the sum of the MOT and the repump. Table 4.1 shows the typical powers for the MOT and the Zeeman slower.

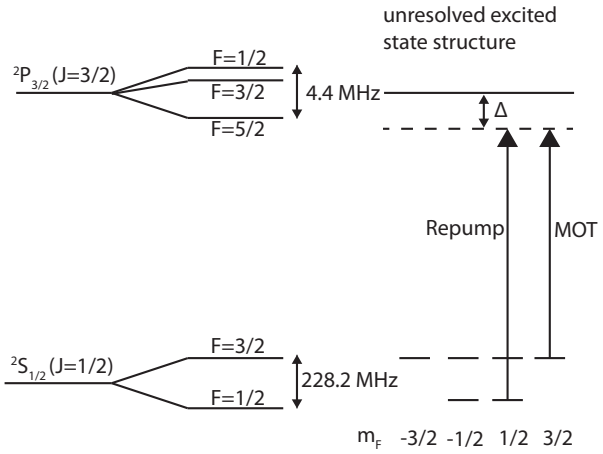

Figure 4.2: MOT transitions. The main cooling beam excites the $^2S_{1/2}$ $|F = 3/2\rangle \rightarrow$ $^2P_{3/2}$ transition. Some of the atoms fall into the lower ground state $^2S_{1/2}$ $|F = 1/2\rangle$, and thus a rempumper that excites the $^2S_{1/2}$ $|F = 1/2\rangle \rightarrow$ $^2P_{3/2}$ transition is needed. The ratio of the MOT to repump power is nearly 3:1. *Figure courtesy of Kirsten Viering*

Fiber	MOT	Repump
Fiber No. 1	11.6 mW	5.4 mW
Fiber No. 2	6.8 mW	5.5 mW
Fiber No. 3	10.3 mW	6.3 mW
Zeeman Slower	33 mW	11 mW

Table 4.1: Typical powers of the MOT and the Zeeman slower.

Figure 4.3 shows the configuration of the near-resonant beams and the magnetic fields of the MOT. A pair of coils is set up in anti-Helmholtz configuration; the distance between the center of the coils equals the radius of the coils. When current is sent in opposite directions through each coil, the resulting field is a quadrupole field that is quasi-linear near the zero of the field, located on the axis of the coils at the midpoint between the coils. The optical component of the MOT consists of three pairs of near-resonant counter-propagating beams, propagating along the x, y, and z directions. The beams are circularly polarized to drive the cycling transition.

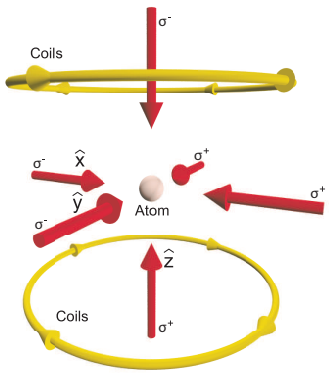

Figure 4.3: MOT Diagram. The Magneto Optical Trap consists of two coils carrying current on anti-helmholtz configuration that give rise to a quadrupole magnetic field, and three paris of right-handed near-resonant red-detuned counter-propagating beams that intersect orthogonally at the zero of the magnetic quadrupole field. *Figure courtesy of Gabriel Price.*

The slowing force that the magneto optical trap exerts over the atoms is known as optical molasses. The scattering force that an atom with velocity $\vec{\mathbf{v}}$ will feel in a red detuned laser beam propagating allong the direction $\vec{\mathbf{k}}$ will be $\vec{\mathbf{F}} = \hat{\mathbf{k}} F_{scat}(\delta_0 - \vec{\mathbf{k}} \cdot \vec{\mathbf{v}})$. For any pair of conterpropagating beams (see figure 4.4), $\vec{\mathbf{k_1}} = -\vec{\mathbf{k_2}}$, the total force is

$$\begin{aligned} \vec{\mathbf{F}}_{total} &= \hat{\mathbf{k_1}} F_{scat}(\delta_0 - \vec{\mathbf{k_1}} \cdot \vec{\mathbf{v}}) + \hat{\mathbf{k_2}} F_{scat}(\delta_0 - \vec{\mathbf{k_2}}) && (4.10) \\ &= \hat{\mathbf{k_1}} \left(F_{scat}(\delta_0 - \vec{\mathbf{k_1}} \cdot \vec{\mathbf{v}}) - F_{scat}(\delta_0 + \vec{\mathbf{k_1}} \cdot \vec{\mathbf{v}}) \right) && (4.11) \end{aligned}$$

Figure 4.4: Molasses. Two red-detuned near-resonant beams are propagating in the directions $\vec{\mathbf{k}}_1$ and $\vec{\mathbf{k}}_2$. When the atom moves to the right, it scatters more photons from beam 1, when it moves to the left, it scatters more photons from beam 2. The faster the atom moves, the more it scatters.

Figure 4.5 shows the damping force for typical parameters of our MOT (P = 12 mW per beam, waist = 10 mm, detuning = $-2\pi \times 38$ MHz). Since we have a pair of beams for each direcion in space, the MOT can cool in three dimensions. However, although these beams can cool down a sample of atoms due to their dissipative force,

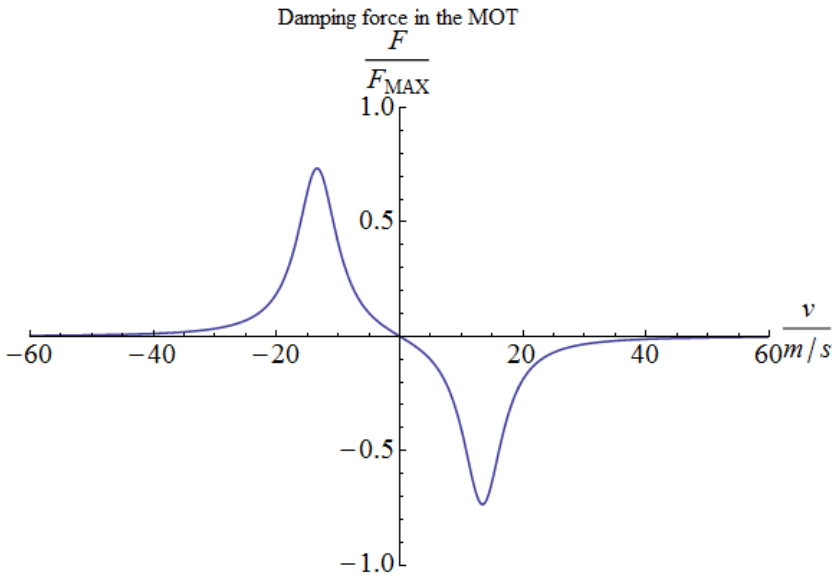

Figure 4.5: 1D MOT damping force plot. The velocity-dependent damping force is shown for typical parameters of the MOT. P = 12 mW per beam, waist = 10 mm, and $\Delta = -2\pi\times 38$ MHz. The velocity is shown in units of m/s and the force in units of $F_{MAX} = \hbar k\gamma/2$.

they cannot compress them. Any two points inside the volume where the six beams intersect are equivalent. Furthermore, the atoms cannot be cooled down to absolute zero because spontaneous emission inevitably heats the atoms. To see this, imagine we start with one atom completely at rest inside the volume of the six beams. The atom will have equal probability of absorbing photons from any of the six beams, and as soon as it absorbs a photon, it will scatter it in a random direction. Thus, the atom has been heated spontaneously, and it will perform a random walk in velocity-space and three-dimensional-space (random walk in phase-space). The speed, however, cannot grow indefinitely because the cooling mechanism eventually kicks in, balancing the cooling and the heating rates at a finite temperature. This is not the case for the displacement; without a confining potential, the displacement will grow without bound until the atom eventually exits the cooling region and escapes the MOT.

To overcome this problem, a position-dependent force has to be imposed on the atom. By using a quadrupole magnetic field, we can induce a position-dependent Zeeman shift. For illustration purposes, consider a MOT with a cycling transition between a

$J = 0$ state and a $J = 1$ state. The initial state is $J = 0$, $m = 0$, and the final state is $J = 1$, $m_J = -1, 0, 1$. Consider the 1-Dimensional MOT shown in figure 4.6 in which a constant magnetic field gradient B' causes a Zeeman shift $\Delta E_Z = m_J \mu_B B' z$ ($g_J = 1$ for illustration purposes). A σ^+ polarized beam can drive transitions in which $\Delta m = 1$, while a σ^- polarized beam can drive transitions with $\Delta m = -1$. Due to the Zeeman splitting, an atom at the right of the origin ($z = z'$) will be closer to resonance with the σ^- beam propagating to the left, while an atom at the left side of the origin will be closer to resonance with the σ^+ beam propagating to the right. Thus, the quadrupole field effectively induces a position dependent force which is linear with distance. With the addition of the quadrupole field, the MOT can cool and compress the atoms.

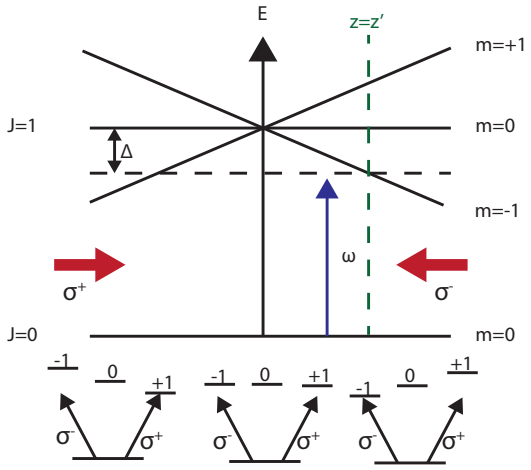

Figure 4.6: Position dependent force of a MOT. A one dimensional MOT with a cycling transition between a $J = 0$ state and a $J = 1$ state is shown in the figure. Two red-detuned circulary polarized counter propgating beams are shown in red. The beam propagating to the left has a σ^- polarization and can drive $\Delta m = -1$ transitions, while the beam propagating to the right has a σ^+ polarization and can drive $\Delta m = 1$ transitions. A constant magnetic field gradient B' induces a linear Zeeman shift $\Delta E_Z = m_J \mu_B B' z$ (let $g_J = 1$ for now). To the right of the origin, ($z = z'$), the Zeeman shift moves the $m_J = -1$ state closer to resonance, and thus the atom will absorb the σ^- beam more strongly than the σ^+. At the other side of the origin, the Zeeman shift will move the $m_J = 1$ state closer to resonance and the atom will then absorb the σ^+ beam more strongly than the σ^-. The Zeeman shift then induces a position dependent force that can be used to trap atoms. *Figure courtesy of Kirsten Viering*

The minium temperature that can be achieved in theory with optical molasses is

the Doppler temperature [27],

$$T_D = \frac{\hbar\gamma}{2k_B} \tag{4.12}$$

which for our cooling transition is 140 μK. In practice, however, it is difficult to perfectly align the beams and the minimum temperature we can achieve is around 250 μK when the MOT is compressed. This is cold enough to load atoms into the CO_2 optical dipole trap.

4.3 Optical Evaporation

The minimum temperatures obtainable in a lithium 6 MOT are around 250 μK with around 2×10^7 atoms. With typical number densities of n $\approx 10^{11}$ cm^{-3}, this corresponds to a phase space density of $\rho \approx 10^{-6}$. In order to further increase phase space density, we use optical evaporation. The goal of evaporation is to induce runaway evaporation, in which the temperature drops much faster than the atom loss, thus increasing the phase space density as a result. Runaway evaporation allows us to achieve low enough temperatures and high enough numbers to achieve Fermi degeneracy, which by convention occurs when $T/T_F \leq 0.55$. Since the lowest hyperfine states of lithium are high-field seekers, they cannot be trapped magnetically. Therefore, magnetic traps cannot be used to confine lithium 6; optical dipole traps have to be used instead [28].

During evaporation, the most energetic atoms escape from the trapping potential. Then, the remaining atoms in the sample rethermalize to a lower temperature. In practice, these two processes occur at the same time until the process stagnates, at which point the evaporation can be further forced by changing the depth of the confining potential. Figure 4.7 illustrates the process. At the beginning of evaporation, the high velocity tail of the distribution is ejected from the sample. The sample rethermalizes to a lower temperature, and the process is repeated again. This is done continously during the experiment.

The final temperature is not the only important parameter at the end of evaporation. Recall from section 2.7 that in order to reach quantum degeneracy, the phase-space density has to exceed 1. This means that both the number density and the temperature

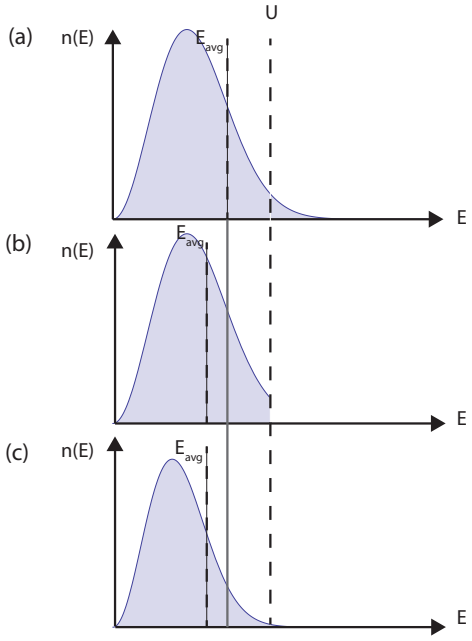

Figure 4.7: Evaporative Cooling. a) The initial sample has a mean energy E^1_{avg}. b) The high-energy tail of the sample is ejected from the trap. c) The sample rethermalizes at a lower average energy $E^2_{avg} < E^1_{avg}$. *Figure courtesy of Kirsten Viering.*

have to be considered. During evaporation, one would like to lower the temperature "faster" than the rate at which the atoms are lost. In other words, phase-space density must increase at all times during evaporation. The ideal curve must take into the account the collisional properties of our sample but, in general, the larger the cross section between the atoms the faster the sample will rethermalize, making evaporation more efficient. Since ^{6}Li is a fermion, two atoms will undergo s-wave scattering only if they are in different hyper-fine states. We use the two lowest hyper-fine states $|1\rangle$ and $|2\rangle$ (see figure 2.3) to achieve degeneracy. When the cross section is independent of energy, the lowering curve is [29]

$$\frac{U(t)}{U_0} = \left(1 + \frac{t}{\tau}\right)^{-2(\eta-3)/\eta} \tag{4.13}$$

where $\eta \equiv U/k_B T$ is kept constant. Near the Feshbach resonance, when the gas is in the unitary regime and the cross section is energy-dependent, the ideal lowering curve is [30]

$$\frac{U(t)}{U_0} = \left(1 - \frac{t}{\tau}\right)^{2(\eta-3)/(\eta-6)} \tag{4.14}$$

4.4 Culling in the Microtrap

While optical evaporation can produce a cold Fermi gas with $T/T_F \leq 0.55$, we can get an even higher Fermi temperature, and therefore a lower degeneracy factor, if we superimpose a small-volume but tightly focused optical dipole trap on top of the CO_2 optical dipole trap. Our microtrap consists of a Nd:YAG laser with a wavelength of 1064 nm focused to a spot of 1.46 μm. If we perform the optical evaporation with our microtrap ON, we can assume that the atoms are going to be thermalized inside the microtrap. Typical final atom number and temperatures for our degenerate Fermi gas are $T \approx 0.53$ μK, and $N \approx 1.3 \times 10^5$ with a power of $P \approx 0.8$ W. We know we can load at most $N \approx 10^3$ atoms into a microtrap and therefore we can assume the trap is completely full, and the Fermi temperature of our system increases by the trap depth of our microtrap. For an initial power of 500 μW, the trap depth of our mictrop is around 6 μK. This gives an effective Fermi temperature of

$$T_F^{\text{Total}} = T_F^{CO_2} + T_F^{\text{Micotrap}} = 1.2\mu\text{K} + 6\mu\text{K} = 7.2\mu\text{K} \tag{4.15}$$

and since we assume thermalization, the Fermi gas in the microtrap should have an efective degeneracy factor of

$$T/T_F^{\text{Total}} = \frac{0.530\ \mu\text{K}}{1.2\ \mu\text{K} + 6\ \mu\text{K}} \approx 0.07 \tag{4.16}$$

which gives a ground state occupation probability exceeding 99.9999%. I will now explain how the spilling scheme works.

As the name suggests, atomic *culling* involves the selection of atoms that meet certain criteria, while the rest are thrown away. Atomic culling can be done in several ways, all of which involve loading atoms into an optical dipole trap: reducing the trap depth [31]; reducing the trap depth and squeezing the trap [32]; and reducing the trap depth and adding a linear potential that "tilts" the trap [33]. The last method, reducing

the trap depth and "tilting" the potential, has already been utilized to create two-atom fermionic Fock states with a fidelity of 96% [34]. I will now describe this last method with more detail.

Consider the potential formed by an optical dipole trap and a magnetic field gradient,

$$V_{\text{optical}} = 1 - \frac{1}{1+(z/z_R)^2} \exp\left(-2\frac{((x-x_0)^2+(y-y_0)^2)}{w^2(1+(z/z_R)^2)}\right) + \mu_{\text{Li}}\frac{dB}{dz}z \tag{4.17}$$

The ratio of the radial trapping frequencies to the axial trapping frequencies is,

$$\eta = \frac{\omega_r}{\omega_a} = \pi\sqrt{2}\frac{w}{\lambda} \tag{4.18}$$

so for a $w = 1.46$ μm focused laser with $\lambda = 1.064$ μm, we have a ratio,

$$\eta = \frac{\omega_r}{\omega_a} = 6.05 \tag{4.19}$$

so as long as our system has less than 12 atoms, we can treat it as one dimensional. Furthermore, we will assume the atoms are in the ground state in the radial direction so we can ignore any offset and set $x = x_0 = y = y_0 = 0$. For now we ignore the graviational force since it only introduces an extra linear term that can be absorbed into the magnetic field term. If initially, only the ground and excited state are populated, and τ_{gnd} and τ_{exc} denote their lifetimes respectively, then the probability that after a time τ_{hold} there is one atom in the ground state is

$$P_{gnd} = e^{-t_{hold}/t_{gnd}} \tag{4.20}$$

for the first excited state

$$P_{exc} = e^{-t_{hold}/t_{exc}} \tag{4.21}$$

So the probability of having one atom in the ground state and no atom in the excited state is

$$P_{single} = (1 - P_{exc}) \cdot P_{gnd} = (1 - e^{-t_{hold}/t_{exc}}) \cdot e^{-t_{hold}/t_{gnd}} \tag{4.22}$$

If the lifetimes of the ground and excited state differ by several orders of magnitude, then the probability of obtaining a single atom in the ground state of the trap can be as high as 99.9%.

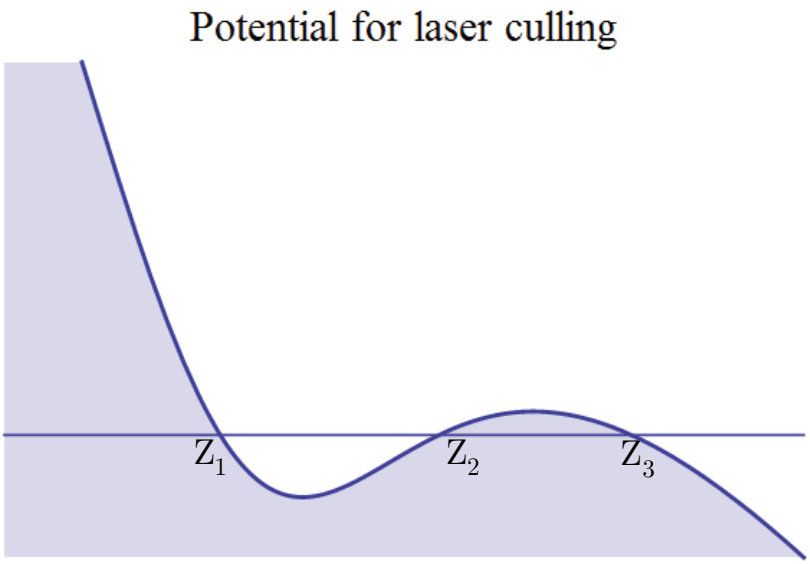

Figure 4.8: WKB method. Z_1, Z_2, and Z_3 represent the classical turning points of a particle in the potential.

The question is now how to calculate the lifetimes of the quasi-bound states. We employ the WKB approximation [35] to obtain approximate solutions to Schrödinger's equation and calculate the lifetimes of the quasi-bound states. Let Z_1, Z_2, and Z_3 in figure 4.8 represent the classical turning points of a particle with energy E. A quasi-bound state with energy E_n satisfies

$$\int_{Z_1}^{Z_2} \sqrt{2m(E_n - V(z))}dz = \left(n + \frac{1}{2}\right)\pi\hbar \tag{4.23}$$

Having found the energy using the previous equation, the transmission probability for the energy level E_n is

$$T(E_n) = e^{-\frac{2}{\hbar}\int_{Z_2}^{Z_3}\sqrt{2m(V(z)-E_n)}dz} \tag{4.24}$$

this is roughly the probability that the particle will tunnel everytime it "bounces" off Z_2. If T_0^n is the trapping frequency of energy level E_n, then a particle will bounce an average of $1/T(E_n)$ times and have a lifetime of

$$\tau \approx T_0^n e^{\frac{2}{\hbar}\int_{Z_2}^{Z_3}\sqrt{2m(V(z)-E_n)}dz} \tag{4.25}$$

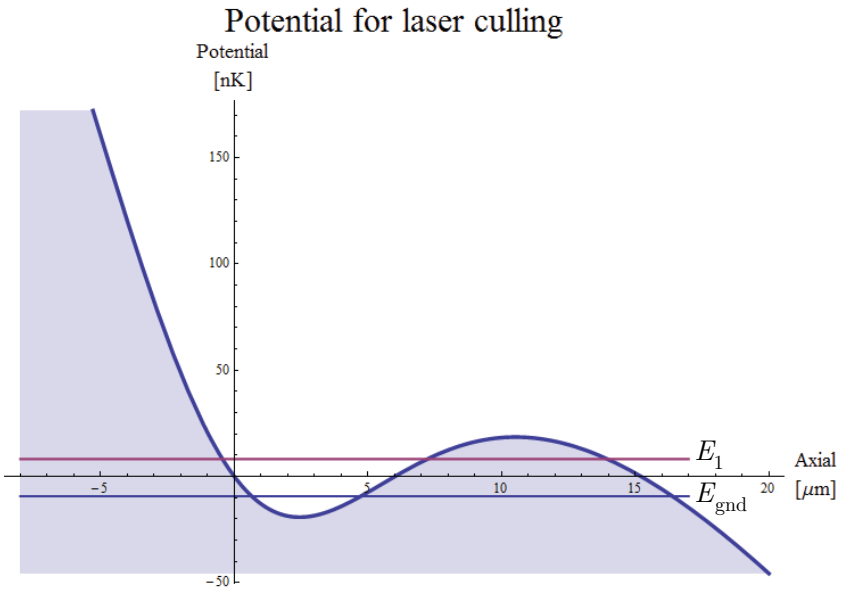

Figure 4.9: Culling potential. Culling potential (eq (4.17)) along the z axis for a 30 μW beam with a waist of 1.8 μm and a magnetic gradient of -2.5 G/cm. E_{gnd} and E_1 denote the ground state and first excited state energy levels. For this parameters, $E_{gnd} = -9.3203$ nK, $E_1 = 8.1317$ nK, $\tau_{gnd} = 3572$ s, and $\tau_1 = 0.3216$ s.

where the period of the energy level E_n can be calculated as,

$$T_0^n \approx \frac{\partial}{\partial E} \int_{Z_2}^{Z_3} \sqrt{2m(V(z) - E_n)} dz|_{E=E_{bound}} \tag{4.26}$$

As an example, figure 4.9 shows the potential for a 30 μ W beam of $\lambda = 1064$ nm light focused to a spot of 1.8 μm and a gradient of -2.5 G/cm. For these set of parameters, the lifetime of the ground state is $\tau_{gnd} = 3572$ s, while the lifetime of the first excited state is $\tau_1 = 0.3216$ s. The large difference in the lifetimes can be exploited to obtain a single pair of atoms in the ground state of the optical potential.

Chapter 5

Imaging Techniques

Producing a sample of cold atoms is not the end of the story; we might want to extract some information such as the atom number, the temperature, or its spatial profile. In order to disturb the sample as little as possible, most cold atom experiments use some kind of optical imaging method. There are three processes by which atoms can interact with light, each of which is used for a particular kind of imaging method [36] : spontaneous absorption of photons is used for absorption imaging, re-emission of photons is used for fluorescence imaging, and phase-shifting of the transmitted light is used for dispersive imaging methods. Dispersive imaging methods include phase-contrast imaging and dark-spot imaging. In this experiment we used fluorescence and absorption imaging.

Fluorescence imaging yields a higher signal to noise ratio when it comes to atom number, while on the downside it typically destroys all the spatial information of the sample. Absorption imaging, on the other hand, preserves the spatial information of the cloud but is not very sensitive to atom number. Therefore, we use fluorescence imaging for atom counting when we measure lifetimes and loading rates, while absorption imaging is the preferred method for cloud size and density profile measurements when we measure temperatures and density distributions.

5.1 Fluorescence Imaging

5.1.1 Atom Number and fluorescence

Fluorescence imaging is simple and very straightforward: we shine near resonant light on the sample and form an image from the scattered light. Figure 5.1 shows a typical fluorescence picture. The total number of counts a CCD camera measures from

light scattered by a sample of atoms is given by,

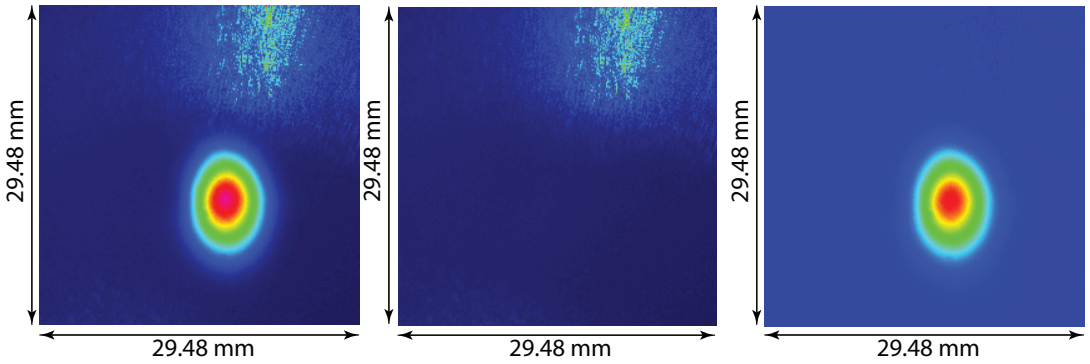

(a) Raw fluorescence picture (b) Probe picture. (c) Fluorescence picture

Figure 5.1: False color fluorescence pictures taken by our AltaU47 camera and processed by our image acquisition software *Vision*. a) Raw fluorescence picture: the picture is taken with the atoms and MOT beams ON. b) Probe picture: a second picture is taken only with the MOT beams ON. c) Fluorescence picture: The probe picture is subtracted from the raw fluorescence picture to eliminate background light as much as possible. In this particular picture, the atom number is $N = 1.07 \times 10^8$, and $\sigma_x = 1.98$ mm, $\sigma_y = 2.81$ mm.

$$N_{counts} = N_{atoms} \cdot R_{scattering} \cdot \Delta t \cdot \frac{\Delta\Omega}{4\pi} \cdot \frac{q}{g} \cdot T \tag{5.1}$$

Where Δt is the exposure time, $\frac{\Delta\Omega}{4\pi}$ is the fraction of solid angle that is collected, q is the quantum efficiency in units of [electrons/photons], g is the gain in units of [electrons/counts], T is the overall transmission coefficient of any filters that might be inserted, and $R_{scattering}$ is the scattering rate of an atom in a near resonant field in units of [photons/s]. Assuming that the Rotating Wave Approximation holds, the scattering rate is given by

$$R_{scattering} = \frac{\gamma}{2} \frac{s_0}{1 + s_0 + (2\delta/\gamma)^2} \tag{5.2}$$

where both δ and γ are in units of s^{-1}, and s_0 is the saturation parameter. The atom number is then,

$$N_{atoms} = N_{counts} \frac{8\pi}{\gamma} \frac{(1 + s_0 + (2\delta/\gamma)^2)}{s_0 \Delta t \Delta\Omega (q/g) T} \tag{5.3}$$

5.1.2 Atom Number Calibration for Fluorescence

To calibrate the atom counting we must measure the fractional solid angle and the ratio q/g. The fractional solid angle must be obtained from geometrical considerations of the imaging system, but typically it is in the order of 1% to 10%. The ratio q/g can be obtained by measuring the total counts on the CCD for a set of exposures at different optical powers. Then by making a fit to the equation

$$N_{counts} = \left(\frac{q}{g}\right) \frac{P\Delta t}{\hbar\omega} \cdot T \tag{5.4}$$

we get the following results,

Camera	q/g
Alta U47	0.348(4)
Stingray F033BC	0.467(1)

Table 5.1: Camera Calibrations

The error in the calibrations is less than 1%. The largest source of error comes from the fractional solid angle, but this can be measured with enough precision that its error amounts to at most 2%. The total error in atom number for not very optically thick clouds is therefore at most 3%. This precision is more than enough when the atom number is larger than 10^4.

5.1.3 Finding the Image Plane

In any imaging system, one must always place the detector at the image plane. In common optical systems, the objects being imaged have definite and sharp boundaries, which makes it very easy to tell if the object is in focus or not. This is not the case for fuzzy objects. *One does not simply* move the CCD chip back and forth and find where the sharpest image of the atomic cloud is. In order to find the image plane, one can use a simple trick known as the *split image method*. See figure 5.2.

To implement the split image method, all that is needed is to place a card with two holes separated as far as possible right after the focusing lens. This will create two

images of the atomic cloud that will intersect at the image plane. Once the image plane is found, we can proceed to find the magnification of the system.

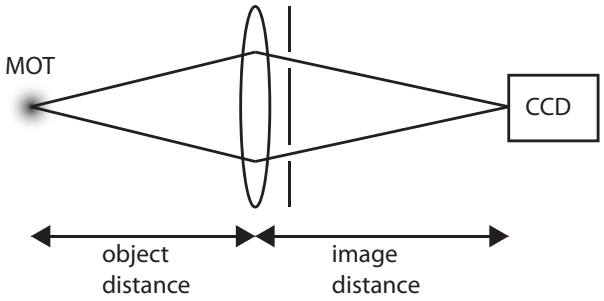

Figure 5.2: Split Image Method. A card with two holes is placed behind the imaging lens. Two images will be formed, and they will intersect at the image plane of the lens. *Figure courtesy of Kirsten Viering*

5.1.4 Magnification Calibration for Fluorescence

Knowing the magnification is not necessary to calculate the atom number in fluorescence imaging, it is necessary in absorption imaging to calculate the size and spatial profile of the cloud. Measuring the magnification of the imaging system is most easily done with fluorescence imaging. In our case, because we mounted the CO_2 focusing lens on a 3D translation stage, we can move our CO_2 dipole trap to different vertical positions, load atoms, and do short-exposure fluorescence images. If the exposures are short enough ($\Delta t < 0.1$ ms), the position and shape of the CO_2 dipole trap can be seen and its center can still be located. The magnification can be found from the displacements of the CO_2 dipole trap in the image *vs* the real displacement. Figure 5.3 shows the magnification calibration for the Stingray camera.

5.1.5 Limitations of Fluorescence Imaging

As simple as fluorescence imaging is, it has some limitations and one would be advised to keep them in mind. There are several mechanisms that can lead to an erroneous atom number when using fluorescence. These are,

- **Photon re-absorption within the cloud**. Reabsorption of photons within the cloud can happen if the cloud is optically thick, the power is high enough to

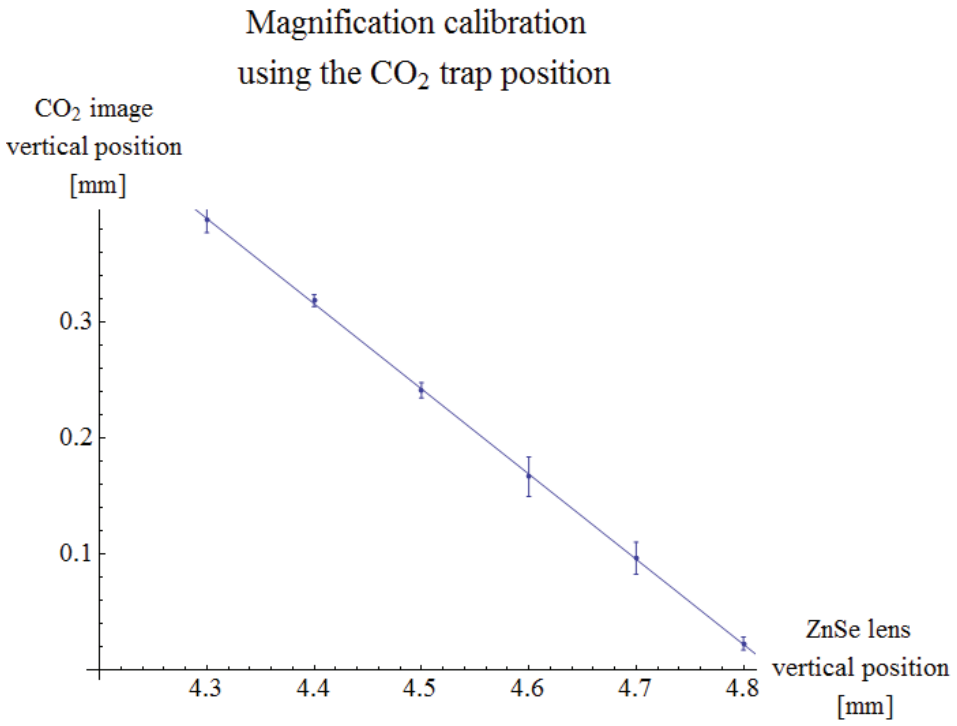

Figure 5.3: Stingray camera imaging system calibration. The vertical position of the center of the CO_2 optical dipole trap mas measured *vs* the vertical displacement of the ZnSe lens. For small displacements, the positions of the lens and the CO_2 trap inside the chamber are 1:1. By looking at the apparent displacement on the CCD chip, the magnification can be calculated. The error bars indicate statistical uncertainties in the CO_2 trap position. A linear fit gives the magnification, in this case, $M = (734 \pm 4) \times 10^{-3}$.

cause power broadening, or the photons are too close to resonance. To avoid this problem, we image at 15 MHz from resonance.

- **Atom loss**. If the exposure time is too long or the detuning is very small, atoms will be lost and the atom number will be an average over time. This leads to an underestimate of the initial atom number. To avoid this problem, we image at 15 MHz from resonance and for 30 ms maximum.

- **Saturating the CCD**. If the sample fluoresces very strongly, the CCD could saturate if no filters are used. This would lead to an underestimated atom number. If the fluorescence signal is too strong, we insert an 8% transmission neutral density filter.

- **Blooming of the CCD**. Blooming (see figure 5.4) occurs when the CCD is pre-exposed to strong light and the CCD chip doesn't have enough time to clear. A phantom pattern of this strong light can then be seen in the picture taken by the camera. Although blooming is hard to eliminate from a single picture, it is quite reproducible so one can easily just recreate the same conditions before the probe or noise pictures are taken and then subtract them from the sample picture. The blooming effect can be cancelled almost entirely.

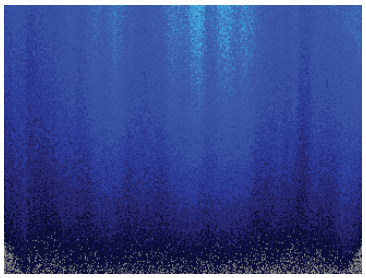

Figure 5.4: CCD camera blooming.

5.2 Absorption Imaging

Fluorescence imaging enables us to measure atom number with a high signal to noise ratio. It does so, however, at the expense of the spatial density profile of the sample. If one wants to learn about the spatial profile of the sample or disturb it as little as possible, then one would have to resort to absorptive or dispersive methods.

Setting up the imaging system for absorption imaging is relatively simple: one uses fluorescence imaging to find the image plane and then measures the magnification; however, using absorption imaging correctly is not as simple nor as straightforward as fluorescence. A more careful analysis is needed to correctly interpret the measurements.

To calculate the correct density profile, one has to take into account the power, detuning, polarization, and orientation (relative to any present magnetic field) of the absorption beam; the strength of any magnetic fields present, and the population of the atomic state being imaged. Essentially, however, one needs three pictures to calculate the number density from absorption imaging: 1) *Raw absorption picture*: this picture is

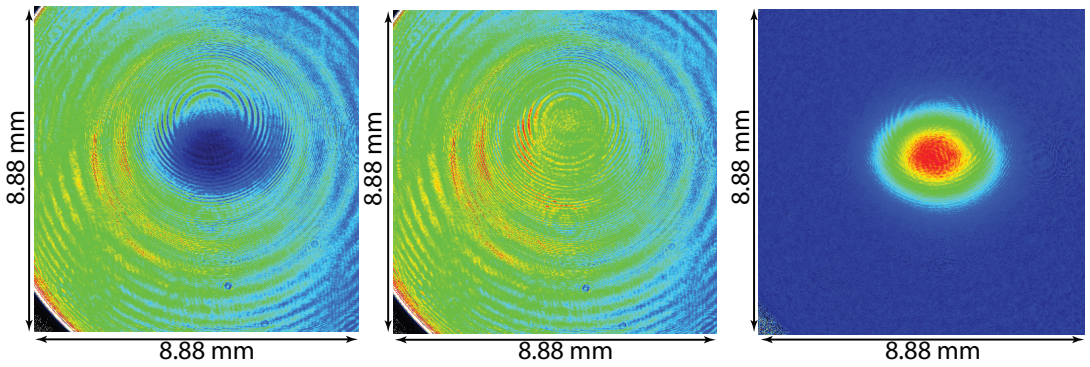

(a) Raw absorption picture (b) Probe picture. (c) Number density

Figure 5.5: False color absorption pictures of a compressed MOT. a) Raw absorption picture of a compressed MOT. The atomic cloud has absorbed part of the probe beam and can be seen as a shadow. b) Probe picture without the atoms. The net absorption is calculated subtracting the probe image from the raw absorption image, from which the number density can be calculated using either equation (5.8) or (5.22). c) Number density. This picture corresponds to a cloud of $N = 6.6 \times 10^7$ atoms with a size of $\sigma_x = 1.082$ mm and $\sigma_y = 0.781$ mm.

taken with the atoms present and shows a bright background with a shadow produced by the atoms. Typical exposure times are between 5 and a few tens of μs with a few μW of power; 2) *Probe picture*, this picture is taken with exactly the same conditions as the raw absorption picture, but without the atoms; 3) *Noise picture*, this picture is taken with the camera shutter closed and is used to reduce the noise caused by dark counts. Figure 5.5 shows a typical absorption image of the compressed MOT.

The effect that a cloud of atoms has on the electric field of a beam of near-resonant light is discussed in appendix C.

5.2.1 Absorption Imaging at Low Fields

At zero magnetic field, the orientation of the absorption beam is irrelevant since the interaction is isotropic. For a one to one imaging system, the intensity at the CCD is obtained by simply integrating Beer's law (equation (C.16)),

$$I(x, y) = I_0(-x, -y)e^{-\beta} \tag{5.5}$$

where

$$\beta \equiv \frac{\tilde{n}(-x,-y)\sigma_0}{1+(2\delta/\gamma)^2} \tag{5.6}$$

and $I_0(x,y)$ is the initial intensity distribution at the atomic cloud location (i.e. with no atoms present), and

$$\tilde{n}(-x,-y) = \int_{allz} n(x,y,z)dz \tag{5.7}$$

is the 3D density distribution integrated along the axis of propagation, called the column density, and σ_0 is the on-resonance optical cross section for the particular transition. Solving for the number density we get,

$$\tilde{n}(-x,-y) = \frac{1+(2\delta/\gamma)^2}{\sigma_0} \ln\left(\frac{I(x,y)}{I_0(-x,-y)}\right) \tag{5.8}$$

In practice, the image is discretized by the finite size of the pixels, and $I(x,y)$ and $I_0(x,y)$ are obtained by subtracting the noise picture to the raw absorption and probe picture respectively. In terms of pixels, equation (5.8) becmoes

$$\tilde{n}_{ij} = \frac{1+(2\delta/\gamma)^2}{\sigma_0} \ln\left(\frac{(\text{Raw Abs Picture})_{ij} - (\text{Noise Picture})_{ij}}{(\text{Probe Picture})_{ij} - (\text{Noise Picture})_{ij}}\right) \tag{5.9}$$

The only remaining quantity to calculate is σ_0, the on-resonance optical absorption cross section. We calculate σ_0 for the MOT and repump transitions in the next section.

5.2.2 Optical Absorption Cross Section for the MOT and Repump

To calculate the absorption optical cross section we need to know the electric dipole transition matrix coefficient. At zero magnetic fields, all the magnetic sublevels (m_F) are degenerate, so all possible values of m_F have to be taken into account. Moreover, since the excited state hyper-fine splitting is unresolved, all possible values of F_2 must be taken into account as well.

We assume that the resonant light is a mixture of all possible polarization, and we express this by writing the electric dipole transition operator as:

$$\vec{\mu} = \sum_q \mu_q^1 a(q)\hat{e}_q \tag{5.10}$$

where μ_q^1 is the q-th spherical tensor component of the electric dipole operator, and $a(q)$ is the q-th polarization amplitude.

$$\sum_q |a(q)|^2 = 1 \tag{5.11}$$

We calculate the average of the square of the optical transition matrix, and since the excited states are unresolved since they are separated by less than 5 MHz, we sum over all F_2's and all m_{F_2}'s

$$\mu^2 = \frac{1}{2F_1+1} \sum_q |a(q)|^2 \sum_{F_2, m_{F_2}, m_{F_1}} \left| \langle (J_2 I) F_2 m_{F_2} | \, \mu_q^1 \, | (J_1 I) F_1 m_{F_1} \rangle \right|^2 \tag{5.12}$$

but,

$$\langle (J_2 I) F_2 m_{F_2} | \, \mu_q^1 \, | (J_1 I) F_1 m_{F_1} \rangle = (-1)^{F_2 - m_{F_2}} \begin{pmatrix} F_2 & 1 & F_1 \\ -m_{F_2} & q & m_{F_1} \end{pmatrix} \langle (J_2 I) F_2 || \mu^1 || (J_1 I) F_1 \rangle \tag{5.13}$$

so

$$\mu^2 = \frac{1}{2F_1+1} \sum_q |a(q)|^2 \sum_{F_2, m_{F_2}, m_{F_1}} \begin{pmatrix} F_2 & 1 & F_1 \\ -m_{F_2} & q & m_{F_1} \end{pmatrix}^2 \left| \langle (J_2 I) F_2 || \mu^1 || (J_1 I) F_1 \rangle \right|^2 \tag{5.14}$$

using (A.6), we can evaluate the sum over m_{F_1} and m_{F_2},

$$\mu^2 = \frac{1}{2F_1+1} \sum_q |a(q)|^2 \sum_{F_2} \frac{1}{3} \left| \langle (J_2 I) F_2 || \mu^1 || (J_1 I) F_1 \rangle \right|^2 \tag{5.15}$$

which reduces to

$$\mu^2 = \frac{1}{3(2F_1+1)} \sum_{F_2} \left| \langle (J_2 I) F_2 || \mu^1 || (J_1 I) F_1 \rangle \right|^2 \tag{5.16}$$

which means that the total transition strength is independent of the initial polarization of light. Using equation (A.8) to decouple F into J, we get,

$$\mu^2 = \frac{1}{3(2F_1+1)} \sum_{F_2} (2F_1+1)(2F_2+1) \left| \begin{Bmatrix} J_2 & F_2 & I \\ F_1 & J_1 & 1 \end{Bmatrix} \right|^2 \left| \langle (L_2 S) J_2 || \mu^1 || (L_1 S) J_1 \rangle \right|^2 \tag{5.17}$$

$$\mu^2 = \frac{1}{3(2J_1+1)} \left| \langle (L_2 S) J_2 || \mu^1 || (L_1 S) J_1 \rangle \right|^2 \tag{5.18}$$

So for the D_2 line, independent of whether it is the MOT ($F_1 = 3/2$) or the repump ($F_1 = 1/2$)

$$\mu^2 = \frac{2}{3}\mu_0^2 \tag{5.19}$$

which means that,

$$\sigma_0^{MOT} = \sigma_0^{RP} = \frac{2}{3}\sigma_0 = \frac{\lambda^2}{\pi} \tag{5.20}$$

5.2.3 Absorption Imaging at High Fields

The two lowest hyper-fine states of ^{6}Li have a broad Feshbach resonance at about 834 G. When performing evaporation at high fields, we might want to image the atoms at high fields rather than ramping the homogeneous magnetic field down to zero and risk heating the sample. The absorption of light by atoms at high fields is not as straightforward and simple as the zero field case. A strong magnetic field will break the symmetry of the system, and a preferred direction, which we will call z, will now exist. It can be shown [37] that for a circularly polarized beam at 90 degrees from the z direction, the intensity at the CCD is now given by,

$$I(x,y) = \frac{1}{2} I_0(-x,-y)\left(e^{-\beta/2} + 1\right) \tag{5.21}$$

where again,

$$\beta = \frac{\tilde{n}(-x,-y)\sigma_0}{1 + (2\delta/\gamma)^2}$$

Solving for the number density now get,

$$\tilde{n}(-x,-y) = -\frac{2(1 + (2\delta/\gamma)^2)}{\sigma_0} \ln\left(2\frac{I(x,y)}{I_0(-x,-y)} - 1\right) \tag{5.22}$$

or in terms of pixels,

$$\tilde{n}_{ij} = \frac{1 + (2\delta/\gamma)^2}{\sigma_0} \ln\left(2\left(\frac{(\text{Raw Abs Picture})_{ij} - (\text{Noise Picture})_{ij}}{(\text{Probe Picture})_{ij} - (\text{Noise Picture})_{ij}}\right) - 1\right) \tag{5.23}$$

5.3 Calculating the Atom Number

Given a number density $n(x, y, z)$, the total atom number is simply

$$N = \int_{space} n(x, y, z) dx dy dz$$

or in terms of the column density,

$$N = \int_{XY-plane} \tilde{n}(x, y) dx dy$$

since the integration is done in all the plane, we can exchange x and y for $-x$, and $-y$

$$N = \int_{XY-plane} \tilde{n}(-x, -y) dx dy \tag{5.24}$$

where $\tilde{n}(-x, -y)$ is the column density found in sections 5.2.1 and 5.2.3. Now, one must be careful about how to interpret dx and dy. We carry out our integration at the CCD plane because we have detected our intensity distribution there, but the coordinates in formula (5.24) refer to the location of the atomic cloud.

$$N = \int_{XY-plane} \tilde{n}(-x_{cloud}, -y_{cloud}) dx_{cloud} dy_{cloud} \tag{5.25}$$

A simple transformation will allow us to integrate at the CCD plane,

$$dx_{CCD} = M dx_{cloud}$$

$$dy_{CCD} = M dy_{cloud}$$

where M is the magnification of the optical system. In reality, dx and dy are the width and height of each pixel at the CCD, so the integral (5.25) is really a sum over pixels:

$$N = \frac{\Delta x_{CCD}}{M} \frac{\Delta y_{CCD}}{M} \left(\sum_{ij} \tilde{n}_{ij} \right) \tag{5.26}$$

5.4 Measuring the Temperature

The temperature of an atomic cloud is found by measuring how fast it expands during free expansion. Suppose we have a trapped gas with Gaussian velocity and

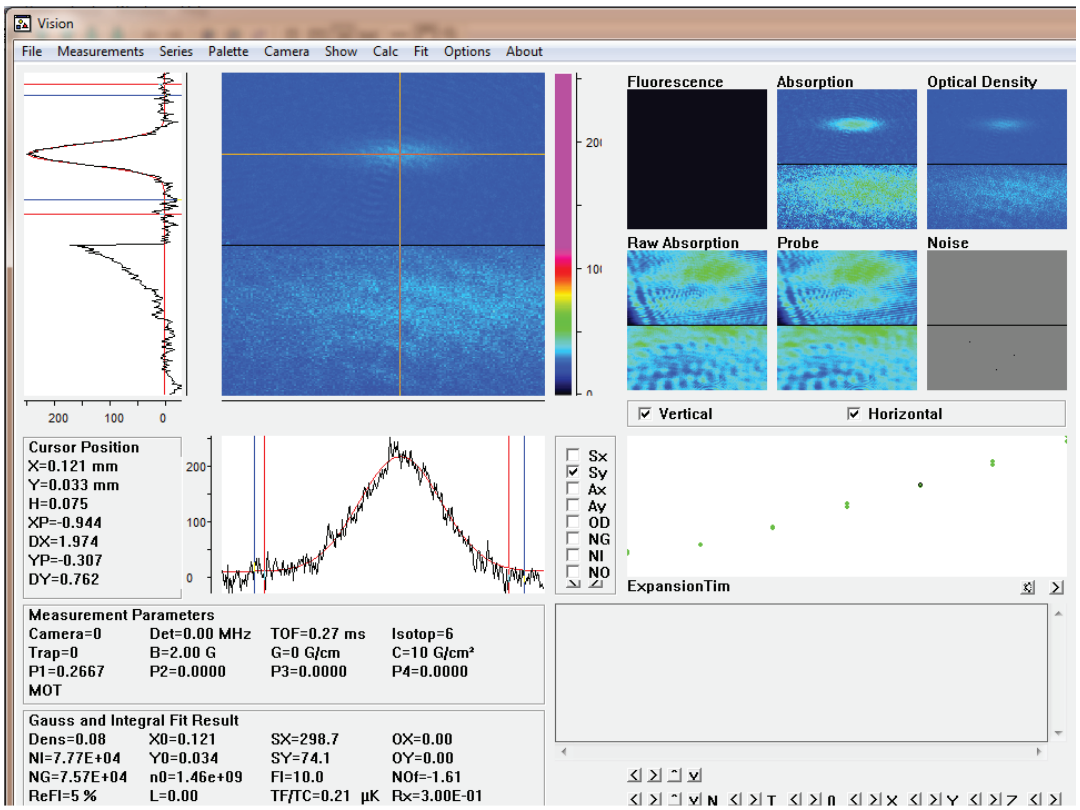

Figure 5.6: ***Vision*** graphic user interface. σ_X and σ_Y are given by SX [mm], and SY [mm] in the *Gauss and Integral Fit Result* box at the bottom of the picture.

position distributions. When the gas is released, it will begin to expand and its $1/\sqrt{e}$ radius, or $\sigma(t)$, will evolve according to

$$\sigma(t) = \sqrt{(\sigma(t=0))^2 + \frac{k_B T}{m}\sigma_v^2} \tag{5.27}$$

where σ_v^2 is the variance of the velocity distribution, T the absolute temperature, and m the mass of the atom. To extract the temperature, $\sigma(t)$ has to be measured for different times and fit to equation (5.27). The radii of the expanding clouds are calculated by fitting Gaussian distributions to the absorption images. Figure 5.6 shows a screenshot of our program Vision as we find the size of a typical cloud. Figure 5.7 shows a typical temperature measurement fit.

The classical fit starts deviating from the real temperatures as the sample approaches degeneracy. Still, it is very convenient to use it for several reasons: 1) It is easier

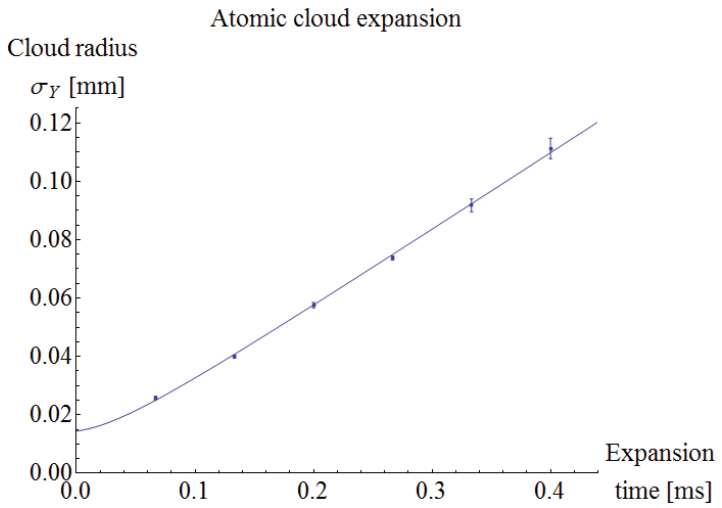

Figure 5.7: Temperature fit. A plot of the vertical $1/\sqrt{e}$ radius vs expansion time is shown in the figure. The points are fitted to equation (5.27), resulting in a temperature of $T = (50.67 \pm 0.88)\mu$K

and faster to fit than the polylog function that has to be used instead; 2) The classical fit overestimates the real temperature. Classically, as the cloud gets colder and colder, the atoms fall to the zero energy level. Due to the Pauli's exclusion principle, fermions start to stack on top of each other and start occupying higher momentum states. As the gas is released, the atoms will expand faster than they would if they behaved entirely classically. Thus, a classical fit overestimates the temperature because it would attribute the faster expansion rate to a higher temperature, not to the fact that the fermions are occupying higher momentum states.

5.5 Fringe Removal Algorithm

Interference fringes produced by the viewport glass surfaces can affect the quality of the absorption image when the absorption signal is weak. If the fringes move between the raw absorption image and the probe image, severe fringe noise will affect the quality of the image. Figure 5.8 shows the effect that fringes have on absorption pictures.

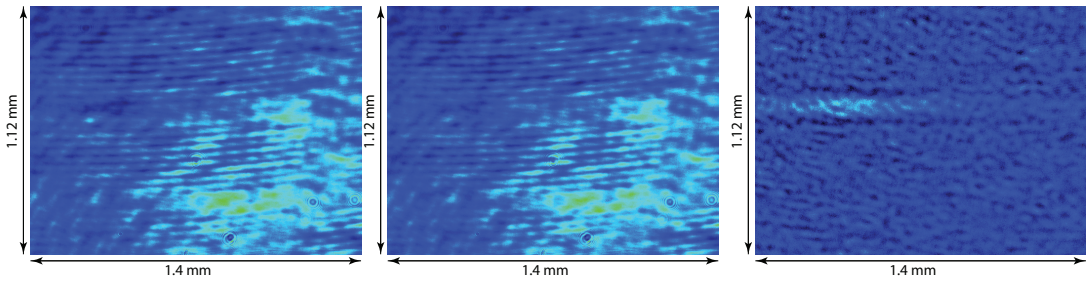

(a) Raw absorption picture (b) Probe picture. (c) Optical density

Figure 5.8: Effect of fringes on absorption pictures. a) Raw absorption picture of the atoms in the CO_2 optical dipole trap. Note the fringes in the picture. b) Probe picture. Note how the fringes moved relative to the raw absorption picture. c) Optical density. The different fringe patterns in the raw absorption picture and the probe picture affect the quality of the optical density picture so much that the atoms are barely visible.

The problem arises because the probe picture has not been able to cancel the fringes appropriately. Instead of taking many probe pictures and hoping that one of them will cancel the fringes perfectly, our approach was to ***construct*** a suitable probe picture. How to construct a suitable probe picture? Suppose we take N probe pictures and form a new probe picture as a linear combination of the N probe pictures: $\lambda_i \mathbf{P}_i$. λ_i is the coefficient of the i-th probe picture $\mathbf{P}_i$. Each $\mathbf{P}_i$ is to be regarded as a column vector that contains all the information of the picture. Let $\mathbf{R}$ represent our raw absorption picture column vector. If we exclude the region where our feature of interest is present, in our case the region where the atoms are present, then our suitable probe picture must minimize

$$S = (\mathbf{R} - \lambda_i \mathbf{P}_i)^2 \tag{5.28}$$

setting

$$\frac{\partial S}{\partial \lambda_j} = 0$$

we get

$$\mathbf{R} \cdot \mathbf{P}_j - \lambda_i \mathbf{P}_i \cdot \mathbf{P}_j = 0$$

Defining $M_{ji} = M_{ij} \equiv \mathbf{P}_i \cdot \mathbf{P}_j$ and $X_j \equiv \mathbf{R} \cdot \mathbf{P}_j$ we can rewrite the previous equation as

$$X_j = M_{ji} \lambda_i \tag{5.29}$$

from which we can solve for λ_i:

$$\lambda_i = (M_{ij})^{-1} X_j \tag{5.30}$$

Applying equation (5.30) to absorption imaging improves the image quality considerably. Figure 5.9 shows the effect that the fringe removal algorithm has on the absorption pictures.

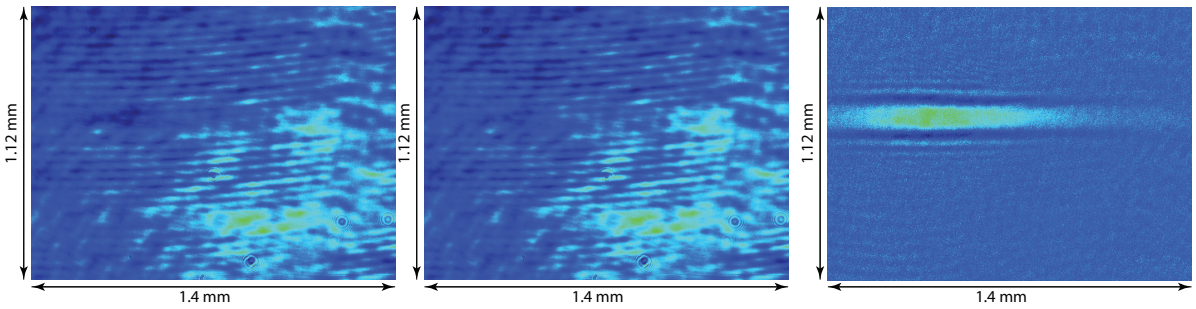

(a) Raw absorption picture (b) Probe picture. (c) Optical density

Figure 5.9: Effect of the fringe removal method. a) Raw absorption picture of the atoms in the CO_2 optical dipole trap. Note the fringes in the picture. b) Constructed probe picture. A probe picture is formed by a linear combination of many other probe pictures such that it minimizes equation (5.28). c) Optical density. A much cleaner optical density picture is extracted from the raw absorption and constructed probe pictures. The atoms are clearly visible and measurements such as size and atom number are now possible.

Part III

The Experiment

Chapter 6

Experimental Setup

6.1 Vacuum Chamber

Quantum states are extremely fragile; a single collision with a gas molecule can destroy them. Therefore, vacuum pressures of less than 10^{-10} torr are necessary to study such systems. At these pressures, the mean free path is greater than 700 m, ensuring that the atoms will not collide with background molecules. In addition to low pressures, the vacuum system must provide appropriate optical access to cool and detect our samples of ^{6}Li , and it has to be easy to build and assemble.

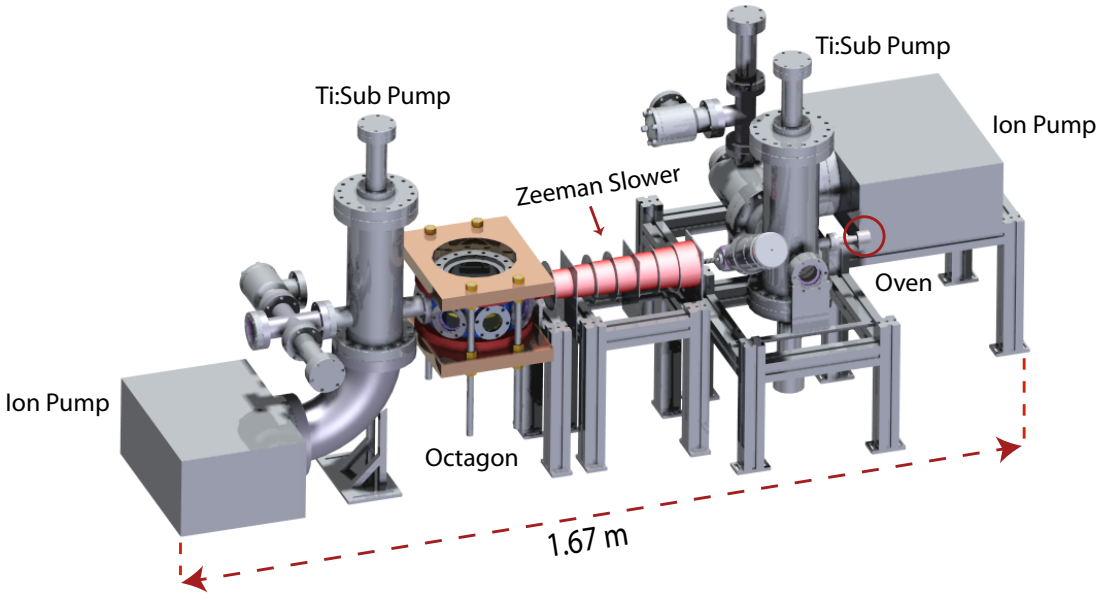

Figure 6.1: Vacuum chamber of the experiment. The total legth of the experimental setup, from ion pump to ion pump, is 1.67 m. The oven (circled in red) is wrapped in fiber glass and aluminum foil for heat insulation.

The lithium setup can be seen in fig 6.1. We decided to build our vacuum system mostly of commercially available parts, keeping modifications and homemade parts to a minimum. The support structure of the vacuum system is made of extruded aluminum, as can be seen in fig. 6.1. Experience from other experiments taught us that we should minimize the degrees of freedom of the vacuum chamber as much as possible, and to do a single, and precise alignment during assembly. There is only one bellows in the whole vacuum system; this bellows connects the oven chamber to the differential pumping tube and allows for angular adjustment. The alignment of the diffusive beam path, from the oven to the Zeeman slower window, was checked meticulously with a telescope. Once the structure is aligned, everything is locked down and no further adjustment is possible.

6.1.1 Oven Chamber

The oven is located at the very beggining of the vacuum setup (see figures 6.1 and 6.4). The oven itself (see fig. 6.2) is made of stainless steel, it has an outer diameter of 1.5 inches, holds up to 4 grams of lithium, and can be heated to temperatures of 370 °C and above using a band heater. We wrapped several layers of fiber glass and aluminum foil around the oven to avoid unnecessary heat loss and protect against the intense heat. The oven is attached to the oven chamber with a nickel gasket. A nickel gasket must be used to attach the oven since hot lithium can corrode copper gaskets and cause vacuum leaks over time.

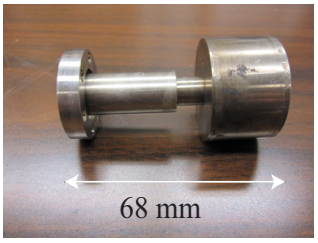

Figure 6.2: The lithium oven. The lithium oven can be filled with up to 4 grams of lithium. Its outer diameter is 1.5 inches and has a total length of 68 mm. The walls have been reduced to decrease the heat flow to the rest of the chamber.

During the experimental sequence, it becomes necessary to turn the effusive beam on and off to avoid buildup of lithium on the chamber windows. An atomic beam shutter (see fig. 6.3) was placed inside the oven chamber and connected to a stepper motor through a rotary feed through (Accuglass Products Inc., HTR-133). Between the oven

and the beam shutter, an atomic beam block (see fig. 6.3) with a 5 mm diameter hole collimates the beam.

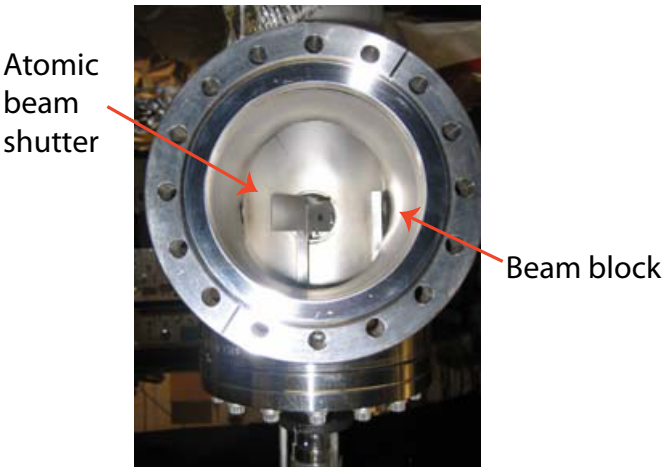

Figure 6.3: Atomic beam shutter. The atomic beam shutter shown in the figure was polished like a mirror to aid in the alignment of the Zeeman slower. It is connected to a stepper motor through a rotary feed through (Accuglass Products Inc. HTR-133). The atomic beam block has a hole of 5 mm that collimates the effusive beam.

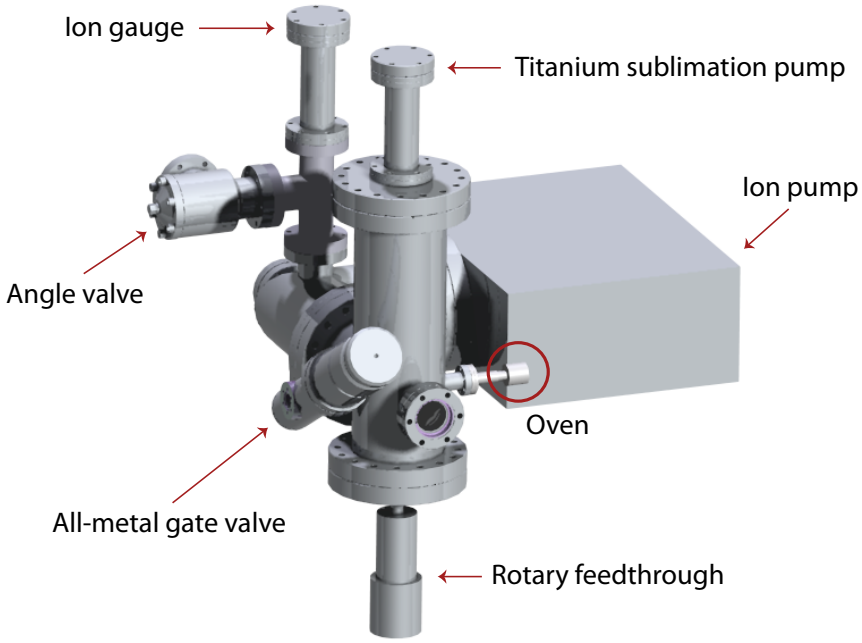

Figure 6.4: The oven chamber. Connected to the oven tower are: the oven (circled in red), a titanium sublimation pump (Duniway Stockroom, TSP-275-003), an all-metal gate valve (VAT Valve, 48124-CE01), and an elbow. Connected to the elbow are: an angle valve (VAT valve, 54032-GE02), a 60 L/s ion pump (Duniway Stockroom, VA-60-TR), and an ion gauge (Duniway Stockroom, I-NUDE-F), with its ion gauge controller (Granville Phillips, 350).

An all-metal gate valve (VAT Valve, 48124-CE01) separates the oven chamber from the science chamber; this way we can break vacuum in the oven chamber to refill the lithium oven and still maintain vacuum in the science chamber.

6.1.2 Differential Pumping Tube

The differential pumping tube connects the high pressure (10^{-9} torr) oven chamber with the low pressure (10^{-10} torr) science chamber. It is connected to the gate valve through a small bellows (Standard Bellows Company, 64-34-1-EE). Longer differential pumping tubes with smaller inner diameters yield larger pressure differentials, but at the same time they reduce the atomic flux. Since the differential pumping tube also forms part of the Zeeman slower, a compromise between length and inner diameter had to be found. Ultimately, the design of the Zeeman slower coils and the differential pumping tube depend on each other.

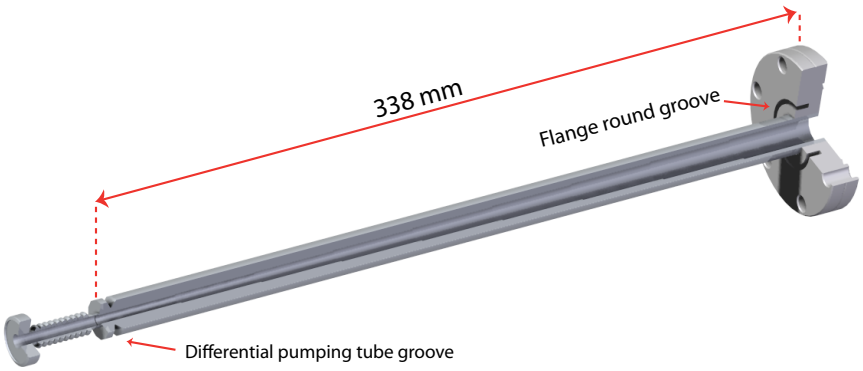

Figure 6.5: Differential pumping tube. The inner diameter of the differential pumping tube changes 9 times, from an initial diameter of 13 mm to a final diameter of 5 mm. The tube is welded to a flange with a ground groove, where the Zeeman slower coils' holding tube is embedded. A groove on the differential pumping tube itself provides additional support.

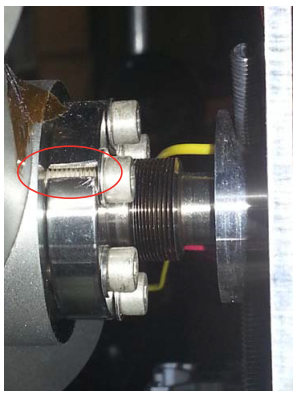

Figure 6.6: Cut flange and bellows. The bellows flange had to be cut in half to fit the Zeeman slower coils.

Since the atomic beam radius increases as the beam propagates, the inner radius of the differential pumping tube is machined to match the expected beam profile. A continuously varying diameter is hard to machine, therefore we changed the diameter in 9 steps, from an initial diameter of 5 mm to a final diameter of 13 mm (see fig. 6.5). The Zeeman slower coils had to be mounted on a supporting tube because the outer diameter of the differential pumping tube is 17 mm, while the inner diameters of the coils are 30 mm. This supporting tube is embedded into a round groove on the flange connecting it to the science chamber. A second groove on the differential pumping tube provides extra support.

The Zeeman slower coils' supporting-tube inner diameter (25 mm) is smaller than the diameter (32 mm) of the flange that connects the bellows to the all-metal valve. Therefore, to assemble the coils, we had to cut the flange in half (see fig. 6.6), slide the Zeeman slower's supporting-tube with the coils already in place, and reassemble and connect the flange to the all-metal gate valve.

6.1.3 Science Chamber

The main component of the science chamber is the **spherical octagon** (see fig. 6.7). The spherical octagon is a UHV stainless steel vacuum chamber manufactured by Kimball Physics (MFC600-SO200800); it has eight 2-3/4" CF ports and two 6 in CF ports. One 2-3/4" CF port connects the spherical octagon to the Zeeman slower

differential pumping tube; the opposite one connects it to the second tower via a 6 in nipple.

Four of the eight 2-3/4" ports are sealed with broadband anti-reflection coated viewports (MDC, 450002) for the wavelength range from 650 to 1200 nm (Thinfilm Labs). The remaining two 2-3/4 in CF ports are attached with two zinc selenide (ZnSe) viewports that are AR-coated for 10.6 μm from VG Scientia.

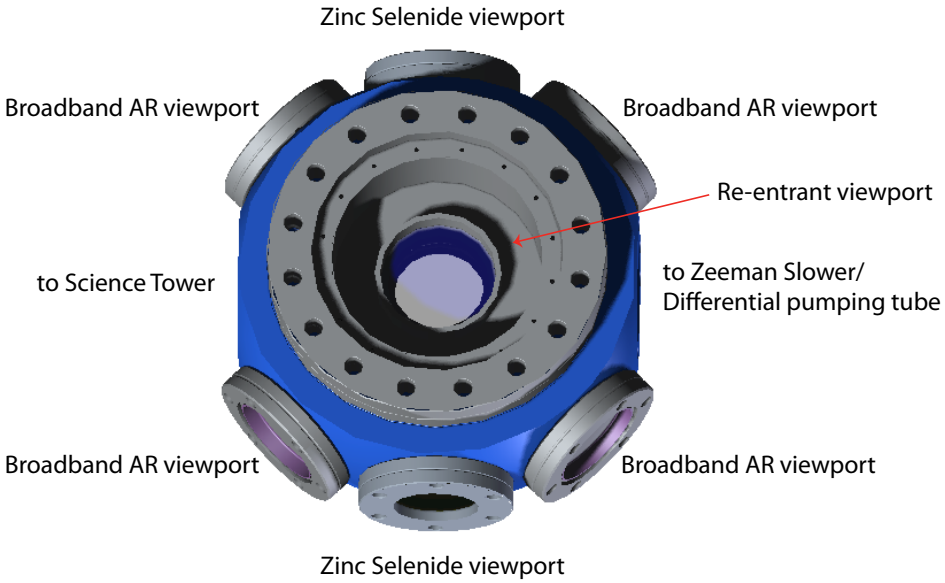

Figure 6.7: Spherical octagon.

To maximize the optical access to our sample, we attached two custom reentrant viewports (Special Techniques Group, Culham Centre for Fusion Energy, United Kingdom Atomic Energy Authority) to the two 6 in CF ports of the spherical octagon. The windows on these viewports extend inside the spherical octagon to maximize the optical access. However, the reentrant viewports cannot block the MOT or Zeeman slower beams. Therefore, this imposes a minimum separation distance between the two windows. For our design, we chose this distance to be 16.6 mm. Both reentrant viewport windows are coated with the same broadband anti-reflection coating as the four 2-3/4 in

viewports. Besides increasing optical access, the reentrant viewports allow us to mount the Feshbach coils much closer to the atoms, thus allowing us to generate fields of 834 G with 132 A.

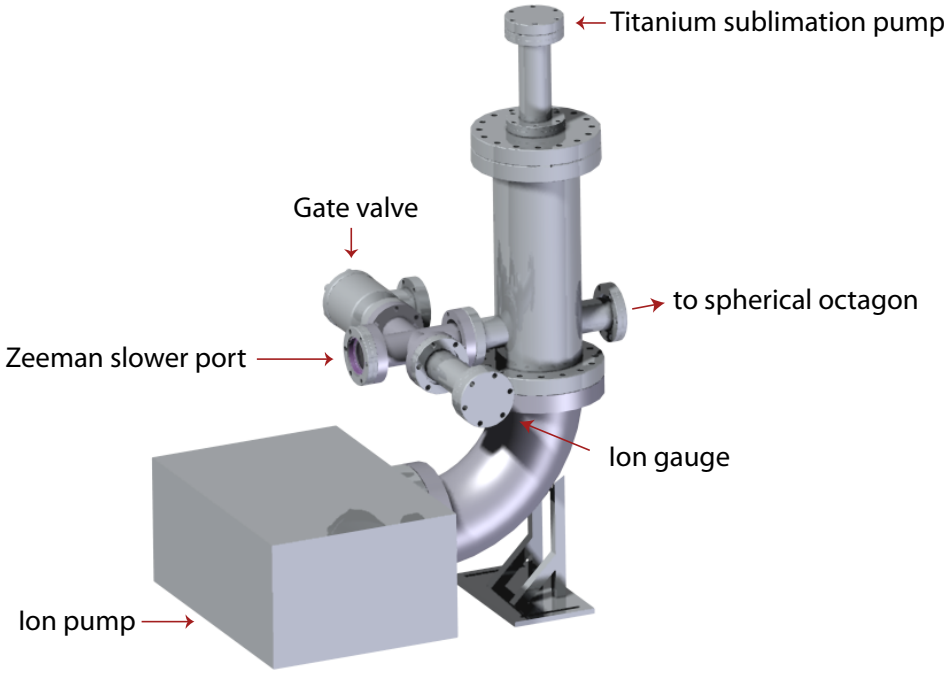

Figure 6.8: Science chamber. The science chamber consists of a 6 inch nipple (science tower), a four port 2-3/4 inch cross, and an elbow. Connected to the science tower are: a titanium sublimation pump (Duniway Stockroom, TSP-275-003), connected at the top of the tower, and an ion pump (Duniway Stockroom, RVIP-75-S), connected through the elbow to the bottom of the tower. Connected to the cross are: an ion gauge (Duniway Stockroom, I-NUDE-F) with its controller (Granville Phillips, 350), an all-metal gate valve (Vat-Valve, 54032-GE02), and a 2-3/4 inch viewport identical to the broadband ones of the spherical octagon.

The rest of the science chamber is described in figure 6.8. The last 2-3/4 inch viewport is used by the Zeeman Slower beam. All lithium atoms not trapped in the MOT end up impinging on this viewport. Therefore, to avoid lithium from coating this viewport, it is kept at a temperature of 120 °C with a band heater.

Both the second tower (6 inch nipple) and the 6 inch elbow are electropolished (by Central Electropolishing Co.) to reduce outgassing.

6.1.4 Vacuum Chamber Bake-out and Pumps

Achieving ultra high vacuum (UHV) pressures of 10^{-10} torr or less involves the use of different kinds of pumps and cleaning procedures; one cannot simply connect vacuum pumps to a vacuum chamber and expect to reach UHV pressures of 10^{-10} torr or less without first baking it out.

In our setup, two ion pumps and two titanium sublimation pumps are permanently connected to the vacuum chamber. A roughing pump and a turbo pump, connected to the chamber through two angle valves, are used once to do the initial pump-out during the bake-out. Since different parts of the chamber have different baking requirements, some parts are individually pre-baked and two bake-outs are done on the chamber. All the chamber components are thoroughly cleaned with acetone and methanol before assembly.

The following bake-out and evacuation procedure was used:

- **Air-bake** of the differential pumping tube. To remove any residual oil from machining, the differential pumping tube was heated to about 200 °C for 24 hours.
- **First bake-out**. Since the maximum baking temperature for the zinc selenide viewports is low (120 °C), they were replaced by blanks for the first high temperature (200 °C) bake-out. The lithium oven was empty during this first bake-out.

After assembly is completed, the turbo pump and roughing pump are connected, and the vacuum chamber is wrapped in heaters and aluminum foil. The roughing and turbo pumps are turned on, and when the pressure drops below 10^{-6} torr, the bake-out begins. For the first bake-out, the chamber is heated to 200 °C, which is the maximum recommended temperature for the reentrant viewports and the rotary feedthrough.

- **Second bake-out**. After the first bake-out was complete, the gate valve was closed to isolate the science chamber from the oven chamber. The blanks in the spherical octagon were replaced with the zinc selenide viewports. To prevent contamination, the science chamber was flooded with high purity argon and the blanks and zinc

selenide viewports were exchanged as quickly as possible. Since the zinc selenide AR coating is very sensitive to temperature variations, a brick oven was built around the spherical octagon to keep the temperature as constant as possible during the second bake-out. The oven chamber was flooded with high purity argon to remove the oven and a blank was loosely attached while the oven was filled with about 4 g of 95% enriched ^{6}Li (Sigma-Aldrich and Medical Isotopes Inc.). The oven was then quickly reattached with a nickel gasket.

^{6}Li is kept under oil to prevent oxidation. Even though we clean the lithium very carefully, it is not possible to remove all the residual oil from it. Furthermore, since the oven runs at at a temperature of 350 °C, it has to be baked at 400 °C to completely degas it. Since the oven and the rotary feed through are close, the walls of the oven had to be thinned (see figure 6.2) to avoid excessive heat conduction from the oven to the rotary feedthrough and the oven chamber viewport. Having the angle valve closed at this stage prevents any oil contamination from reaching the science chamber, should it occur in the oven chamber.

The oven itself was baked at around 400 °C, the octagon at 100 °C, and the rest of the chamber at 150 °C. After the bake-out process was completed, UHV pressures were finally obtained.

6.2 Magnetic Systems

Magnetic fields play a central role in many atom cooling and trapping techniques. In our experiment we use magnetic fields to exploit the Zeeman shift and a Feshbach resonance. There are three systems of coils used in the experiment, all of which were home built:

1. **Zeeman slower coils**: Eight coils produce the required magnetic field to operate the Zeeman slower.

2. **Magneto optical trap (MOT) and Feshbach coils**: The two Feshbach coils

can be used to generate a quadrupole field (uniform field) when operated in anti-Helmholtz (Helmholtz) configuration.

3. **Shim coils**: A system of four coils is used to produce an offset magnetic field. This way the center of the magneto-optical trap can be moved a few millimeters.

6.2.1 Zeeman Slower Coils

The Zeeman slower magnetic field profile is approximated with eight coils (see figure 6.9). Since the Zeeman slower and the MOT are next to each other, their magnetic fields inevitably affect each other's operation. To minimize this effect, the MOT is built in such a way that it forms part of the Zeeman slower; the axial field of the MOT completes the field at the end of the Zeeman slower, ensuring a smooth transition from the Zeeman slower to the MOT.

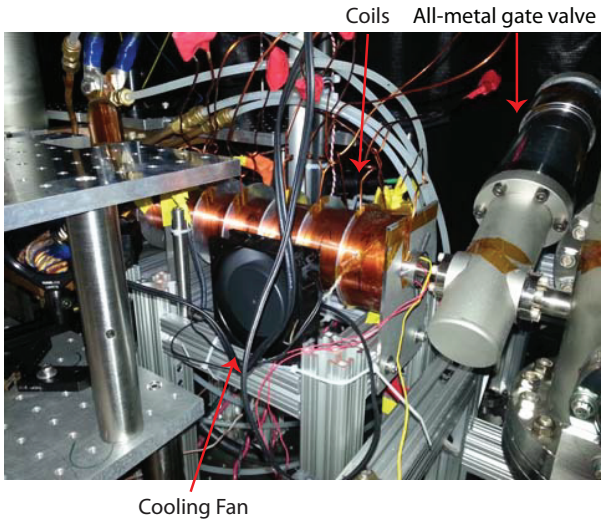

Figure 6.9: The Zeeman slower. The Zeeman slower coils can be seen in the picture. A continuously operating fan cools down the Zeeman slower. The all-metal gate valve can be seen at the right of the Zeeman slower.

The required magnetic field profile for the Zeeman slower was calculated in section 4.1. This field profile can be approximated by an array of coils by changing parameters such as the number of coils, number of turns per coils, length of each coil, and current per coil. The more coils that are used, the better the approximation to the desired field

will be. However, a compromise between a good approximation and complexity has to be made. To reduce complexity we decided to use eight coils, seven of which are operated with the same power supply. These seven coils have different numbers of windings to produce different magnetic field strengths. The last coil has its own power supply; we wanted to have independent control of this coil to better match the transition between the Zeeman slower and the MOT and to be able to use it as a shim coil as well.

A Mathematica program [38] was used to simulate the magnetic fields of both the MOT and the Zeeman slower. This program allowed us to change parameters such as the number of windings, currents, and size of coils to find a good fit to the field. However, since the field profile cannot not be perfectly matched with a finite number of coils, a second Matlab program [39] was used to simulate the efficiency of the Zeeman slower for a given approximated field profile. The Zeeman slower coil parameters are shown in table 6.1.

Coil #	Axial turns	Radial turns	Resistance	Current	Power	Outer diameter
1	26	19	0.87 Ω	4.9 A	20.9 W	85.9 mm
2	26	15	0.62 Ω	4.9 A	14.9 W	74.4 mm
3	26	13	0.51 Ω	4.9 A	12.2 W	68.6 mm
4	26	12	0.46 Ω	4.9 A	11.0 W	65.7 mm
5	26	11	0.41 Ω	4.9 A	9.8 W	62.8 mm
6	26	10	0.36 Ω	4.9 A	8.6 W	59.9 mm
7	26	8	0.26 Ω	4.9 A	6.2 W	54.1 mm
8	26	5	0.15 Ω	4.3 A	2.8 W	45.5 mm

Table 6.1: Parameters of the Zeeman slower coils

The coils are made of AWG 18 square wire (MWS Wire Industries, 40039) coated with Polyimide-ML, rated for temperatures up to 200 °C. The bare (coated) wire dimensions are 1.29 mm×1.29 mm (1.45 mm×1.45 mm).

The coils were wound on a lathe. Epoxy (Epoxy Technology, 360) was added continuously during the winding process to provide structural support to the coil. Afterwards, the coil was allowed to dry at room temperature for one day. Each coil then was baked at 100 °C for one hour to cure the epoxy completely. Finally, they were

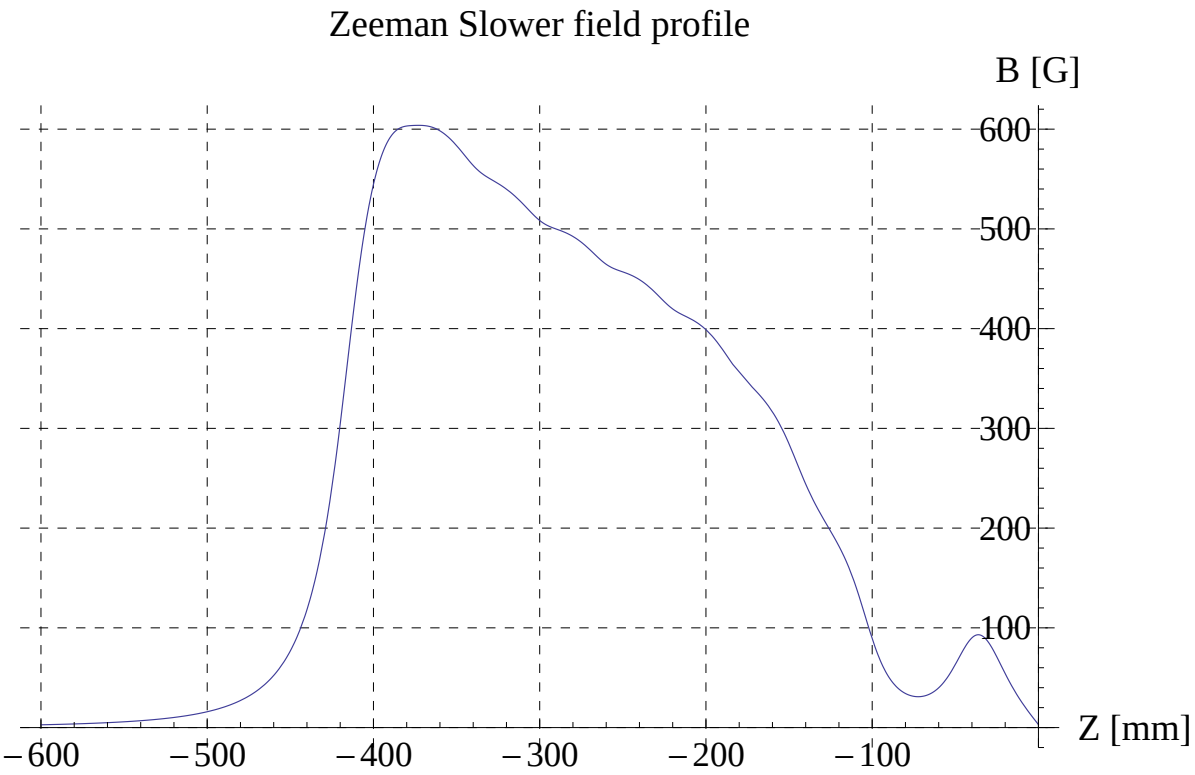

Figure 6.10: Zeeman slower field profile. The expected profile of the Zeeman slower and MOT when 4.9 A of current run through coils 1-7 of the Zeeman slower, 4.3 A run through coil 8 of the Zeeman slower, and 20 A run through the Feshbach MOT coils.

assembled in the Zeeman slower's coil holding tube.

The current for the first seven coils is supplied by a Sorensen power supply (DCR40-35A), while the current for the last coil is provided by a Kepco power supply (36-15M). All the coils are driven by a homemade current controller. The current controller features two Arduino Duemilanove microcontrollers that monitor the coils' temperatures and currents, and two home-made PID controllers that set and stabilize the currents. An additional relay box can invert the current flow of the last coil. The current controller is controlled by Control (see section 6.6) through analog and digital outputs. From Control, one can change the currents flowing through the slower, as well as the current direction of the last coil.

The power dissipated by the first seven coils of the Zeeman slower is around 84 Watts. While this does not justify water cooling, a continuously running fan was installed

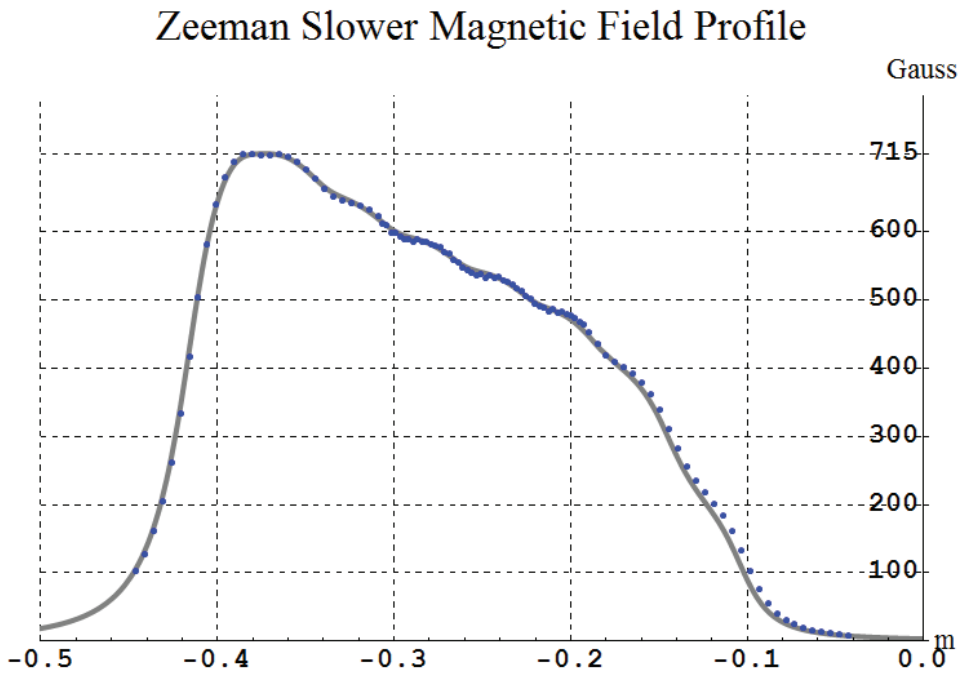

Figure 6.11: Zeeman slower field profile. The solid line represents the calculated field when 5.8 A of current run through coils 1-7 and 4.9 A run through coil 8. The blue dots are field measurements taken with a gaussmeter. The field excludes the fields from the MOT coils. The actual currents used in the experiment are 4.9 A for coils 1-7 and 4.3 A for coil 8 (actual values not shown).

to cool the Zeeman slower. This allows us to run the Zeeman slower continuously for more than 20 minutes.

To verify that the actual field matched the expected field, we measured the magnetic field of the Zeeman slower running 5.8 A of current through coils 1-7 and 4.9 A through coil 8. These were the original values for the currents and thus are the ones we used for comparison to our fit. The results are shown in figure 6.11. The figure shows an incomplete Zeeman slower field since the final part of the Zeeman slower is completed by the MOT axial field.

6.2.2 Magneto Optical Trap and Feshbach Coils

Originally, we were going to use a pair of coils for the MOT and a separate pair of coils (the Feshbach coils) to generate a uniform magnetic field to control the

Feshbach resonances. The Feshbach coils can operate in two configurations: Helmholtz configuration, in which current circulates in the same direction in both coils and produces a uniform magnetic field midway between the coils, and anti-Helmholtz configuration, where currents circulate in opposite directions and produce a quadrupole field with a zero located midway between the coils. The Feshbach coils can be used as MOT coils when operated in anti-Helmholtz configuration. During the sequence, the atoms would first be loaded in the MOT coils, then we would transfer them to the Feshbach coils still in anti-Helmholtz configuration, after which we would compress the cloud and transfer it to the CO_2 laser. While optimizing the MOT to Feshbach-MOT transfer, we tried loading the atoms directly to the Feshbach MOT without using the original MOT coils. Since both methods had similar performance, we decided to use the Feshbach coils for the MOT instead of the original MOT coils. The original MOT coils were then modified and are now used as shim coils (see section 6.2.3).

The Feshbach coils serve two purposes: in anti-Helmholtz configuration, they complete the MOT-Zeeman slower magnetic system, and in Helmholtz configuration, they produce the homogeneous magnetic field necessary to access the 834 G Feshbach resonance of ^{6}Li .

The Feshbach resonance we use occurs at around 834 G. To generate such a field a large amount of current has to be run through the coils. Moreover, this field has to be maintained for a few seconds. To reduce the amount of current and power needed to reach this field, the coils were mounted inside the reentrant viewports so they could be closer to the atoms. The best coil parameters were found using a Mathematica program.

The inner (outer) diameters of the coils are 29.5 mm (45 mm). The coils are made of flat wire (MWS Wire Industries, 41137) with dimensions of 0.43 mm $\times$ 7.6 mm and each have 26 windings, giving a resistance of 30 mΩ for each coil. The coils are placed 36 mm apart and when operated in Helmoltz configuration produce 6.34 G/A. When operated in anti-Helmholtz configuration, only 20 A are needed to produce the axial (radial) gradient of 21 G/cm(38 G/cm) needed for the MOT operation. Notwithstanding their low combined resistance of 60 mΩ, the coils still dissipate more than 600 W each when operated at 834 G. It was therefore necessary to implement a cooling system for

the coils. The water in the cooling system flows at a rate between 2.1 and 2.4 l/min at a temperature of 18 °C. Even at a current of 150 A (B ≈ 951 G), the steady state temperature remains below 70 °C.

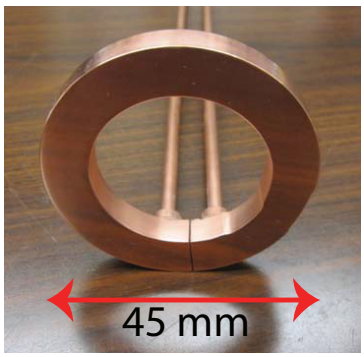

Figure 6.12: Feshbach coils heatsink. The lower face of the heatsink is polished to increase thermal contact.

Like the Zeeman slower coils, the Feshbach coils were wound on the lathe: epoxy (Epoxy Technology 360) was added as they were wound, and then the coils were baked at 100 °C to completely cure the epoxy. Unlike the Zeeman slower coils, the feschbach coils need a high power cooling system, so a pair of water cooled heat-sinks (see figure 6.12) was constructed. To maximize the heat conductivity between the coils and the heatsinks, the mating faces of each coil-heatsink pair were flattened and polished. This exposed the copper wire in the coils, so an electrically-insulating heat-conducting epoxy (AI Technology, Primabound ME 7159) had to be used to attach the coils to the heatsinks. This epoxy is a diamond filled epoxy with a thermal conductivity of 11.4 W/m·C ° and an electrical resistivity of more than 10^{24} Ω·cm. After the mating faces of the coils and heatsinks were polished, a layer of diamond filled epoxy was applied and prebaked for 30 minutes at 60 °C. The faces were then joined and the epoxy was cured for 2 hours at 140 °C.

The electrodes have round faces to maximize the electrical contact area with the flat wire. Since the electrodes and the coils act as a giant heatsink, a special indium solder wire (Indium Corporation of America, alloy 58Bi 42Sn) had to be used. This solder wire has a melting point of 138 °C and a lower electrical resistance than regular solder wires. To solder the electrodes to the coils, the coils with their heatsinks attached

are heated to 130 °C with a heater tape. The electrodes are heated in an oven to 130 °C as well. Some diamond filled epoxy is applied to the dents of the heat sink to provide some electrical insulation and support to the electrodes, then two soldering irons are used at the same time to solder the electrodes to the coils. To further add structural support, epoxy putty (Loctite, Fixmaster) is used to attach the electrodes to the heatsinks. The Feshbach coils' current is supplied by a Lambda power supply (ESS 20-500), that can supply up to 500 A at 20 V with a current stability of 0.1%. The value of the current is directly controlled by the power supply, while the coil configuration is changed with an external H-bridge driver. Figure 6.13 shows the H-bridge driver circuit diagram. The driver consists of four sets of MOSFETs (IRF1324PbF) connected to an H-bridge driver (HIP4081). The driver is controlled directly by the computer program Control.

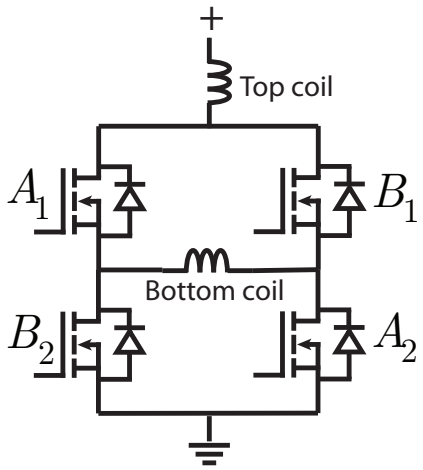

Figure 6.13: H-bridge circuit diagram. The H-bridge controls the direction of the current in the bottom coil by switching on and off different pairs of MOSFETs. When A_1=ON, A_2=ON, B_1=OFF, and B_2=OFF, current flows from left to right. When A_1=OFF, A_2=OFF, B_1=ON, and B_2=ON, current flows from right to left.

Each MOSFET set consists of ten MOSFETs in parallel, mounted on a water cooled copper plate as seen in figure 6.14. Since each MOSFET can take up to 195 A, a set of ten can in principle take 1950 A, leaving a large safety margin and a very fault tolerant design. To reduce the switching time, the length and area enclosed by the cables are minimized as much as possible.

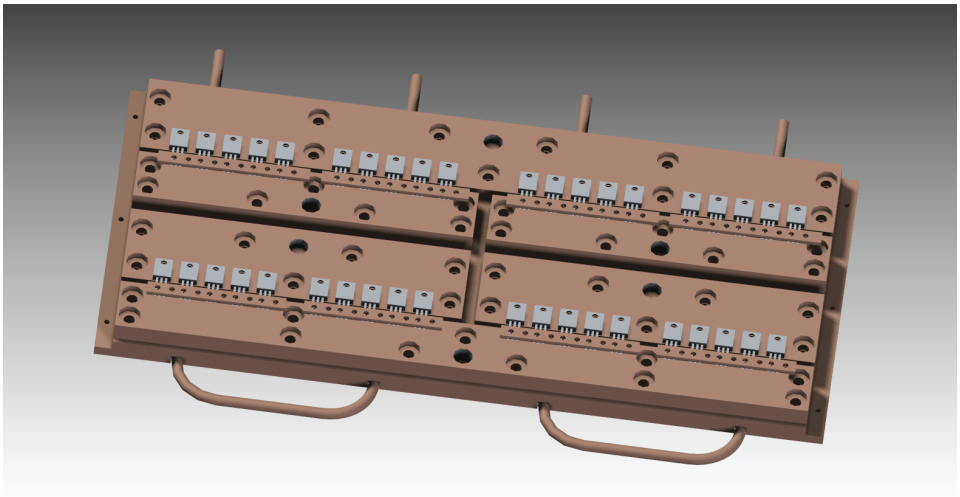

Figure 6.14: MOSFET bank. 40 MOSFETS (IRF1324PbF) are connected to an H-bridge driver (HIP4081). Each of the four banks shown in figure 6.13 consist of 10 MOSFETs in parallel. Each MOSFET can take up to 195 A, so each bank can take at least 1950 A. The MOSFETs are mounted on a copper plate that has incorporated water cooling. *Figure courtesy of Kirsten Viering.*

The expected magnetic field profile for the Helmholtz configuration is shown in figure 6.15. By taking absorption pictures at high fields we concluded that the fields are accurate to within 1 G.

6.2.3 Shim Coils

The shim coils are used to move the center of the quadrupole field of the MOT. The last coil of the Zeeman slower is used as the x-axis (Zeeman slower axis) shim coil; the direction and amount of its current can be controlled independently from the other coils. The original MOT coils (see figure 6.16) are used as a pair of shim coils for the vertical direction (y-axis). Although each can be independently controlled, the current direction is fixed, so they are configured in anti-Helmholtz configuration to increase their range. Finally, an extra coil was installed on the exiting zinc selenide viewport to serve as a shim coil (z-direction, CO_2 laser propagation). The shim coils current values are set during the MOT holding phase, just after the loading is over.

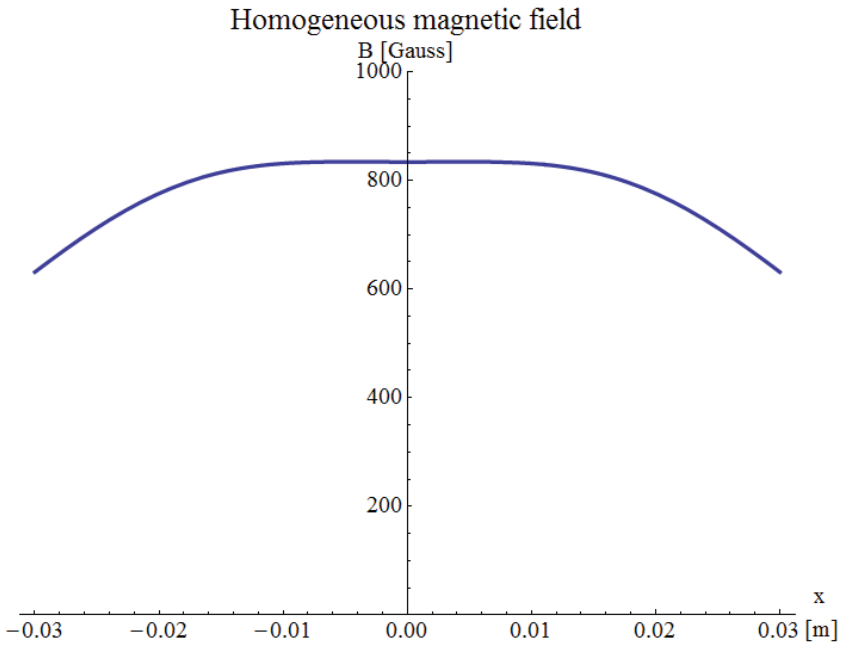

Figure 6.15: Homogeneous magnetic field produced by the Feshbach coils when operated at 131 A in Helmholtz configuration

6.2.4 Water Cooling of the Magnetic System

The currents needed to operate the MOT and to reach the Feshbach resonance require us to water cool the coils and the H-bridge. A diagram of this system can be seen in figure 6.17

We use a heat-exchanger (Affinity, EWA-04AA-CE56CB) connected to a water flow of chilled water through an externally controlled valve (Johnson Controls, VA-4233-6GA-24). A home-built temperature controller featuring an Arduino Duemilanove microcontroller probes the water temperature with a thermocouple and accordingly opens and closes the valve to keep the temperature at approximately 18 °C.

Right after the water output of the heat exchanger, a water filter is installed to prevent water lines clogging. Since the heat exchanger cannot generate enough output pressure, a pair of pumps (Tuthill, TXS2.6PPPT3WN1C000) are used to increase the water flow rate. Two pulsation dampers (FlowGuard) are added in series with the pumps to suppres mechanical vibrations.

The cooling lines for the the Feshbach coils, the shim coils, and the H-bridge, all

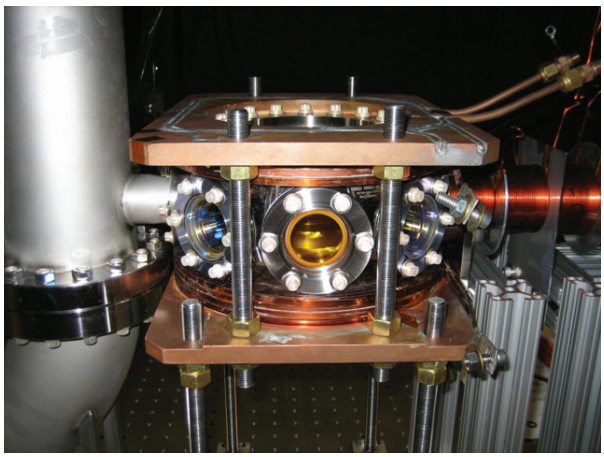

Figure 6.16: Spherical octagon in the setup. The old MOT coils can be seen. These coils are now used as shim coils in the vertical direction.

are connected in parallel. Figure 6.18 shows our brass home-built distribution system used to split and combine the water lines. Finally, there is a flow meter measuring the water flow returning to the heat exchanger. If the flow is less than expected, either due to a clog or a leak, the interlock boxes controlling the electrical currents in the coils will stop any electrical current flow, preventing potential damage to the experiment.

6.3 Near Resonant Lasers Systems

The near resonant laser system is used for the MOT, the Zeeman slower, fluorescence detection, and absorption imaging. The laser system consists of three Toptica units: two low power diode lasers (Toptica, DLpro), each with an output power of approximately 20 mW, and one tapered amplifier with its own laser diode (Toptica, TApro), with an output power of approximately 400 mW.

One of the DLpro modules is used to lock the frequency of the laser to the $\left|^2S_{1/2}, F = 3/2\right\rangle$ to $\left|^2P_{3/2}\right\rangle$ line of lithium-6. The TA and imaging lasers are then locked to the spectroscopy laser. The TA supplies power for the Zeeman slower, the MOT, fluorescence detection and absorption imaging. The imaging laser provides extra power for imaging. All the lasers are located in a separate optical table and are coupled to single mode optical fibers that are sent to the main optical table. The fiber coupling efficiencies

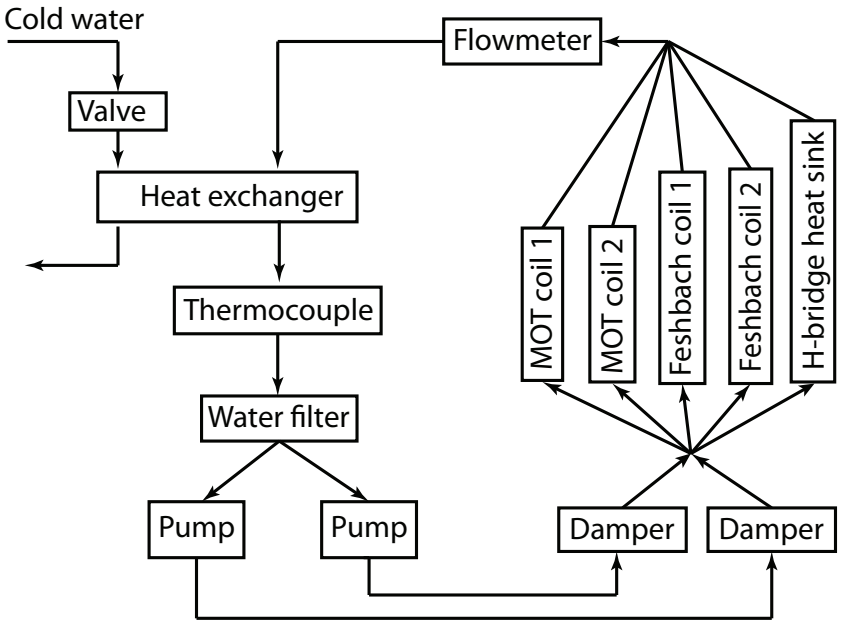

Figure 6.17: Water cooling system diagram. The magnetic system water cooling system services the MOT coils, the Feshbach coils, and the H-bridge heatsink.

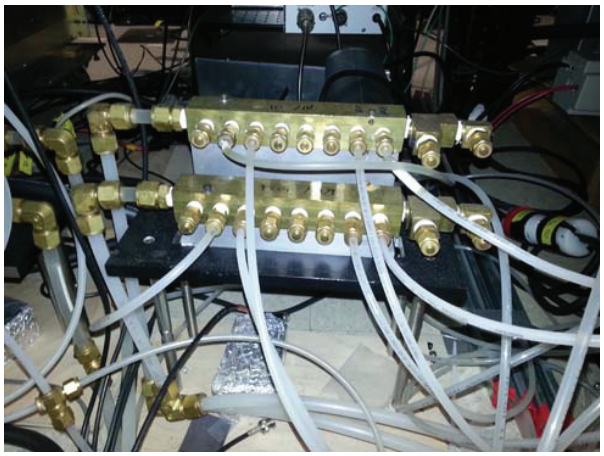

Figure 6.18: Distribution system for the water cooling system shown in figure 6.17

are typically around 40%, but can be as high as 60%. There are two advantages of using fibers: first, since they are single mode they serve as spatial filters; second, they decouple the optical alignments from before and after the fiber. The laser system will now be described in more detail.

6.3.1 Spectroscopy Cell and Laser

The spectroscopy cell is used to lock the spectroscopy laser (Toptica, DLpro) to the $\left|^2S_{1/2}, F = 3/2\right\rangle$ to $\left|^2P_{3/2}\right\rangle$ line of lithium 6. We use Doppler free frequency modulation spectroscopy to lock our master laser to the lithium-6 D_2 line. The necessary electronics for this technique have been implemented in the laser modules of the Toptica system.

The beam profile coming out from the spectroscopy laser has an elliptical profile, so a pair of anamorphic prisms (Thorlabs, PS871-B) are used to make it more circular. Immediately after that, an optical isolator (Conoptics, 712B) protects the laser from any reflections. A beam splitter picks up around 15 mW of light to lock the TA and the imaging laser, the rest is sent through a telescope (f1=50 mm, f2=200 mm) with a 300 μm pinhole at the focus to further clean the mode. The resulting beam is sent through a quartz half-wave plate (CVI-MellesGriot, PBS-670-050) to rotate the linear polarization of the beam, so that the polarizing beam splitter (PBS) that follows reflects all the power to the spectroscopy cell. After the polarizing beam splitter, a quarter-wave plate turns the linearly polarized light into circularly polarized light, so that the transition $\left|^2S_{1/2}, F = 3/2\right\rangle$ to $\left|^2P_{3/2}\right\rangle$ can be excited. The beam is then retroreflected, goes through the quarter-wave plate again, turns into linearly polarized light, goes through the cube, hits a mirror, and then a lens focuses it to a ultra-fast photodetector (New Focus, 1801). The laser diode current is modulated at 20 MHz by the PDD module of the laser. This produces two sidebands at $\pm$ 20 MHz of the carrier frequency. The laser beam contains these two extra frequencies and which results in amplitude modulation after the beam double passes the lithium cell. The AC-coupled output voltage of the photodetector is then fed to the input of the Pound-Drever-Hall module of the laser, which generates an error signal that can be used to lock the laser. The error signal can be seen in figure 3.2

The spectroscopy cell is made of stainless steel and is filled with argon gas at a pressure of 35 mTorr when it is at room temperature. The amount of gas inside the cell is important, as it serves as a buffer gas: with too much broadening effects will affect the spectroscopy signal, and if not enough the mean free path of lithium will be long enough to reach the viewports and coat them. The viewports are broadband anti-reflection coated for 400 nm to 700 nm (Larson glass). A schematic of the spectroscopy cell optical setup can be seen in figure 6.19

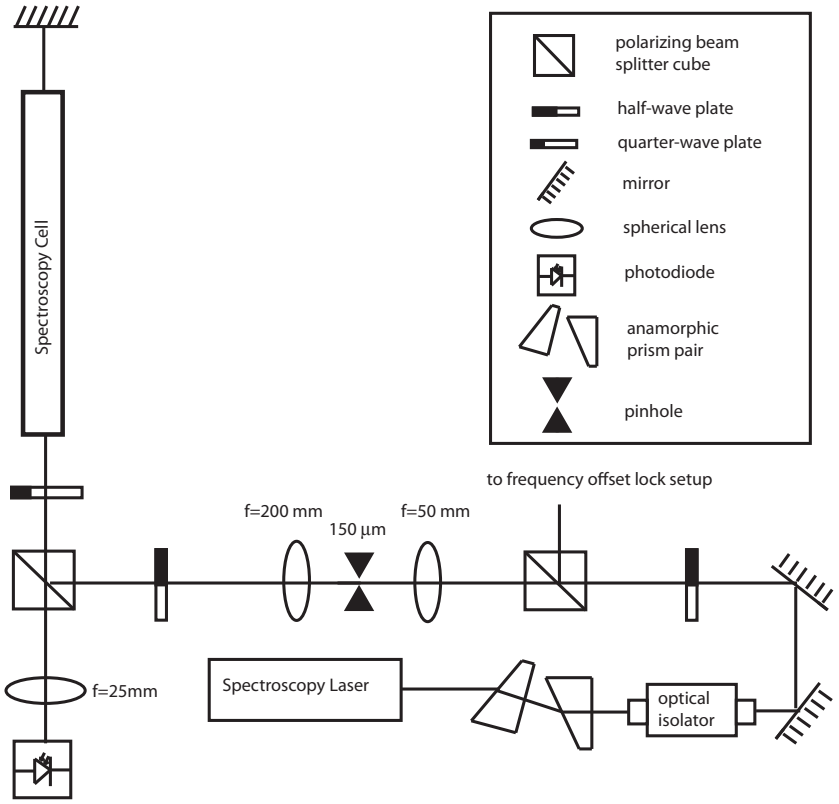

Figure 6.19: Spectrocopy cell optical setup.

A small amount of 95% enriched lithium-6 is deposited in the lithium reservoir. The cell operates at a temperature of 420 °C. At this temperature the pressure is enough to both see a spectroscopy signal and effectively contain the lithium close to the oven. The oven is heated with a fiber glass wire heater (93.8 Ω, 120 W, 480 °C max) that is wound around the oven tightly. It is wrapped with a few layers of fiberglass wrapped in wrinkled aluminum foil. Wrinkles are important because they trap air in between. The

oven has a small housing to prevent air currents from destabilizing the temperature.

A small valve (VAT Valve, 54024-GE02-0001) is connected to the 2-3/4 flange tee. This valve is used to connect the vacuum pumps used for the initial pump-out. First, the spectroscopy cell is tested for leaks without lithium. Then it is flooded with argon and lithium is added quickly. Finally, the cell is evacuated until a pressure of approximately 35 mTorr is reached.

6.3.2 Tapered Amplifier

The Tapered Amplifier (Toptica, TApro) is used to power the Zeeman slower beam, all MOT beams, and one absorption beam. The schematic of the laser setup can be seen in figure 6.21. There is a pickup mirror inside the TA that picks a small amount of light to be used to lock the laser to the spectroscopy laser. This is done with the beatlock technique. Figure 6.20 shows a diagram of the RF electronic components used to generate the error signal.

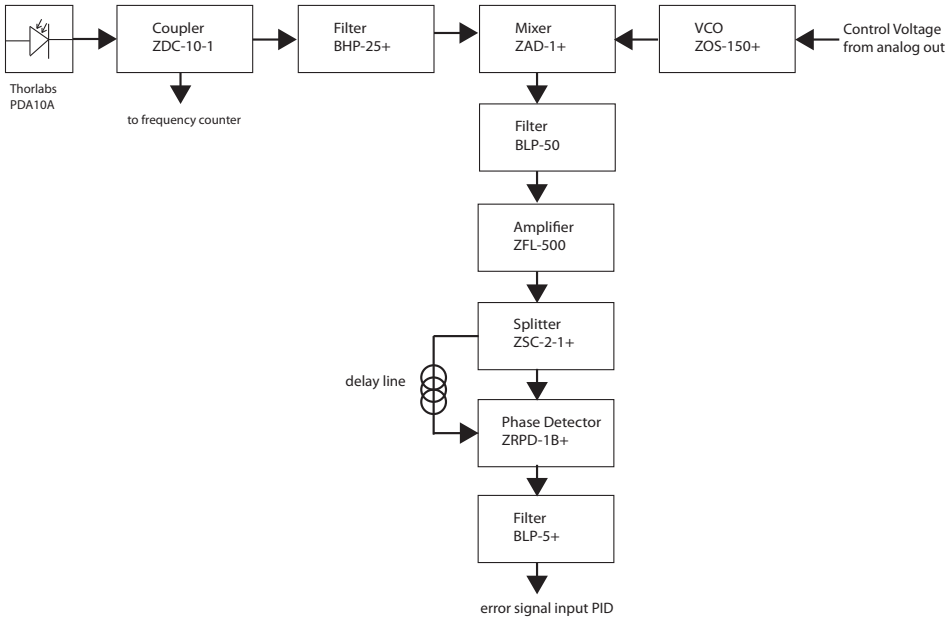

Figure 6.20: Tapered amplifier beatlock electronics. *Figure courtesy of Kirsten Viering.*

Coming out from the TA, the beam goes through an optical isolator (Conoptics, 716) with a high isolation ratio (56 to 60 dB). This is necessary as the TA is more

sensitive to back reflection. After the isolator, a 5:3 cylindrical telescope is used to make the beam profile more symmetric. This is important as the coupling efficiencies of the fibers depend on the beam profile. Next, a 5:1 spherical telescope changes the size of the beam to match the active areas of the MOT and repump AOMs (IntraAction, ATM114-A1). After the telescope, a half wave-plate and a polarizing beam splitter split the beam into two, with a typical ratio of MOT:RP=3:1. Figure 6.22 shows how the frequencies are shifted by the AOM's and the beatlock. The MOT AOM shifts the frequency by -114 MHz, while the repump AOM shifts the beam by +114 MHz. The difference between these two shifts is 228 MHz, exactly the hyperfine splitting between the $|F = 3/2\rangle$ and $|F = 1/2\rangle$ states of the ground state.

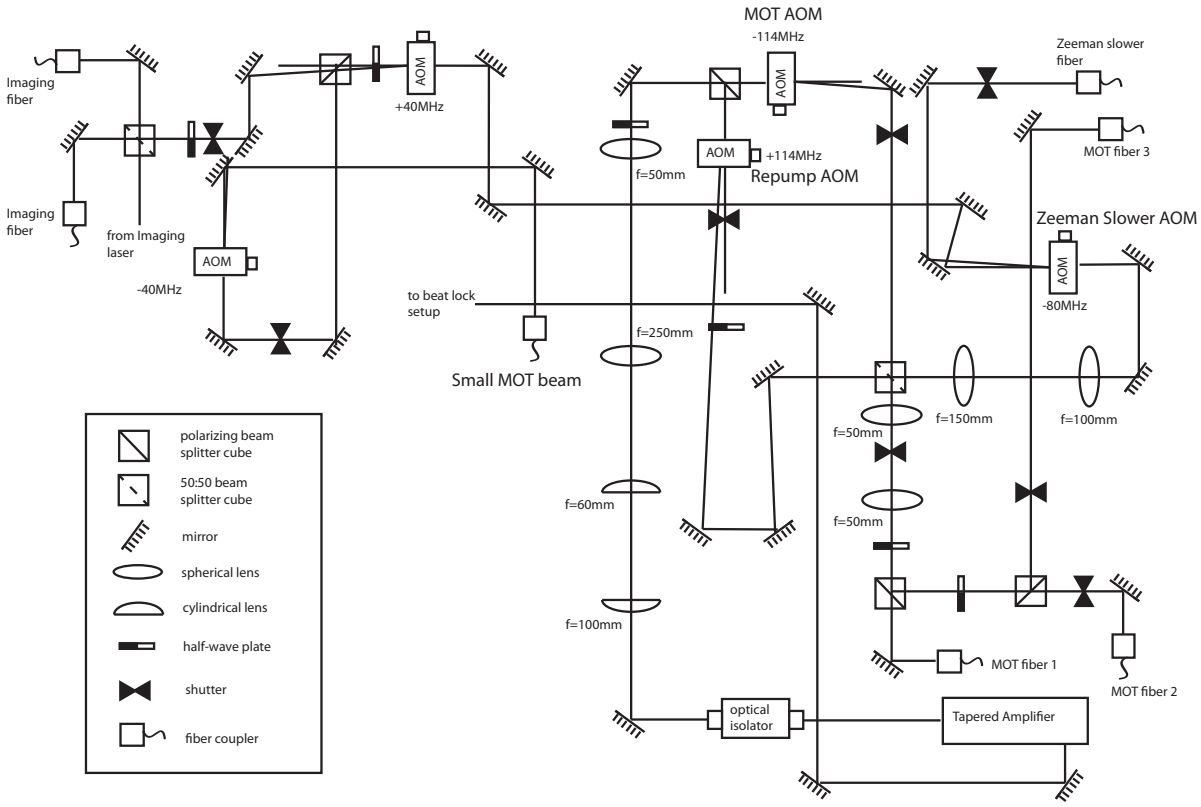

Figure 6.21: Tapered amplifier optical setup

The final frequency for each branch is,

$$\omega = \omega_0 + \delta_{\text{offset}} \pm 114\text{MHz} \tag{6.1}$$

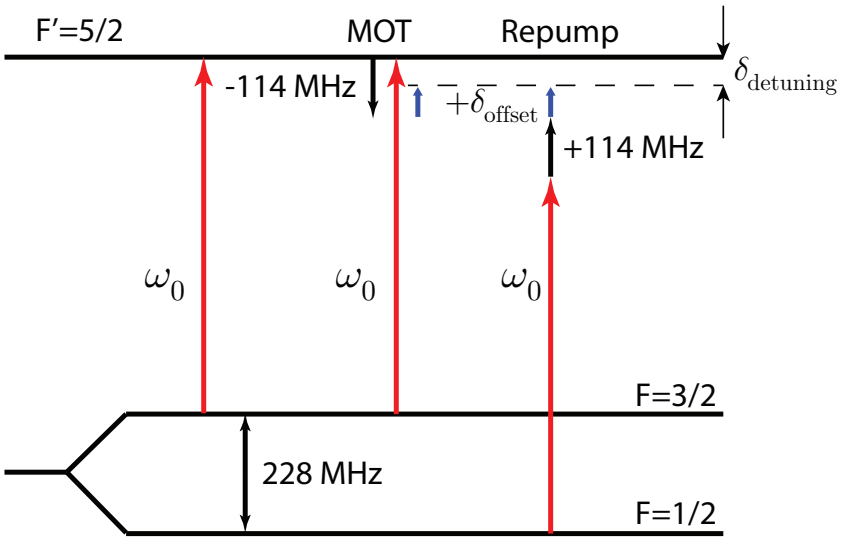

Figure 6.22: Beat lock detuning diagram. Shown in red is ω_0, the on-resonant frequency for the D_2 line transition. All red arrows are the same length. The MOT AOM shifts this frequency by -114 MHz (black arrow pointing down), while the repump AOM shifts the frequency by +114 MHz (black arrow pointing up). Then both frequencies are shifted by $+\delta_{\text{offset}}$ (blue arrows pointing up), leaving the MOT with a detuning of $\delta_{\text{MOT}} = \delta_{\text{detuning}} = \delta_{\text{offset}} - 114$ MHz from the $|F = 3/2\rangle$ to $|F' = 5/2\rangle$ transition (the MOT transition), and the repump with a detuning of $\delta_{\text{repump}} = \delta_{\text{detuning}} = \delta_{\text{offset}} - 114$ MHz from the $|F = 1/2\rangle$ to $|F' = 5/2\rangle$ transition (the repump transition). The separation between the $|F = 1/2\rangle$ and $|F = 3/2\rangle$ ground states is 228 MHz.

where ω_0 is the transition frequency $\left|^2S_{1/2}, F = 3/2\right\rangle$ to $\left|^2P_{3/2}\right\rangle$, δ_{offset} is the beatlock offset, and +114 MHz (-114MHz) corresponds to the repump (MOT) AOM frequency shift. The detuning from the spectroscopy line is then,

$$\delta_{\text{detuning}} = \omega - \omega_0 = \delta_{\text{offset}} \pm 114\text{MHz} \tag{6.2}$$

where $\delta_{RP} = \delta_{\text{offset}} + 114$MHz and $\delta_{MOT} = \delta_{\text{offset}} - 114$MHz. When $\delta_{\text{offset}} = 114$, $\delta_{RP} = +228$ MHz and $\delta_{MOT} = 0$ MHz. This means that the MOT is on resonance with the $\left|^2S_{1/2}, F = 3/2\right\rangle$ to $\left|^2P_{3/2}\right\rangle$ transition, and the repump is on resonance with the $\left|^2S_{1/2}, F = 1/2\right\rangle$ to $\left|^2P_{3/2}\right\rangle$ transition (which is +228 MHz blue detuned from the

$\left|^2S_{1/2}, F = 3/2\right\rangle$ to $\left|^2P_{3/2}\right\rangle$ transition).

Since both the Zeeman slower and the MOT need both frequency components, the beams are combined in a 50:50 beam splitter cube. This results in two beams containing both frequencies. One of these beams is further split into 3 more beams that are coupled into fibers that power the MOT. The other beam powers the Zeeman slower. Since the Zeeman slower operates at 80 MHz red detuned relative to the MOT, the beam is first resized in a telescope before passing through an 80 MHz AOM (IntraAction, AOM802). The $m = -1$ order (-80 MHz shift) of the AOM is then coupled to the Zeeman slower fiber, while the $m = 0$ order of the Zeeman slower beam is then used to power the small MOT beam, used to do fluorescence detection, and two absorption imaging beams.

The optical setup around the spherical octagon can be seen in figure 6.23. The light coming out of each fiber is linearly polarized, so a quarter wave-plate is inserted to make it circularly polarized. An additional quarter wave-plate before the mirror changes the polarization of the light to linear, then to circular again, with the same handedness. Since the axis of fiber No. 2 is used for imaging as well, the corresponding mirror and quarter wave-plate were mounted on a flipper that can be lifted to take images of the atoms. The polarized beam splitter after fiber 2 is used to couple light from the imaging fiber 1, which is the one used to take absorption pictures.

6.3.3 Imaging Laser

The imaging laser is used for absorption imaging at high fields. It is beatlocked to the spectroscopy laser in the same way as the TA. The optical setup can be seen in figure 6.24 and the beatlock electronics can be seen in figure 6.25.

Coming out from the imaging laser, the beam has an elliptic profile that is corrected by an anamorphic prism pair. An optical isolator (Conoptics, 712B) is added after the prism pair to avoid damage from back-reflections. Next, a plate beam splitter picks off around 1 mW of power to be used for frequency-offset lock and the Fabry-Perot cavity. The rest of the beam passes through an 80 MHz AOM (IntraAction, ATM801-A1). The main purpose of the AOM is to quickly turn ON and OFF the beam, as short pulses (≈ 10 μs) are needed for absorption imaging.

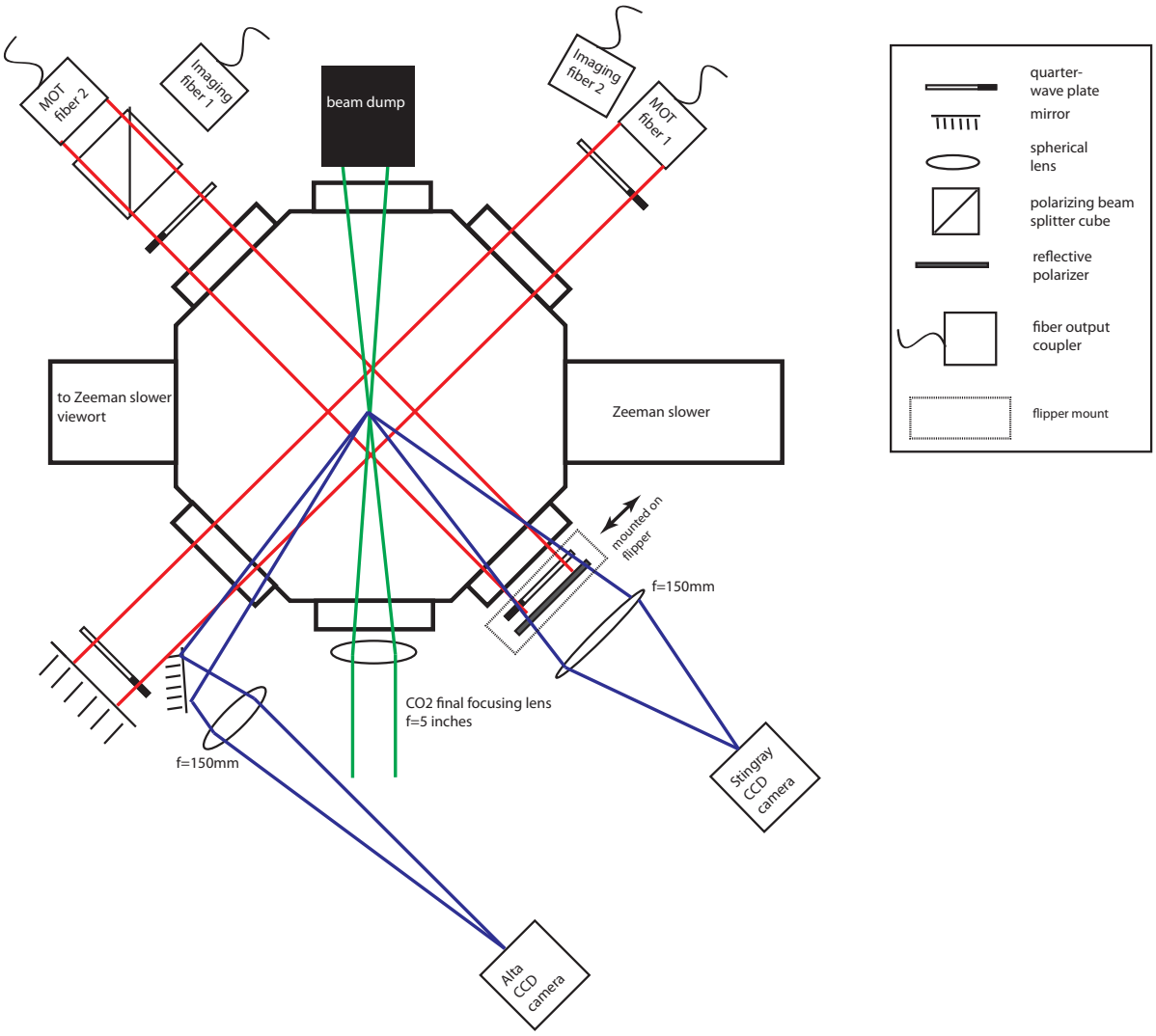

Figure 6.23: Spherical octagon optics. The red beams represent MOT beams. The blue beams represent imaging paths.

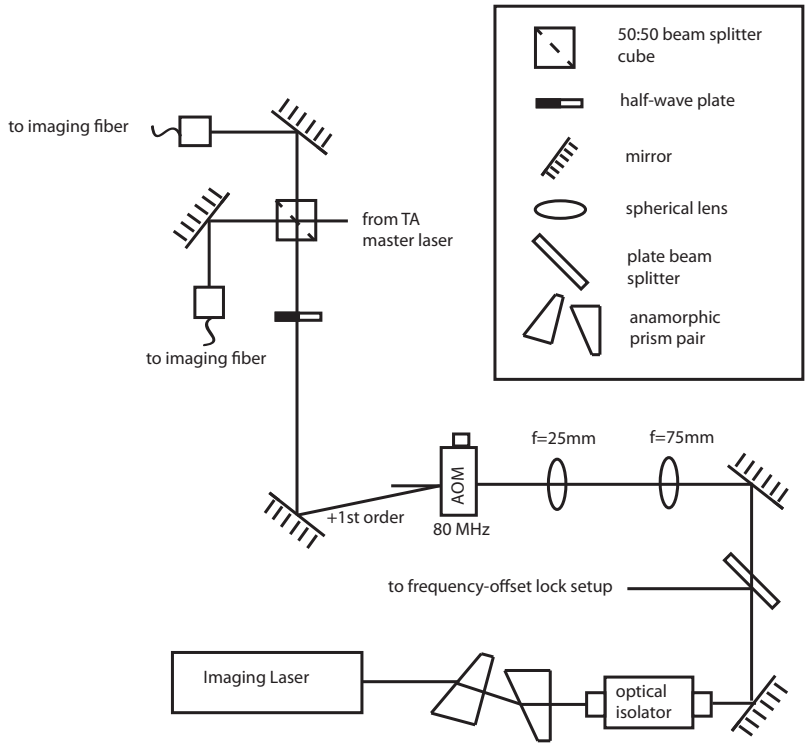

Figure 6.24: Imaging laser optical setup. *Figure courtesy of Kirsten Viering.*

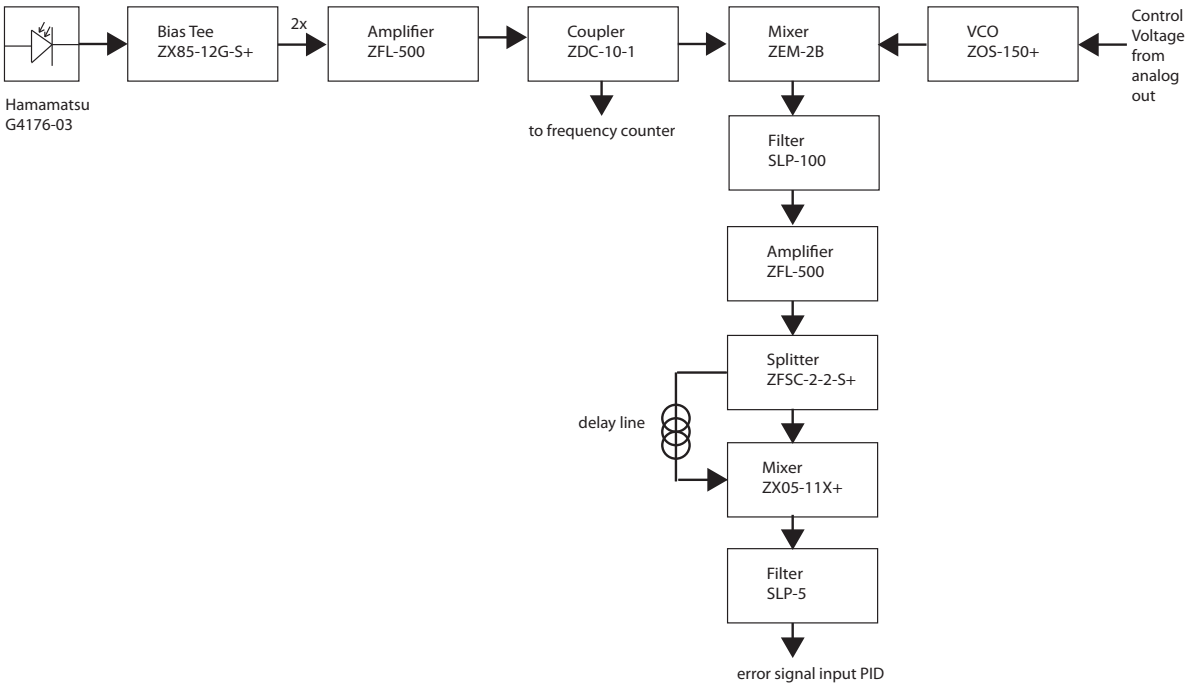

Figure 6.25: Imaging laser beatlock electronics setup. *Figure courtesy of Kirsten Viering.*

6.4 Off Resonance Lasers Systems

The off resonance laser systems are used to create optical dipole traps. We have one 130 Watt CO_2 laser used to optically trap and evaporate lithium-6 to degeneracy. A small power Nd:YAG laser is used to trap the lowest energy state atoms of the CO_2 optical trap to then do the culling process.

6.4.1 Carbon Dioxide Laser

An ideal optical dipole trap to perform optical evaporation should be very deep and have a negligible photon scattering rate. A high power far red-detuned laser would offer both a low scattering rate and a deep optical potential. At a wavelength of 10.6 μm and a power of 130 Watts, the Coherent GEMSelect CO_2 laser yields a scattering rate of a few photons per hour. In addition, the intensity noise of the CO_2 laser is below our requirements.

Although the power of the laser can be pulsed to reduce its average power, it is operated in continous mode and its power is controlled by a single crystal germanium acousto-optical modulator (IntraAction, AGM-4010BJ1) with a center frequency of 40 MHz. Despite the relatively high transmission of germanium at 10.6 μm, the crystal absorbs enough power that it requires water cooling with a flow rate of 1 L/min. The diffraction efficiency of the first order of the AOM is about 85%. This leaves enough power in the zeroth order to require a water cooled beam dump.

Figure 6.26 shows a diagram of the CO_2 laser optical setup. Copper mirrors are used to reflect the CO_2 laser. Because the germanium crystal is water cooled only at the top and the bottom, a vertical temperature gradient develops across the crystal which leads to a cylindrical lensing effect. Thus, a cylindrical telescope is placed after the germanium AOM to correct for this effect. All CO_2 lenses are made of Zinc Selenide.

After the cylindrical telescope, a 1:4 spherical telescope increases the beam diameter before the final $f = 5$ in focal length Zinc Selenide lens that focuses the beam into the spherical octagon. The power right before the ZnSe lens at the octagon is 86 Watts. The trap formed by the CO_2 laser is a single pass optical dipole trap. After going

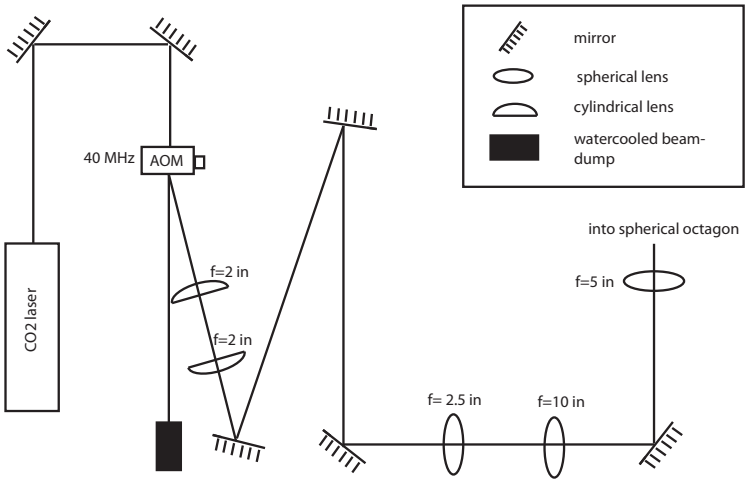

Figure 6.26: CO_2 laser optical setup. *Figure courtesy of Kirsten Viering.*

through the spherical octagon, the beam is dumped in a water cooled beam dump.

6.4.2 CO_2 Laser Interlock and Cooling Systems

The CO_2 laser, the germanium AOM, the AOM driver, and the beam dumps are all water-cooled. The CO_2 laser is cooled by a chiller (Lytron, RC022J03BF2C031) provided by Coherent. An additional chiller (Neslab, M33), provides cooling for the beam dumps, the AOM, and the AOM driver. A second home-built distribution line identical to the one described in section 6.2.4 is used to distribute the water lines.

An interlock box monitors will shut off the laser if the water flow rate is insufficient or the temperature rises above 22 °C. Additionally, an emergency shut-off switch is located at the entry of the lab that will stop emission at any time.

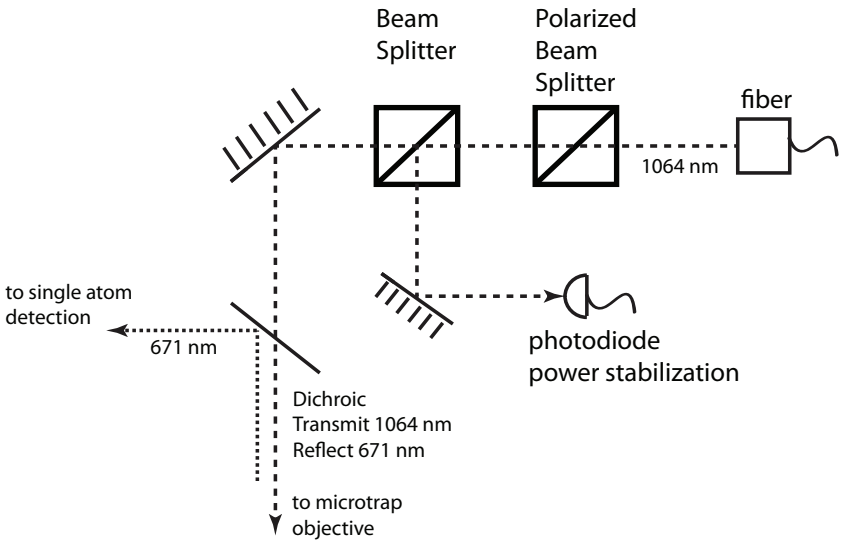

Figure 6.27: Microtrap optical setup. Coming out of the fiber, the beam has a waist of 8 mm. It is sent through a polarized beam splitter cube were its polarization is cleaned. Next, it is split into two beams by a non-polarizing beam splitter cube. One part is sent to a photodiode for power stabilization, while the other is sent to the microtrap objective which focuses it inside the spherical octagon (science chamber). A dichroic mirror placed before the microtrap objective enables us to use the same optical axis for single atom detection.

6.5 The Microtrap Optical Setup

The power for the microtrap comes from a Mephisto (Innolight GmbH) laser. The power of the beam coming out of the Mephisto is modulated with an AOM and then coupled to a fiber that is sent to the experiment table. Figure 6.27 shows the optical setup of the microtrap beam. Coming out of the fiber, the beam has a waist of 8 mm. A polarizing beam splitter cube cleans the beam's polarization. The beam is then split into two beams by a non-polarizing beam splitter. One of the resulting beams is sent to a photodiode for amplitude stabilization purposes, while the other is used as the microtrap beam. The microtrap beam is reflected down by a mirror and then passes through a dichroic mirror that transmits 1064 nm and reflects 671 nm. After the dichroic mirror, the beam is focused by the microtrap objective.

6.5.1 The Microtrap Objective

The top reentrant viewport of the spherical octagon is the most crowded and heavily used viewport of all. It is used by the vertical MOT beam, the Nd:YAG microtrap beam, the small MOT beam, and to collect photons for single atom detection. The microtrap objective must therefore allow the MOT beam return collimated, focus the Nd:YAG laser at a distance of 14.3 mm and with the smallest spot size possible, and allow the small MOT beam to propagate at an angle without interfering with it. It must also have a large numerical aperture to collect as many photons as possible, and it must be easy to construct and align.

The objective (figure 6.28)was designed using Zemax optical design software and is made of commercially available parts: an aspheric lens (Thorlabs, AL4532-B), and a meniscus lens (CVI MellesGriot, MENP-50.0-4.8-300.0-C-670-1064). Aspheric lenses are designed to minimize aberrations. However, the reentrant viewport window introduces aberrations that must be corrected with the meniscus. The spacing between the two lenses is 2 mm, and to focus at the location of the atoms the objective needs to be mounted 2.8 mm above the window of the reentrant viewport. The diffraction limited spot size of this objective for an incoming YAG beam with a waist of 8 mm is expected to be 1.7 μm.

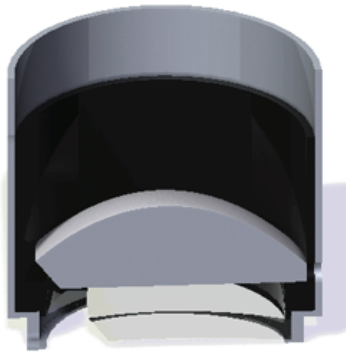

Figure 6.28: The microtrap objective. The microtrap objetive is made of two commercially available parts: an aspheric lens (Thorlabs, AL4532-B), and a meniscus lens (CVI MellesGriot, MENP-50.0-4.8-300.0-C-670-1064).

6.6 Control and Data Acquisition System

6.6.1 Control

The experimental sequence is controlled by a program named *Control*. Control was developed by Florian Schreck and its latest version is written in Microsoft Visual C++ 2005 and must be run in 32-bit Windows XP [40]. Control's graphical user interface allows the user to enter experimental parameters, create and modify experimental sequences, and execute them. The graphical elements of the program and the sequences themselves can only be modified in the source code. Therefore, the experimental sequences are programmed sequentially in a C++ environment. This has two advantages: first, time ordering becomes clear with sequential programming; and second, it allows the user to use all the power, might, and resources of Visual C++. A typical sequence looks like this,

```
void CSequence::MainSequence(){
 StartSequence();
 OpenOvenShutter();
 OpenAllShutters();
 SetMOTAttenuation(0);
 SetRepumpAttenuation(0);
 SetZSAttenuation(0);
 SetZeemanCurrent(5.9);
 SetMOTCurrent(20);
 Wait(7000);
 ..
 StopSequence();
}
```

In its current version, Control runs at 2 MHz (0.5 μs time resolution) and provides classes to use the following National Instruments cards

- **NI-PCI 6533**. This is a fast 32 digital output card. Control can control each output of this card individually to give 32 digital outputs, or it can use it to create the Multi-IO system that will be described later.

- **NI-PCI 6733**. This card provides 8 analog outputs, 8 configurable digital inputs/outputs, and one 24-bit counter.

- **NI-PCI 6024e**. This card provides 16 single-ended analog inputs with a 12-bit resolution at a sampling rate of 200 kS/s, two 12-bit analog outputs, 8 digital I/O lines, and two 24-bit counters.

- **NI-PCI GPIB**. This card provides a GPIB port, and can support up to 14 devices.

In addition to these NI card classes, Control provides a variety of classes that give access to the serial port, parallel port, and windows network sockets (TCP/IP). Using these classes, one can easily build classes to support any instrument or computer that connects to the main computer via parallel, serial, GPIB, or the Ethernet port.

6.6.2 The MULTI-IO System

A typical cold atoms experiment needs a few tens of digital and analog outputs, and some tunable radio frequency sources. This requires buying several computer cards and can be expensive. Fortunately, Control can use a single NI-PCI 6533 card to create a much larger number of analog and digital outputs and to control Direct Digital Synthesizers. The MULTI-IO system is a software communications architecture that uses a 25-bit parallel bus distribution system that connects to digital output cards, analog output cards, and Direct Digital Synthesizers. The MULTI-IO system currently supports,

- **Analog Output cards**. Each Analog output card provides eight 16-bit Digital to Analog converters and driver electronics to drive 1/4 of Ampere per channel from -10 V to 10 V.

- **Digital Output cards**. Each Digital output card provides 16 buffered digital outputs that can drive 50 Ohm loads.
- **Direct Digital Synthesizers (DDS)**. Each DDS can produce frequencies up to 135 MHz. The DDSs require a master clock running at 300 MHz.

More detailed information and instructions on how to build the MULTI-IO system hardware and devices can be found in [40].

6.6.3 Vision and Apogee Server

Our main data acquisition program, Vision, was written by Florian Schreck in Borland C++ 5.02; its source code and manual can be found in [40]. Vision manages the cameras that we use in the experiment and analyses and stores the pictures. Athough Vision supports several cameras, it doesn't support the cameras that we use in the experiment: two Apogee AltaU47 cameras, and one Allied Vision Technologies Stingray F033B/C. To solve this problem, a third program called Apogee Server was written in Visual C++ (by Florian Schreck), for which drivers for all these cameras exist. Vision and Apogee Server communicate via TCP/IP through which Vision can configure the cameras and retrieve the pictures. If a new camera needs to be added, one simply needs to obtain the Visual C++ drivers and modify the existing classes in Apogee Server and Vision. Vision also communicates with Control via TCP/IP, from which it receives all the experimental parameters of each run and all the necessary camera settings.

By analyzing fluorescent and absorption pictures, Vision can calculate optical densities and cloud sizes, from which it can calculate lifetimes and temperatures.

6.6.4 Labview Server

To measure the atom number at the end of the sequence, we turn on the MOT beams and focus the fluorescence onto a single photon counting module (model Perkin Elmer SPCM-AQR-14). The signal of this module is fed to the 24-bit counter of a National Instruments card. Since the NI-PCI 6733 was never able to work at 2 MHz with the newer version of Control, a Labview program that could communicate with

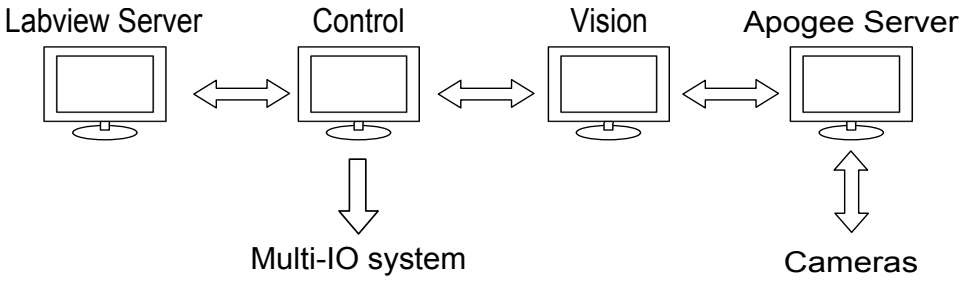

Figure 6.29: Experiment control and data acquisition system. Double arrows mean bidirectional communication, a single arrow means output only.

Control via TCP/IP had to be written. The *Labview* class in Control communicates with *Labview Server* through the LAN. At the beginning of the sequence, Control arms the counter through Labview Server, and at the end of the sequence, Control sends all the experimental parameters to Labview Server. Labview Server then saves both the parameters and the results of the measurements in the same file.

6.6.5 Computer Communications

We use four computers in the experiment, each of them running an instance of Control, Vision, Apogee Server, and Labview Server. Their interconnectivity can be seen in fig. 6.29.

1. Control sends Labview Server all the parameters to arm the counter.
2. Labview Server arms the counter.
3. Control sends Vision parameters to arm the cameras.
4. Vision sends Apogee Server all the camera parameters to arm the cameras.
5. Apogee Server arms each camera.
6. Control runs the sequence and triggers the cameras and the counter.
7. Apogee Server retrieves the pictures as soon as they become available and sends them back to Vision.

8. Control sends Vision extra parameters needed to analyze the pictures.
9. Vision analyzes the pictures and saves the results in a file.
10. Labview Server saves the result of the measurement in a file.
11. Control sends Vision and Labview Server the rest of the experimental parameters.
12. Labview Server and Vision each save the experimental parameters in a file.

Chapter 7

Experimental Sequence: Towards high-fidelity Fock states

The ^{6}Li experiment has not yet produced high-fidelity Fock states. However, much progress has been done towards this goal. In particular, evaporative cooling was optimized and degeneracy was achieved; the microtrap objective was characterized, installed, and aligned; the microtrap laser optics were installed; atoms were loaded into the microtrap; and the single atom detection optics were installed and are currently being optimized.

This chapter will describe the experimental sequence used to obtain a single pair of atoms with ultra-high fidelity and summarize the progress done towards the production of ultra-high fidelity atomic Fock states.

7.1 Experimental Sequence

Starting from a cloud of cold ^{6}Li atoms in a MOT, the atoms are cooled further and compressed into a CO_2 optical dipole trap. We then perform optical evaporation to cool the atoms to degeneracy. A weak but tightly focused 1064 nm optical dipole trap (the microtrap) is superimposed on top of the CO_2 optical dipole trap during evaporation to increase the Fermi temperature, thus achieving an effective degeneracy factor $T/T_F \leq 0.1$. The probability of ground state occupancy is now $P_{gnd} > 0.9999$. The CO_2 optical dipole trap is turned off and a magnetic field gradient is turned on. The magnetic field gradient tilts the optical potential produced by the microtrap, transforming the bound states of the microtrap into quasi-bound states, each with a lifetime τ_i. The difference in the lifetimes of the ground and first excited state can be of several orders of magnitude. Therefore, by waiting a suitable amount of time, one can generate a single pair of atoms

in the ground state of the trap with a probability exceeding 99.9%. The single pair can then be transferred to a magneto optical trap for single atom detection. The exact sequence to obtain a single pair of atoms in the ground state of an optical dipole trap is the following.

1. Load atoms into the MOT.
2. Load the atoms into the CO_2 optical dipole trap by compressing the MOT.
3. Turn on the microtrap on top of the CO_2 optical dipole trap.
4. Perform evaporative cooling to obtain a Fermi degenerate gas with an effective $T/T_F \leq 0.1$
5. Turn off the CO_2 optical dipole trap.
6. Culling process: reduce the power of the microtap and introduce a magnetic field gradient.
7. Wait for a certain holding time.
8. Adiabatically turn off the magnetic field gradient and increase the power of the microtrap. Turn on MOT for single atom detection.

For a microtrap power of 14.57 μW, a magnetic field gradient of -2.5 G/cm, and a holding time of 67.5 ms, the probability of obtaining a single pair in the ground state can be as high as $P_{gnd} = 0.9962$. I will now describe each step of the experimental sequence in more detail.

7.2 Loading the MOT

The experimental sequence starts by loading atoms into the magneto optical trap. Operating the oven at 350 °C and when optimally aligned, the MOT can be loaded at a rate of around 10^8 atoms per second. Lower loading rates of 10^7 are typically not a

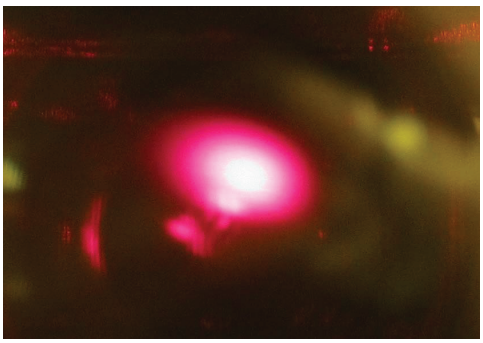

Figure 7.1: Atoms in the Magneto Optical Trap (MOT). A cloud of $N \approx 10^8$ cold atoms of ^{6}Li trapped in the magneto optical trap at $T \approx 3$ mK. The diameter of the cloud is between 3 and 4 mm. The atoms are the oval shaped cloud and are fluorescing at 671 nm. The rest of the red light is just reflections. It is a tradition (a very confusing one) to call *the MOT* to the atoms trapped in the MOT.

problem since what really matters is how many atoms are loaded into the CO_2 optical dipole trap. Figure 7.1 shows a picture of a typical MOT with around 10^8 atoms.

The loading rate of the MOT is very sensitive to beam alignment and depends on the oven temperature as well. Higher oven temperatures will yield higher loading rates at the expense of faster depletion of the lithium-6 oven. The atom number depends on the beam alignment, power, magnetic field gradient, and vacuum pressure. In our system, the size of the MOT saturates at around 1×10^9 atoms. The main reason for this limitation is two-body collisions; at high densities, inelastic collisions between lithium atoms lead to heating of the MOT. The beam size and the magnetic field gradient also limit the size of the MOT.

7.3 Compressed MOT and the CO_2 Optical Dipole Trap

The next step in the sequence is to load the atoms in the MOT into the CO_2 optical dipole trap (ODT). The atoms in the MOT cannot be efficiently loaded into the CO_2 laser by just superimposing the CO_2 laser on top of the MOT. The MOT atoms are too hot ($T > 2$ mK) to be loaded into the CO_2 ODT, which has a depth of just 700 μK. Even if the atoms were cold enough, since the CO_2 ODT is a conservative trap, any atom that makes it into the trap has enough energy to make it out of the trap. To load

atoms into the CO_2 ODT, we compress and cool the MOT by ramping the detuning of the MOT beams from 38 MHz to 6 MHz while at the same time decreasing the power of the MOT beams from 10 mW (4 mW) to 40 μW (30 μW) of MOT (repump) to avoid heating. Bringing the MOT beams (both MOT and repump) closer to resonance decreases the Doppler temperature, but increases the scattering rate. Therefore, the power of the beams is decreased at the same time to avoid heating the sample. Figures 7.3 and 7.2 show the temperature and diameter respectively of the MOT as the detuning of the MOT and repump beams is decreased: the MOT reaches a temperature of around 250 μK with a size of $\sigma_Y \approx 475$ μm and $\sigma_X \approx 690$ μm.

In the experiment, the detuning was always changed linearly, but the power was changed according to a power law that was optimized automatically. Depending on the compression curve (power v.s. detuning), up to 3×10^6 atoms can be loaded into the CO_2 ODT. Now, there is one very important step that has to be done after compressing the MOT to successfully load atoms into the CO_2 ODT: optical pumping. Since lithium-6 atoms in the states $|F = 1/2\rangle$ and $|F = 3/2\rangle$ have a nonzero scattering length even at $B = 0$, we must pump all of them into the state $|F = 1/2\rangle$ so that they do not undergo s-wave scattering. A magnetic field can then be used to lift the degeneracy of the state and perform evaporation with the two lowest hyper-fine states $|F = 1/2, m_F = \pm1/2\rangle$. Optical pumping is usually done by turning off the repump component of the MOT beam 50 μs before the main MOT component is turned off.

The next step after compressing the MOT is to load it into the CO_2 ODT. The trap depth of the CO_2 ODT is around 700 μK, and the $1/e^2$ diameter is 100 μm. Therefore, the compressed MOT must be cooled well below 700 μK and compressed as much as possible to load the atoms into the CO_2 ODT. The trap can be loaded simply by compressing the MOT within 200 μm of the center of the CO_2 ODT.

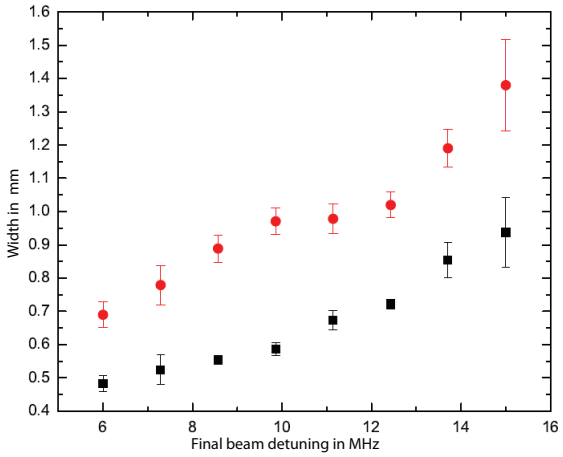

Figure 7.2: Width of the compressed MOT vs final beam detuning of the MOT beams. The figure shows the $1/e^2$ width of the compressed MOT as a function of the final beam detuning of the MOT beams. The red circles (black squares) represent σ_x (σ_y). *Figure courtesy of Kirsten Viering.*

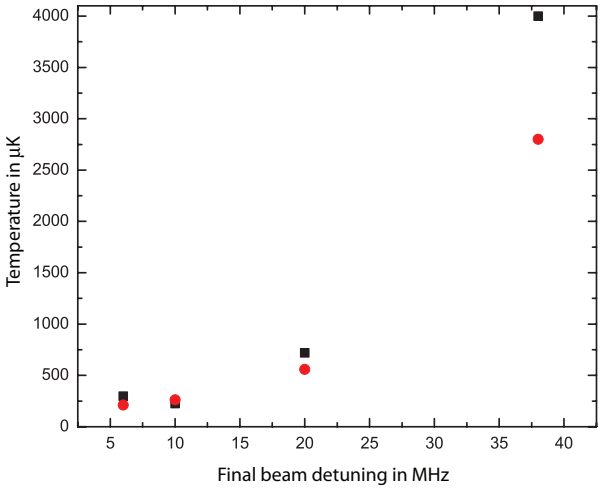

Figure 7.3: Temperature of the compressed MOT vs final detuning of the MOT beams. Black squares (red circles) represent T_x (T_y). *Figure courtesy of Kirsten Viering.*

7.4 Alignment of the CO_2 Laser Optical Dipole Trap: Invisible Atomic Beam Finder

Forced optical evaporation is a very useful technique to achieve degenerate quantum gases [27]. The large detuning of the CO_2 optical dipole trap provides an extremely low scattering rate: a 86 Watts beam of the CO_2 laser focused down to a spot with a waist of 50 μm, produces a trap with a depth of $\approx 800\mu$K with a scattering rate of 2.5 photons per hour, while a YAG (1064 nm wavelength) laser with similar spot size and trap depth has a scattering rate of 1.1 photons per second. Since the heating rate of the CO_2 is almost 2000 times smaller than the one of a YAG, we chose the CO_2 to perform optical evaporation. Our 86 Watt CO_2 laser beam is focused inside the vacuum chamber by an $f = 5$ in lens down to a spot of 50 μm, as can be seen in figure 6.26.

Although a CO_2 optical dipole trap has been used to trap [41] and cool [28] ^{6}Li to degeneracy, it is still difficult to align it and work with it. The main difficulty is *how to align an 86 W beam focused down to a 50 μm size spot inside a vacuum chamber with a precision of better than 200 μm without any commercially available device that can image it.* First, of course, one has to do a rough alignment and get the focus of the CO_2 reasonably close to the MOT. This can be done inserting a copropagating, near-resonant beam along the path that the CO_2 laser beam follows before entering the spherical octagon. This procedure, however, can only get the beam a couple of millimeters from the center of the MOT; a fine alignment procedure has to be used to do the final alignment.

One approach uses the AC-Stark shift (light shifts) induced by the optical dipole trap. In this approach, the near resonant beams are turned on and the fluorescence changes as the position of the optical dipole trap changes. Unfortunately, the AC-Stark shift that the CO_2 laser induced in the $^2S_{1/2}$ ground state and the $^2P_{3/2}$ excited state are nearly the same. For a 50 W laser beam focused to a waist of 50 μm the change in transition frequency at the peak intensity of the CO_2 laser is less than 10 MHz. The linewidth of this transition is around 6 MHz so the change in scattering rate is negligible. A different transition has been used [41] at 610 nm. The scattering rate of this transition

is very sensitive to the alignment of the CO_2 optical dipole trap. This method requires, however, an extra laser system, along with all its optics and electronics.

This is too expensive considering that we only need to align the CO_2 laser once. Therefore, we developed a cheap and robust method to align the CO_2 optical dipole trap [42]. The CO_2 laser beam is aligned using balanced lock-in detection from a fluorescent split-image. This technique requires a lock-in detector, two photodiodes, and a few optics.

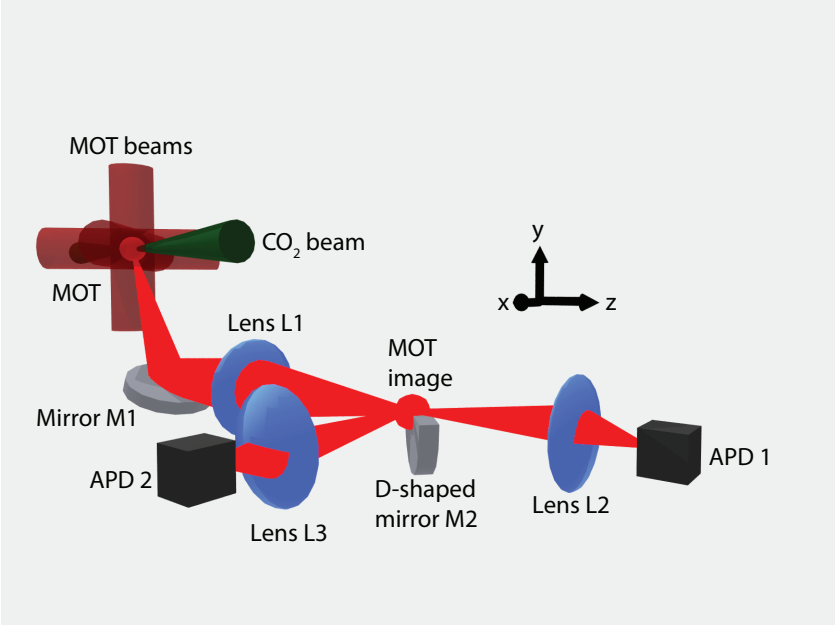

Figure 7.4: Optical setup for the CO_2 alignment procedure. Light from the MOT is collected by Lens L1, which forms a real image of the MOT at a D-shaped mirror M2 mounted on translation stage. The D-shaped mirror splits the image of the MOT in two parts, each of which is focused by a lens (Lens L2 and Lens L3) onto an avalanche photo diode (APD1 and APD2 respectively). With the MOT on and with the CO_2 laser off, the D-shaped mirror is moved to balance both signals. F*igure courtesy of Kirsten Viering.*

The optical setup of the beam alignment technique can be seen in figure 7.4. Light from the MOT is collected by Lens L1, which forms a real image of the MOT at a D-shaped mirror M2 mounted on translation stage. The D-shaped mirror splits the image of the MOT in two parts, each of which is focused by a lens (Lens L2 and Lens L3) onto an avalanche photo diode (APD1 and APD2 respectively). With the MOT ON

and with the CO_2 laser OFF, the D-shaped mirror is moved to balance both signals. In a perfectly static MOT, the two signals would balance exactly, but due to beam power fluctuations and complicated MOT dynamics, the signal cannot be completely balanced and exhibits a particular noise spectrum. The noise spectrum of the difference of the signals can be seen in figure 7.5. If we now turn on the CO_2 laser in the vicinity of the MOT, we would induce a slight increase in the atom density. However, the fluctuations in the fluorescence of the MOT would make it impossible to see any change in the local density. Fortunately, if we *pulse* the CO_2 laser at frequency much higher than the typical frequency of fluctuations, then we could do lock-in detection and be able to detect this small density increase.

The natural question is now, what is the optimum modulation frequency. Figure 7.5 suggests that we use any frequency above 2 kHz. We cannot use arbitrarily large pulsing frequencies because the atoms in the MOT cannot respond too fast. In our case, the best pulsing frequency was found to be 2.4 kHz.

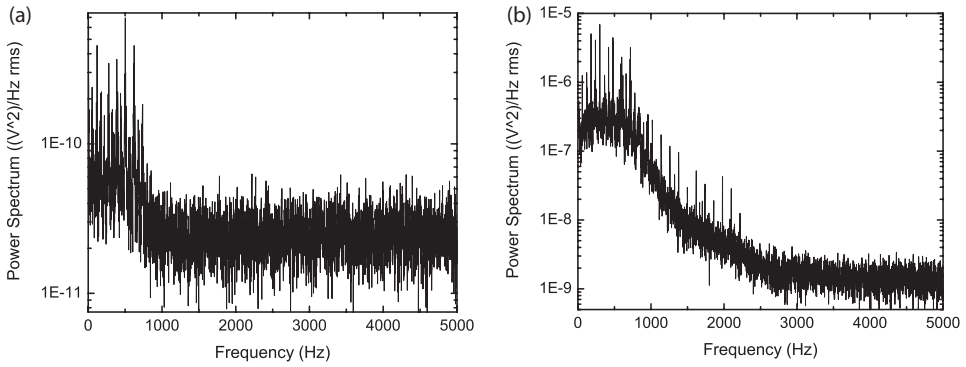

Figure 7.5: Power spectrum of the balanced fluorescence signal of the MOT. Left: noise with no MOT. The main sources of noise when there is no MOT are electronic and scattered light fluctuations. Right: noise spectrum when the MOT is present. From the noise spectrum it can be seen that the noise decreases after 2 kHz. We found that the best modulation frequency for our system was at 2.4 kHz. *Figure courtesy of Kirsten Viering.*

Figure 7.6 shows the detected signal as the CO_2 laser is moved across the MOT using the ZnSe lens mounted on a 3D translation state. Figure 7.6 (a) shows the relative orientation of the CO_2 laser beam relative to the MOT and the D-shaped mirror. The

CO_2 laser beam can be translated along the x, y, and z axes shown in the figure. Figure 7.6 (b) shows the recorded signal when the CO_2 laser is moved along the x axis (in and out of page) when positioned at $Y = -0.8$ mm and $Z = 2.5$ mm. Since the CO_2 beam stays in the same half of the MOT's image, the signal has the same sign across the scan.

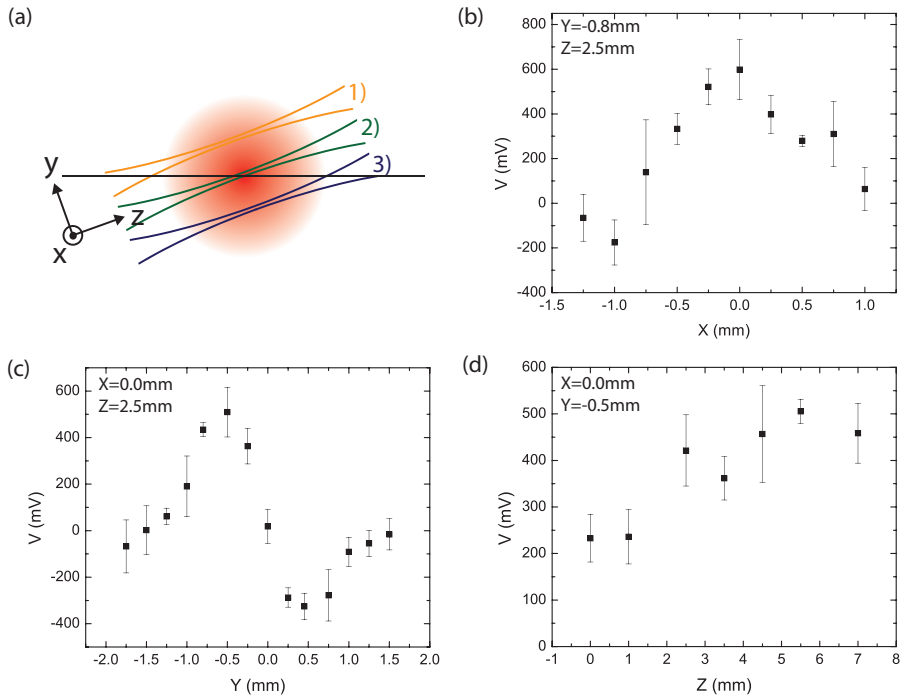

Figure 7.6: Signals recorded from the alignment procedure. (a) Relative orientation of the CO_2 laser beam relative to the MOT and the D-shaped mirror. The CO_2 laser beam can be translated along the x, y, and z axes shown in the figure. The relative angle arises because look at the MOT thru a viewport at an angle. (b) Recorded signal when the CO_2 laser is moved along the x axis (in and out of page) when positioned at $Y = -0.8$ mm and $Z = 2.5$ mm. Since the CO_2 beam stays in the same half of the MOT's image, the signal has the same sign across the scan. (c) Recorded signal when the CO_2 laser is moved along the y axis (positions 1 thru 3) with $X = 0$ mm and $Z = 2.5$ mm. The CO_2 laser beam moves across the two halves of the MOT's image, therefore a sign change is expected. Moreover, the signal vanishes when the CO_2 is exactly at the center of the MOT. (c) Recorded signal when the CO_2 laser is translated long the z direction. *Figure courtesy of Kirsten Viering.*

Figure 7.6 (c) shows the recorded signal when the CO_2 laser is moved along the y axis (positions 1 thru 3) with $X = 0$ mm and $Z = 2.5$ mm. This time the CO_2 laser beam moves across the two halves of the MOT's image, therefore a sign change is expected.

Moreover, the signal vanishes when the CO_2 is exactly at the center of the MOT. Finally, Figure 7.6 (c) show that the technique is not very sensitive to displacements in Z. There are two reasons for this: first, as the beam moves in the z direction, the size of the beam increases, affecting a larger portion of the MOT, but with a smaller intensity.

Nevertheless, the method is sensitive even if the CO_2 is a couple of millimeters away from the center of the MOT, which is the best one can do when aligning it with a copropagating near-resonant beam.

7.4.1 CO_2 Laser Trapping Frequencies and Waist Measurement

In principle, if one knows the power of an ideal optical dipole trap, one can calculate the trapping frequency for small oscillations. Since our trap is not ideal, the beam waists at the focus and the trapping frequencies of the trap were independently measured. The CO_2 laser beam waist was measured at low power using a photodiode sensitive to 10.6 μm (VIGO systems). A beam splitter is temporarily placed after the spherical telescope. The beam splitter reflects 99% of the beam into a beam dump, and the transmitted 1% is sent through a replica of the ZnSe lens used in the experiment and through a ZnSe window to simulate the spherical octagon ZnSe viewport. The beam waists were then measured and found to be 61 μm and 42 μm. One common way of measuring the trapping frequency of an optical dipole trap is to trap atoms and then modulate either the intensity of the trap or the position of the trap to parametrically heat the sample. Modulating the intensity has the disadvantage that the trapping frequency also depends on the intensity, so the modulation depth cannot be too large. On the other hand, modulating the position of the beam does not change the trapping frequency and can be done at much larger modulation depths. Figures 7.7 and 7.8 show the atom loss from the CO_2 optical dipole trap when the amplitude is modulated by 20% for a few seconds for low and high frequencies respectively. Since the heating mechanism is parametric heating, resonant atom losses occur at twice the expected trapping frequencies.

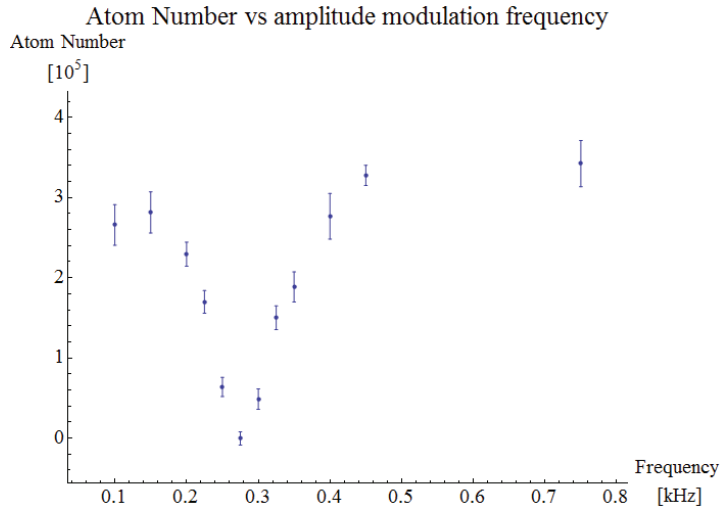

Figure 7.7: Atom loss due to amplitude modulation of the CO_2 optical dipole trap from 0 to 800 Hz. Since the atom loss mechanism is parametric heating, the resonant frequency is twice the trap frequency. The resonance occurs at ≈ 280 Hz, so the trap frequency is $\omega_z \approx 140$ Hz. The error bars indicate statistical uncertainty in the atom number.

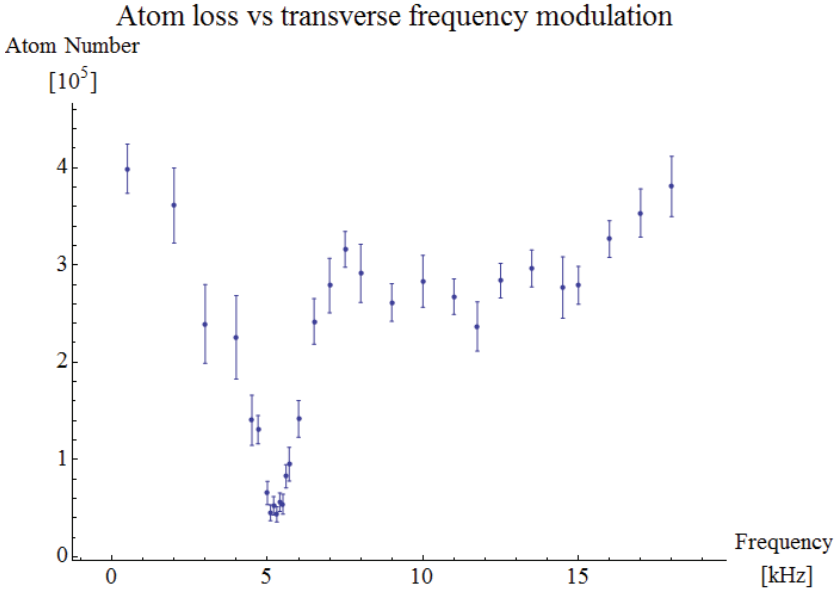

Figure 7.9: Atom loss due to transverse modulation of the vertical position of the CO_2 optical dipole trap from 0 to 18 kHz. The system behaves like a driven harmonic oscillator, and the maximum atom loss occurs exactly at the resonance ≈ 5.25 kHz. This is consistent with figure 7.8 and shows that the vertical position has the highest trapping frequency. The error bars indicate statistical uncertainty in the atom number.

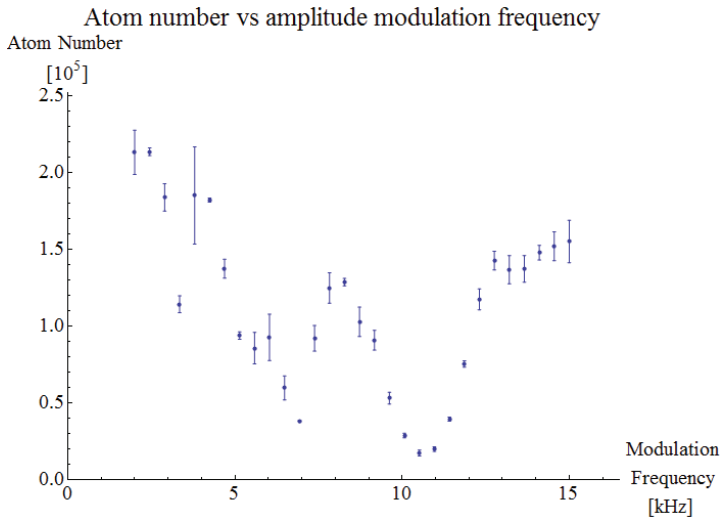

Figure 7.8: Atom loss due to amplitude modulation of the CO_2 optical dipole trap from 0 to 15 kHz. Since the atom loss mechanism is parametric heating, the resonant frequency is twice the trap frequency. Two resonances occur, one at $\approx$ 7 kHz, and the other at $\approx$ 10.5 kHz. Therefore, the trap frequencies are $\omega_x \approx 3.5$ kHz and $\omega_y \approx 5.25$ kHz. The error bars indicate statistical uncertainty in the atom number.

7.5 Evaporative Cooling: Achieving Degeneracy

Evaporative cooling allows us to achieve low enough temperatures ($T \approx 0.5\ \mu$K) and high enough atom number (N>10^5) so that the phase space density exceeds $\rho \geq 1$. Evaporation becomes more efficient with longer evaporation times, as the sample has more time to rethermalize. However, the finite lifetime of our cold atoms in the CO_2 ODT ($\tau \approx 27$ seconds) limits the evaporation time. Fortunately, we can increase the collision rate by increasing the scattering cross section using Feshbach resonances. The two lowest hyper-fine states of ^{6}Li present during evaporation, states $|1\rangle$ and $|2\rangle$ as defined in figure 2.3, have a broad feshbach resonance at 834 G that can be used to change the scattering lenght a from $a = 0$ to about $a = -300a_0$ at $\approx$ 330 Gauss to $a = \infty$ at 834 G. Increasing the scattering cross section enables us to perform efficient evaporation in shorter time, avoiding atom losses due to the finite lifetime of our CO_2 optical dipole trap.

A two-stage forced evaporation sequence (see figure 7.10) is employed to achieve degeneracy:

1. Initially, around 2.3×10^6 atoms in the CO_2 optical dipole trap have a temperature of around 115 μK.

2. Free evaporation 1: An homogeneous magnetic field is ramped from 0 G to 760 G. The atoms are allowed to freely evaporate for 300 ms at full trap depth until they reach a temperature of around 50 μK. Approximately 1.2×10^6 atoms remain.

3. Forced evaporation 1: With the magnetic field still at 760 G, the trap depth is reduced from 100% to 13% of the total trap depth. The curve used is the energy independent curve,
$$U(t)/U_0 = (1 + t/\tau)^\beta$$
with parameters: $\tau = 500$ ms, β=1.3.

4. Free evaporation 2: With a trap depth of 13% and still at 760 G, the atoms are allowed to freely evaporate again for 100 ms.

5. Forced evaporation 2: The magnetic field is ramped to 330 G and the trap depth is ramped from 13% to 0.35% of the total trap depth. The curve used is again the energy independent curve used in the first forced evaporation but with different curve parameters: $\tau = 600$ ms, β=1.4.

To calculate the degeneracy factor, we need to measure both the temperature and the Fermi temperature through the evaporation sequence. Recall that $k_B T_F = \hbar\bar{\omega}(6N)^{1/3}$, so we need to measure the atom number and the trapping frequencies to calculate the Fermi temperature at any given time during the evaporation sequence. Now, while measuring the atom number is a trivial task, measuring the trapping frequencies is tedious. I will make the reasonable assumption that $\omega \approx \omega_0\sqrt{U(t)/U}$, so that we can use the previously measured full trap depth trapping frequencies: $\omega_x = 2\pi \times 3.5$ kHz, $\omega_y = 2\pi \times 5.5$ kHz, and $\omega_z = 2\pi \times 140$ Hz. The atom number and temperature during evaporation are shown in figures 7.11 and figure 7.12 respectively.

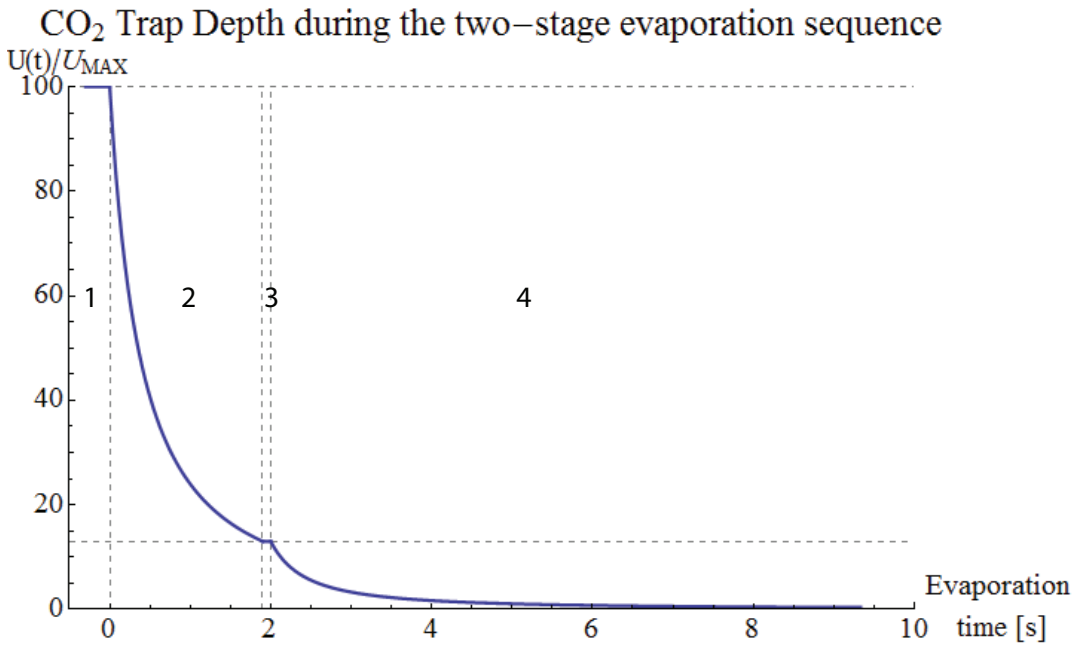

Figure 7.10: Evaporation Curve. The vertical dashed lines divide the evaporation curve in 4 parts. From left to right: 1) Free evaporation for 300 ms at 760 G and 100% of trap depth, 2) Forced evaporation at 760 G from 100% to 13% trap depth. Curve parameters: $\tau = 500$ ms, β=1.3. 3) Free evaporation for 100 ms at 760 G and 13% trap depth, and 4) Forced evaporation at 330 G from 13% to 0.35% trap depth. Curve parameters: $\tau = 600$ ms, β=1.4.

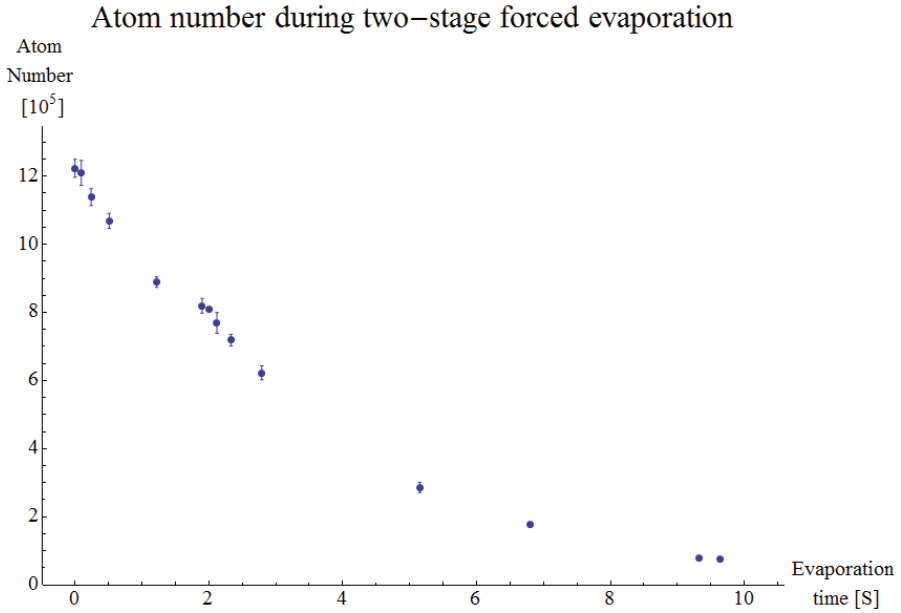

Figure 7.11: Atom number during the two-stage forced evaporation sequence. The error bars indicate statistical uncertainties. After 6 seconds, the error bars are smaller than the points.

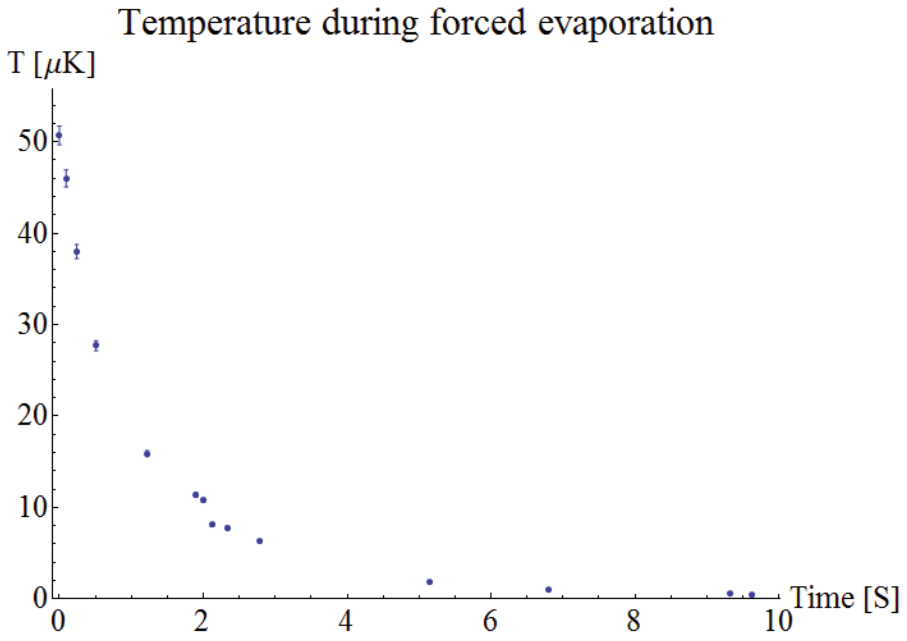

Figure 7.12: Temperature during forced evaporation. The first stage of forced evaporation starts when the atoms reach a temperature of around 50 μK. The second stage starts when they reach a temperature of around 10 μK. The final temperature is around (574 ± 140) nK

The Fermi temperature can now be calculated, as well as the degeneracy factor T/T_F. Figures 7.13 and 7.14 show the Fermi temperature and degeneracy factor respectively. The phase-space density can be calculated from $\rho = (T/T_F)^{-3}/6$. Figure 7.15 shows how the phase-space density increases during the two-stage evaporation. The lowest degeneracy factor in figure 7.14 is $T/T_F \approx 0.4$, with $T = 0.530$ μK and $T_F \approx 1.2$ μK. Adding the microtrap on top with a power of 500 μW and a waist of 1.46 μm, and assuming thermalization, will further increase the Fermi temperature to $T_F = 7.2$ μK, giving a final $T/T_F \approx 0.07$.

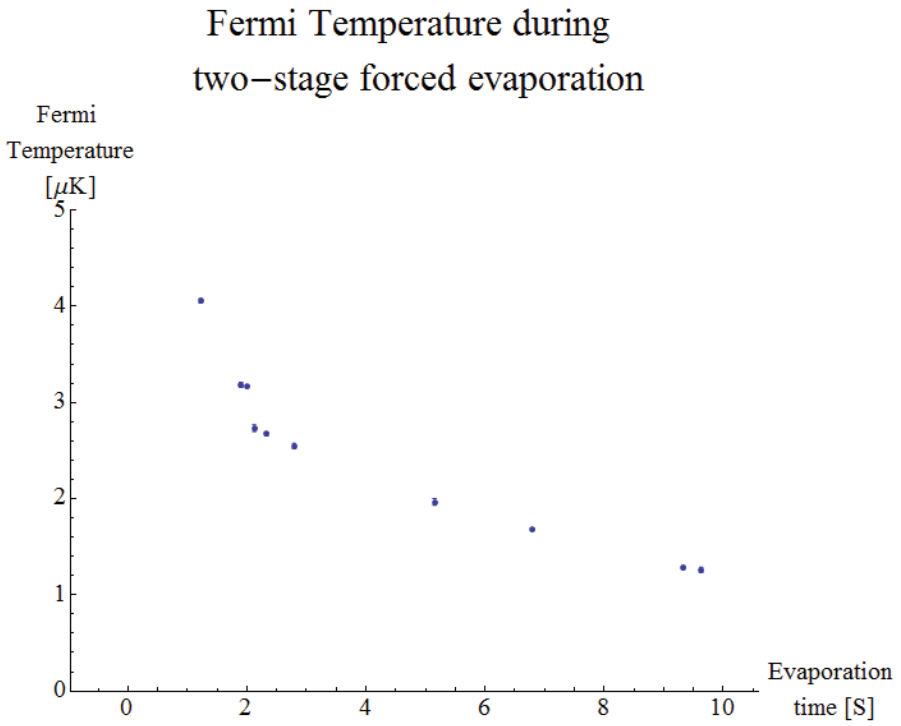

Figure 7.13: The Fermi temperature is shown through the evaporation sequence. The error bars are calculated using the statistical uncertainties of the atom number and assuming there are no statistical uncertainties in the trapping frequencies.

The next section describes the microtrap beam waist measurements and alignment

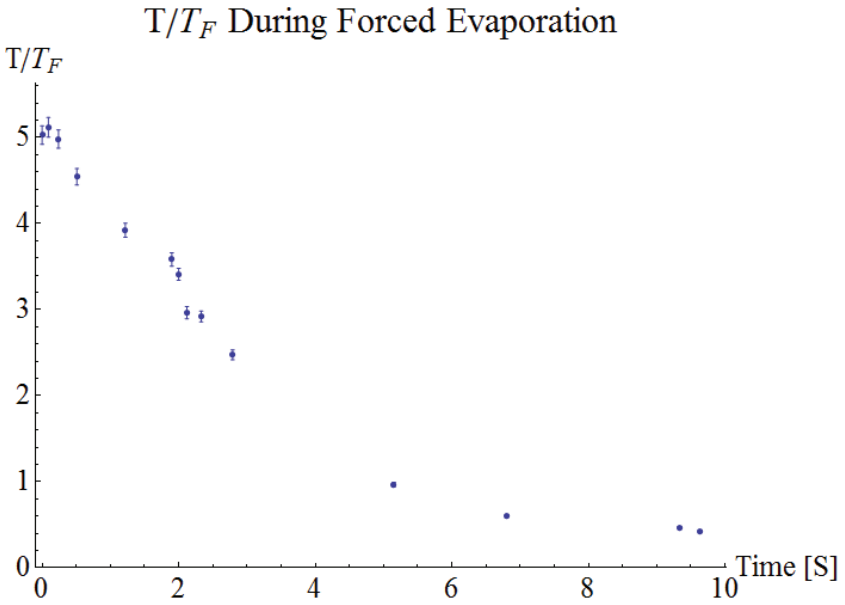

Figure 7.14: The degeneracy factor is shown through the evaporation sequence. The smallest degeneracy factor is around $T/T_F \approx 0.42$. The error bars are calculated using the errors from both the temperatures and the Fermi temperatures.

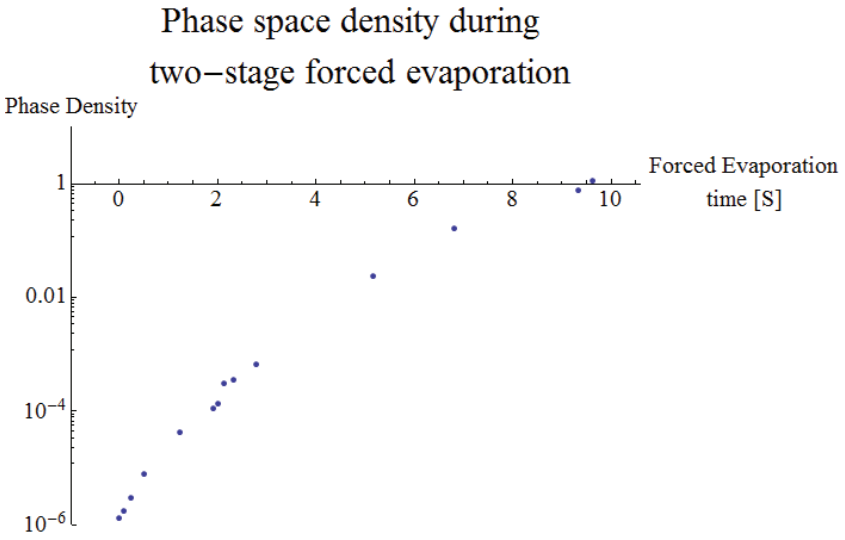

Figure 7.15: Phase space density during the two-stage forced evaporation. The error bars are smaller than the points. The largest error bar corresponds to the highest phase-space density value: 2.23 ± 0.06.

7.6 The Microtrap

The micotrap is a weak ($P \leq 1$ mW) but tightly focused ($w \approx 1.4$ μm) optical dipole trap formed by a 1064 nm wavelength Nd:YAG laser. Being so tightly focused, the microtrap can only hold around 1000 atomic states. It is in the microtrap where the final stage of the high-fidelity preparation of a single pair scheme takes place. In this section I present the microtrap beam waist properties and the alignment procedure.

7.6.1 The Microtrap Objective Beam Properties

To measure the microtrap beam waists, the objective was mounted outside the chamber and a window simulating the re-entrant viewport window was placed at the same distance as the experimental setup. The beam waists were then measured and the results can be seen in figures 7.16 and 7.17. The waists are $w_x = 1.36$ μm and $w_y = 1.57$ μm which give an effective $w \approx 1.46$ μm.

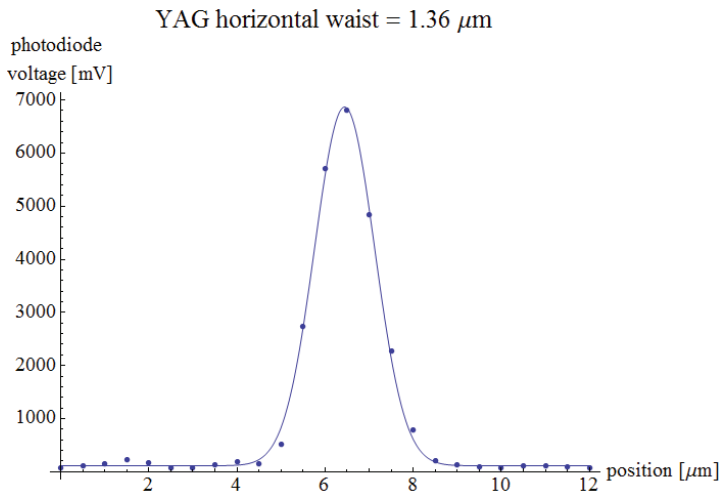

Figure 7.16: Horizontal waist of YAG. The horizontal waist of the YAG was measured to be 1.36 μm.

7.7 Alignment of the Microtrap Objective

The alignment of the microtrap was a challenging task that took us over a month to complete. One has to consider how stable is the position of the atomic cloud at every

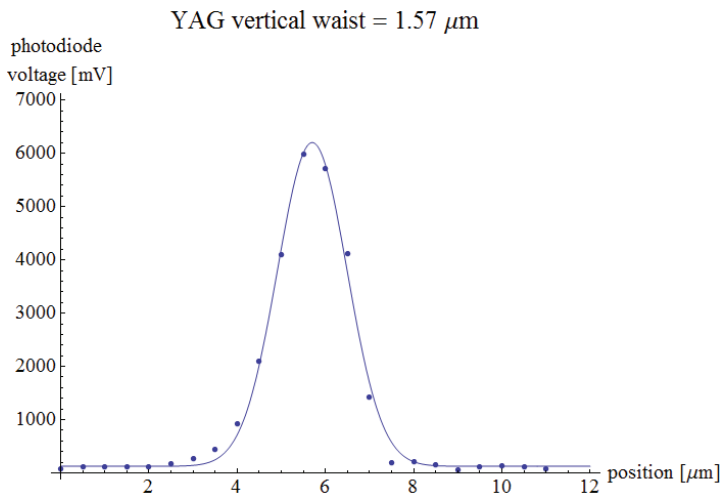

Figure 7.17: Vertical waist of YAG. The vertical waist of the YAG was measured to be 1.57 μm.

moment of the experimental sequence and how it changes on a daily basis due to laser power and temperature fluctuations. The relevant atomic cloud positions we need to consider are:

- **The MOT**. The alignment of the MOT is stable. If the beams are fairly retroreflected, the center of the MOT is insensitive to beam translations smaller than the waist of the beams. Since the MOT diameter is around 4 mm and its position changes by no more than 200 μm every day, its day to day position variation is negligible. However, care should be taken to retroreflect the beams as good as possible since the center of the compressed MOT and its compression efficiency depend strongly on beam alignment.

- **The Compressed MOT**. The position of the compressed MOT is unstable and changes every day. The position of the compressed MOT is very sensitive to the alignment and intensities of the MOT beams. Due to thermal effects, the coupling efficiencies of the MOT fibers change from day to day and this changes the position of the compressed MOT randomly by around 100 μm. Since the CO_2 dipole trap has a waist of 50 μm, we have to tweak the CO_2 dipole trap and the compressed MOT alignment almost every day.

- **CO_2 Dipole Trap**. The position of the CO_2 dipole trap is stable; once in position, we do not need change it.

- **YAG Microtrap**. The position of the YAG micotrap is stable; once in position, we do not need change it.

We decided to implement shim coils, since the only unstable position for the atomic cloud is the compressed MOT. Shim coils provide an offset magnetic field that changes the position of the zero of the quadrupole field, thus changing the position of the center of the compressed MOT. This allows us to align the CO_2 dipole trap and the microtrap regardless of where the MOT compresses to, since we can always use the shim coils to move around the compressed MOT.

Even though the shim coils makes our CO_2 dipole trap alignment independent of the day to day laser beam intensity variations, we still need to align both the CO_2 and the microtrap within 50 μm to see any trapping effect. With an initial uncertainty in the position of at least 64 cubic millimeters, a brute force three dimensional search with steps of 50 μm in x and y and 300 μm in z taking 1 minute each would take almost 120 days working 12 hours per day. Even if we decided to do it, there was no guarantee that we didn't have to repeat the alignment again. It was clear that a more efficient method had to be used. The alignment procedure we used was the following.

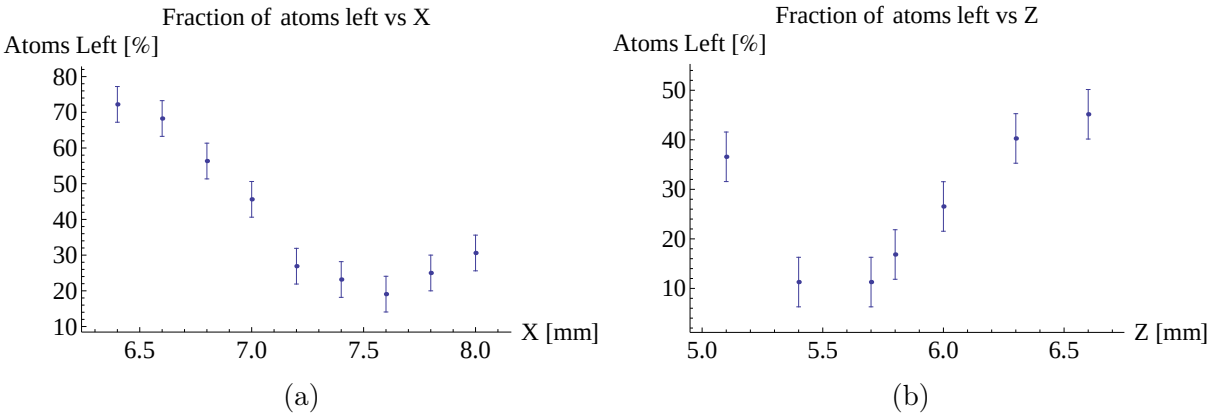

Figure 7.18: Fraction of atoms left after shinning a resonant beam for 20 μs. (a) Moving the CO_2 beam along the X direction (Zeeman Slower axis). (b) Moving the CO_2 beam along the Z direction (CO_2 beam propagation axis).

1. **Resonant beam alignment with fluorescent imaging.** We switched the YAG fiber to a fiber carrying a resonant beam, this way the resonant beam will follow the same optical path as the YAG beam. We then loaded atoms into the CO_2 dipole trap and shined the resonant beam for a few tens of microseconds (typically 20 μs) after which we measured the atom number using fluorescence imaging and compared it with the number when no resonant beam was present. This method allowed us to align the CO_2 beam within 1 mm in the radial directions of the resonant beam; see figure 7.18. While this method is not sensitive to translations along the resonant beam axis (up-down, objective axis), we were able to reduce the problem from a 3D search to a 1D search. We then used absorption imaging to align the axial direction of the resonant beam.

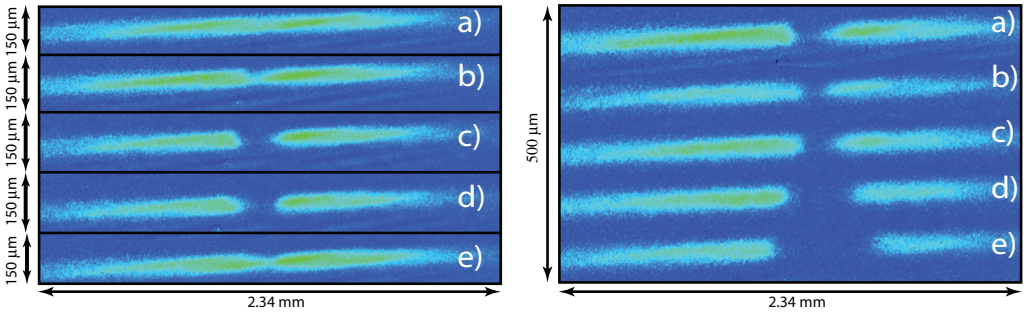

(a) X direction alignment (in and out of the page)

(b) Y direction alignment (up and down)

Figure 7.19: Absorption pictures of the atoms in the CO_2 dipole trap with the resonant beam on. (a) The CO_2 dipole trap is shown at five different positions along the Zeeman Slower axis: a) x = 7.38 mm, b) x = 7.35 mm, c) x = 7.30 mm, d) x = 7.25 mm, and e) x = 7.20 mm. (b) The CO_2 dipole trap is shown at five different vertical (up-down) positions: a) y = 1.90 mm, b) y = 2.00 mm, c) y = 2.10 mm, d) y= 2.20 mm, and e) y = 2.30 mm.

2. **Resonant beam alignment with absorption imaging.** With absorption imaging we were able to see the local effect the resonant beam had on the atoms trapped in the CO_2 dipole trap. This method allowed us to clearly see the converging and diverging nature of the resonant beam, thus giving us a final uncertainty in the position of less than 50 μm in the radial direction and less than 150 μm in the axial direction. Figures 7.19 and 7.20 show absorption pictures of the atoms trapped in

the CO_2 dipole trap. The pictures show the Y-Z plane. Figure 7.19(a) show the CO_2 beam at five different x positions; each of them had to be sliced

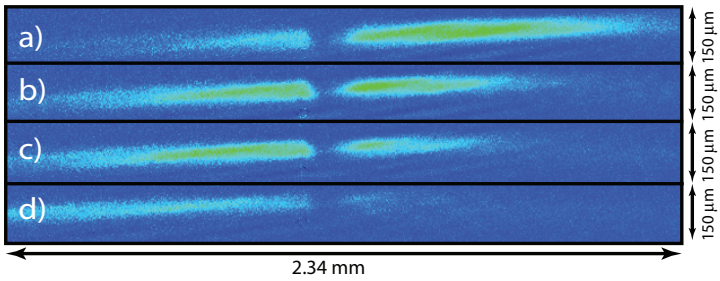

Figure 7.20: Absorption pictures of the atoms in the CO_2 dipole trap with the resonant beam. The CO_2 dipole trap is shown at four different positions along the CO_2 beam propagation: a) z = 6.00 mm, b) z = 5.60 mm, c) z = 5.45 mm, and d) z = 5.00 mm.

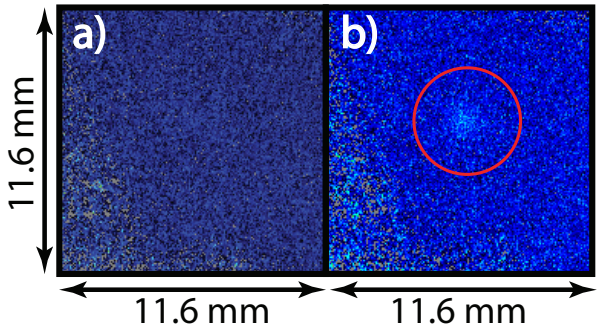

Figure 7.21: YAG beam alignment with fluorescence imaging. Around 1000 atoms are loaded into the YAG microtrap. (a) Fluorescence picture with no loading (microtrap off). (b) Fluorescence picture with loading (microtrap on).

3. **YAG beam alignment with fluorescent imaging and interactions.** We switched back to the YAG fiber and scanned the axial direction since the previous alignment was for a resonant beam at 671 nm that focuses farther away from the lens than the YAG beam. Having previously measured the waist location for 671 nm and 1064 nm, we knew that the two foci were 400 μm apart. At the beginning, we did not turn on the interactions and we could not load any atoms into the YAG. We then realized that the atoms where not thermalizing in the YAG dipole trap and were as likely to enter it as to leave it. We successfully loaded around 1000 atoms (see figure 7.21) after turning on the interactions at 300 gauss for a

couple of seconds. This method allowed us to align the YAG beam within 50 μm (300μm) of the radial (axial) direction of the CO_2 dipole trap.

4. **YAG beam alignment with absorption imaging.** Finally, we used absorption imaging to see the local effect of the YAG microtrap on the CO_2 dipole trap. A peculiar change in the atomic density could be seen in the absorption pictures. The disturbance (see figure 7.22)was about 100 μm along the axial direction of the CO_2 dipole trap. This method allowed us to axially (radially) center the YAG beam along (across) the CO_2 dipole trap within 100 μm (25 μm) of its center.

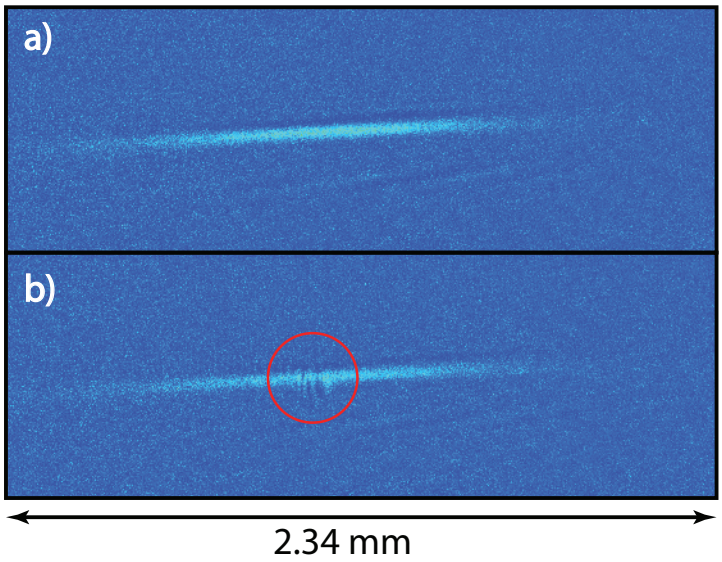

Figure 7.22: YAG beam alignment with absorption imaging. An absorption image of the atoms in the CO_2 ODT was taken (a) with the YAG off, and (b) with the YAG on. A peculiar feature, the "disturbance", can be seen circled in red.

Further optimization will be done using the single atom detection setup.

7.8 Power Stabilization of the Microtrap

Intensity noise in optical dipole traps can cause atom loss due to heating [43]. This would compromise the preparation of a single pair and would lower the fidelity.

Therefore, we stabilized the laser intensity using a PID controller. Figure 7.23 shows the optical setup of the PID controller used to stabilize the power of the microtrap.

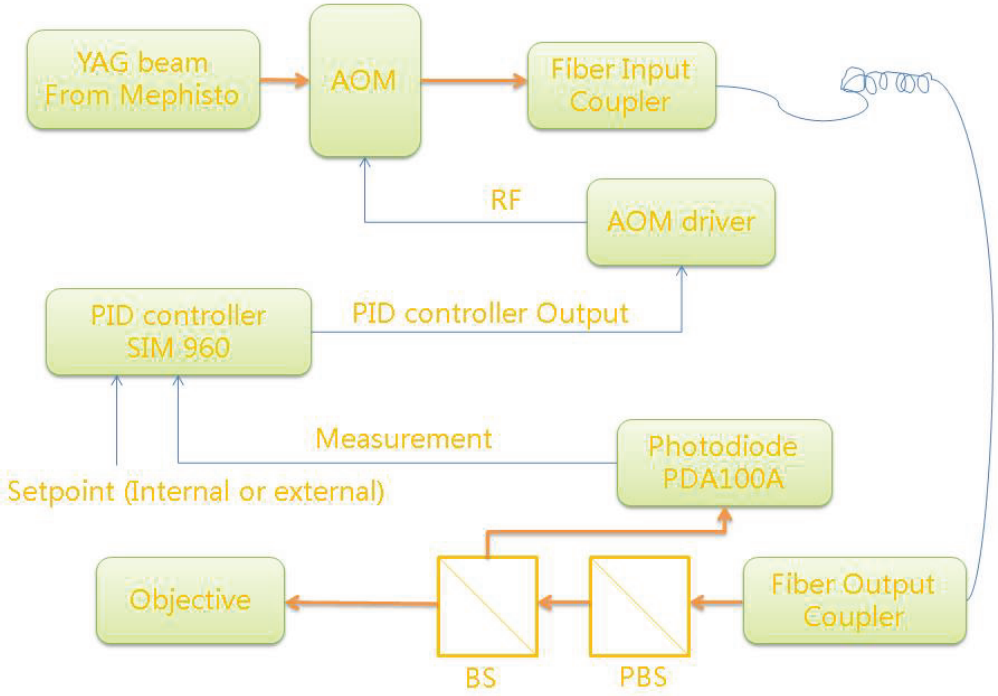

Figure 7.23: Optical setup of the intensity stabilization for the microtrap. The output of the Mephisto laser is sent through and acousto-optic modulator (AOM). The output is coupled to a fiber and sent to the experiment table. Part of the output of the fiber is sent to a photodetector. The output signal of the photodetector is sent to the PID controller module. The output of the PID controller is sent to the AOM driver that modulates the AOM. *Figure courtesy of Jianyong Mo*

The heating rate as a function of the power spectrum of noise is given by [43],

$$\Gamma_\epsilon \equiv \frac{1}{T_I(sec)} = \pi^2 \nu_{tr}^2 S_\epsilon(2\nu_{tr}). \tag{7.1}$$

Here ν_{tr} is the trap oscillation frequency in Hertz, and T_I is the energy e-folding time in seconds. The solid line of figure 7.24 shows the maximum noise for an e-folding time of $T_I = 100$ s. As can be seen in the figure, the noise is already well below the $T_I = 100$ e-folding time limit.

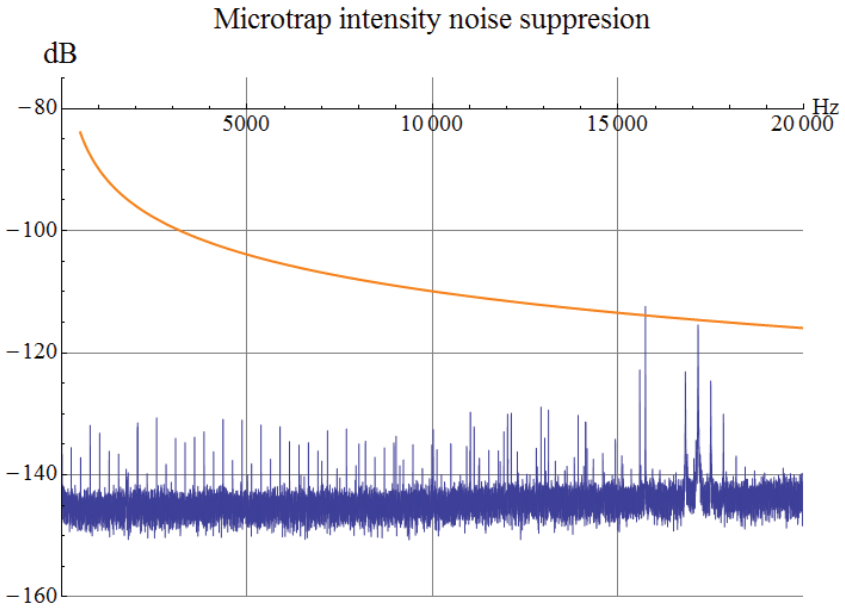

Figure 7.24: Microtrap intensity noise suprresion. The solid orange curve is the maximum intensity noise density that our microtrap can have for an e-folding time of 100 s. The intensity noise power spectra is shown in blue. *Figure courtesy of Jianyong Mo*

7.9 Single Atom Detection

Once we prepare a single pair of atoms in the ground state of the microtrap, we need to detect them with high fidelity. The single atom detection optical setup is shown in figure 7.25. A similar setup has been used before [44] to detect single atoms in a MOT. A pair of lenses (f1 and f2) focuses the image of the MOT on a pinhole that acts like a spatial filter, blocking all the light that doesn't come from the neighborhood of the MOT. The light exiting the pinhole goes through a telescope (lens f3 and f4) that has a bandpass filter that blocks all light except 671 nm. Lens f4 focuses the beam onto the avalanche photodetector (SPCM-AQR-14) operating in photon counting mode.

The dichroic mirror shown in the figure 7.25 is the same one placed along the microtrap objective axis (see figure 7.26). The vertical axis (figure 7.26) is used for three purposes: 1) as a MOT beam axis, 2) as the microtrap beam axis, and 3) as the single atom detection axis. To work as a MOT axis, a quarter wave plate, a lens, and a mirror were mounted on a translation stage that moves them in and out of the axis at different stages of the experiment. The lens is necessary because the beam is diverging

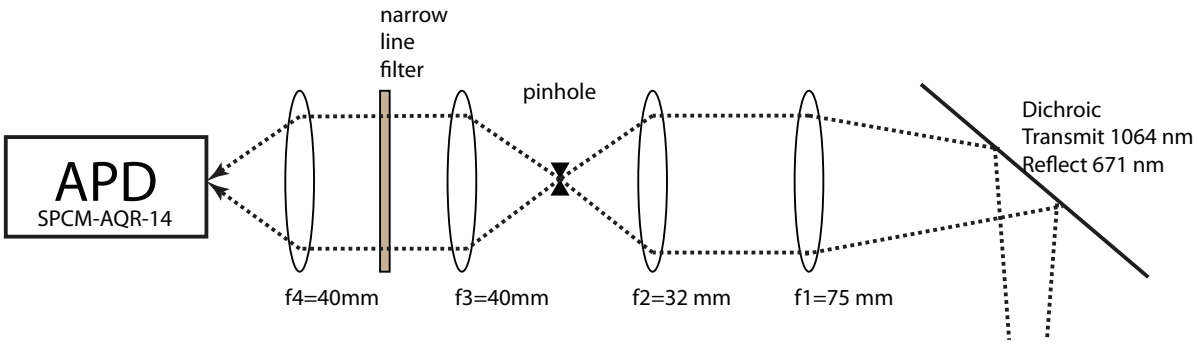

Figure 7.25: Single atom detection setup. Lens f1 collimates the light coming from the MOT. Lens f2 focuses it on the pinhole, which acts like a spatial filter. Lens f3 collimatse the beam before the narrow line filter, which absorbs all light except 67 1nm. Lens f4 focuses the beam onto the avalanche photodetector.

after agoing through the objective. When the mirror and the wave plate are on the axis, the axis works as a MOT axis. When the mirror and wave plate are out of the way, the axis can be used as the microtrap axis and the single atom detection axis at the same time thanks to the dichroic mirror. Notice, however, that to perform single atoms detection the MOT beams need to be on. Since the mirror and wave plate are out of the way, we cannot longer use the vertical MOT beam. Instead, we made a cut through the lenses through which a small MOT beam passes and is retroreflected by a small mirror and quarter wave plate. We call this small beam the "small MOT beam" and the MOT obtained with this beam "the small MOT". Single atom detection is done with the Small MOT. A schematic of the complete optics of the vertical axis can be seen in figure 7.26

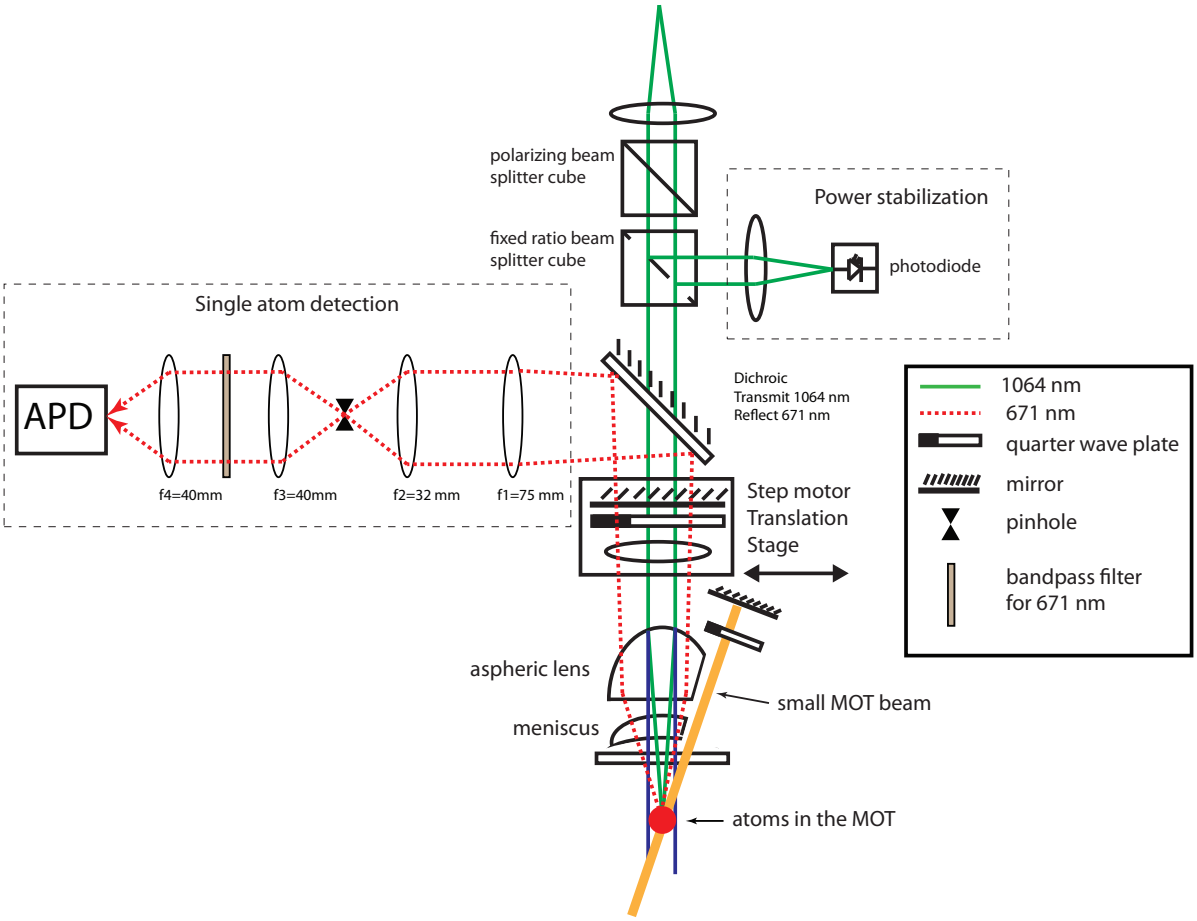

Figure 7.26: Full vertical axis optical setup. A mirror, a lens, and a quarter waveplate are mounted on a translation stage that moves them in and out of the axis. The vertical axis serves three purposes: 1) as a vertical MOT beam when the mirror and the quarter wave plate are on axis, 2) as the axis for the microtrap when the mirror and the quarter wave plate are off the axis, and 3) as the single atom detection axis, when the mirror and the quarter waveplate are off the axis and the small MOT is on.

7.10 Future outlook

7.10.1 Culling Parameters

Figure 7.27 shows the results of a WKB calculation. The maximum fidelity that we can obtain with the current vacuum pressure is around 99.7. Further improvement on the vacuum pressure and reducing the waist of the microtrap should allow us to go beyond 99.9%.

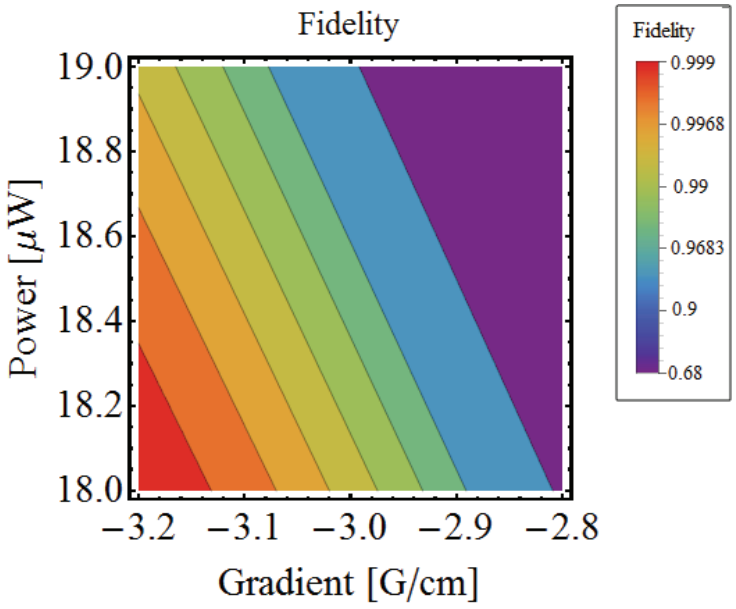

Figure 7.27: Contour plot of the probability of producing a single atom in the ground state of the microtrap after waiting long enough so that the ratio of the excited state occupancy probability to the ground state occupancy probability is 10^{-4}.

7.10.2 Single Atom Detection

Currently, the single atom detection signal is being optimized. The dark counts for our detection system are around 300 counts/second, while the background noise is between $3 \cdot 10^4$ and $7 \cdot 10^4$ counts/second. Based on the geometrical setup and small MOT beam parameters, we expect around 10^4 counts/second·atom. Once we achieve a signal of around 10^4 counts/second·atom we can start optimizing the culling process.

7.10.3 Scalability to N pairs

Scaling the production of a pair to multiple pairs can be done by means of painted potentials [45]. A single axis acousto-optic deflector can be used to generate a linear array of N traps by multiplexing different modulating its crystal with different radio frequencies. The main advantage of multiplexing the frequencies rather than applying all of them at the same time, is that the spots can be put arbitrarily close without worrying for interference. Figure 7.28 (7.29) shows how two (four) optical dipole traps can be generated by multiplexing two (four) frequencies into an acousto-optic deflector.

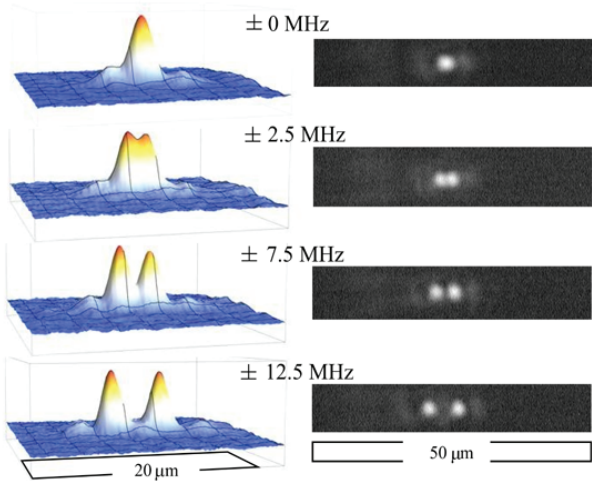

Figure 7.28: Scaling to N traps. A single axis acousto-optic deflector (AOD) can be used to generate N microtraps. The figure shows two spots being generated by multiplexing two different frequencies into the AOD. *Figure courtesy of Felix Schmidt.*

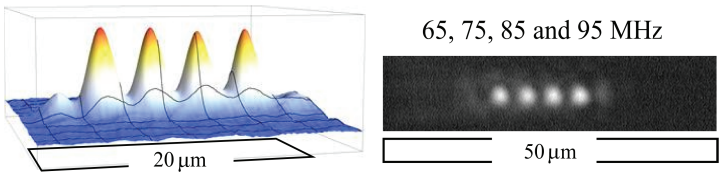

Figure 7.29: Scaling to N traps. A single axis acousto-optic deflector (AOD) can be used to generate N microtraps. The figure shows four spots being generated by multiplexing four different frequencies into the AOD. *Figure courtesy of Felix Schmidt.*

7.10.4 Future Studies

With the capability of producing N pairs of atoms in the ground state of N microtraps, one can further split the N microtrap into 2N microtraps and have 2N atoms in the ground state of 2N microtraps. Furthermore, if one uses a 2 axis electro optic deflector (which is faster than acousto-optic deflectors), one can generate as many as 81 dipole traps and can arrange them in any desired geometry. This would enable to study from single to many-body quantum phenomena like many-body tunneling. Using Feshbach resonances, one can tune the interactions between the atoms and simulate Hubbard-like Hamiltonians, or one can use Raman pulses to implement quantum gate operations and perform quantum computing [46].

Appendix

Appendix A

Angular Momentum Identities

The convention used here is the same as in ***Angular Momentum in Quantum Mechanics***, by A. R. Edmonds [47]; ***Quantum Mechanics: Fundamentals***, by Kurt Gottfried and Tung Mow Yang.

Wigner-Eckart Theorem

$$\begin{aligned} \langle \gamma' j' m' | \, \hat{\mathbf{T}}^k_q \, | \gamma j m \rangle &= \langle jk; mq | jk; j'm' \rangle \, \frac{\left\langle \gamma' j' || \hat{\mathbf{T}}^k || \gamma j \right\rangle}{\sqrt{2j'+1}} \qquad \text{(A.1)} \\ &= (-1)^{j'-m'} \begin{pmatrix} j' & k & j \\ -m' & q & m \end{pmatrix} \left\langle \gamma' j' || \hat{\mathbf{T}}^k || \gamma j \right\rangle \qquad \text{(A.2)} \end{aligned}$$

Wigner 3-j symbol:

$$\begin{pmatrix} j_1 & j_2 & j_3 \\ m_1 & m_2 & -m_3 \end{pmatrix} = \frac{(-1)^{j_1 - j_2 + m_3}}{\sqrt{2j_3+1}} \langle j_1 j_2; m_1 m_2 | j_1 j_2; j_3 m_3 \rangle \qquad \text{(A.3)}$$

Properties of the Wigner 3-j symbols

Even permutations leave the 3-j symbol unchanged,

$$\begin{pmatrix} j_1 & j_2 & j_3 \\ m_1 & m_2 & m_3 \end{pmatrix} = \begin{pmatrix} j_2 & j_3 & j_1 \\ m_2 & m_3 & m_1 \end{pmatrix} = \begin{pmatrix} j_3 & j_1 & j_2 \\ m_3 & m_1 & m_2 \end{pmatrix} \qquad \text{(A.4)}$$

Odd permutations introduce a factor of

$$(-1)^{j_1+j_2+j_3} \begin{pmatrix} j_1 & j_2 & j_3 \\ m_1 & m_2 & m_3 \end{pmatrix} = \begin{pmatrix} j_2 & j_1 & j_3 \\ m_2 & m_1 & m_3 \end{pmatrix} = \begin{pmatrix} j_1 & j_3 & j_2 \\ m_1 & m_3 & m_2 \end{pmatrix} = \begin{pmatrix} j_3 & j_2 & j_1 \\ m_3 & m_2 & m_1 \end{pmatrix} \qquad \text{(A.5)}$$

Orthogonality relations

$$\sum_{j_3 m_3} (2j_3+1) \begin{pmatrix} j_1 & j_2 & j_3 \\ m_1 & m_2 & m_3 \end{pmatrix} \begin{pmatrix} j_1 & j_2 & j_3 \\ m'_1 & m'_2 & m_3 \end{pmatrix} = \delta_{m_1 m'_1} \delta_{m_2 m'_2} \qquad \text{(A.6)}$$

$$\sum_{m_1 m_2} \begin{pmatrix} j_1 & j_2 & j_3 \\ m_1 & m_2 & m_3 \end{pmatrix} \begin{pmatrix} j_1 & j_2 & j_3' \\ m_1 & m_2 & m_3' \end{pmatrix} = \frac{1}{2j_3+1} \delta_{j_3 j_3'} \delta_{m_3 m_3'} \delta(j_1 j_2 j_3) \tag{A.7}$$

where $\delta(j_1 j_2 j_3)$ is the triangular condition, which is met if $j_3 = j_1 + j_2$

Wigner 6-j symbol

Wigner 6-j symbols allow us to decouple (factor) angular momentum components from the reduced matrix element. If $\hat{\mathbf{J}} = \hat{\mathbf{j}}_1 + \hat{\mathbf{j}}_2$, and $\hat{\mathbf{T}}^q_k$ acts only on $\hat{\mathbf{j}}_1$ to give a new $\hat{\mathbf{J}}' = \hat{\mathbf{j}}_1' + \hat{\mathbf{j}}_2$, as for example, the electric dipole operator acts only on $\hat{\mathbf{J}}$ in $\hat{\mathbf{F}} = \hat{\mathbf{J}} + \hat{\mathbf{I}}$, and only on $\hat{\mathbf{L}}$ in $\hat{\mathbf{J}} = \hat{\mathbf{L}} + \hat{\mathbf{S}}$.

$$\begin{aligned} \left\langle \gamma'(j_1' j_2) J' || \hat{\mathbf{T}}^k || \gamma(j_1 j_2) J \right\rangle =& (-1)^{j_1' + j_2 + J + k} \sqrt{(2J+1)(2J'+1)} \\ & \begin{Bmatrix} j_1' & J' & j_2 \\ J & j_1 & k \end{Bmatrix} \left\langle \gamma'(j_1' j_2) J' || \hat{\mathbf{T}}^k || \gamma(j_1 j_2) J \right\rangle \end{aligned} \tag{A.8}$$

Orthogonality Relation for Wigner 6-j Symbols

$$\sum_j (2j+1)(2j''+1) \begin{Bmatrix} j_1 & j_2 & j' \\ j_3 & j_4 & j \end{Bmatrix} \begin{Bmatrix} j_3 & j_2 & j \\ j_1 & j_4 & j'' \end{Bmatrix} = \delta_{j' j''} \tag{A.9}$$

Appendix B

Maxwell-Bloch Equations

B.1 Near resonant atom-light interactions

In this section I will discuss the theory of the interaction of atoms with near resonant light. Since we will be dealing with a large number of photons, the light fields can be treated classically. These photons, however, are near resonant and the atom-photon interaction must be treated quantum mechanically. Therefore, I will use a semi-classical framework to describe the interaction of atoms with near-resonant light. The equations that govern the interaction of near-resonant light with atoms are the optical Bloch equations, also known as the Maxwell-Bloch equations.

The treatment presented here is not complete – only the results relevant for this thesis will be derived. For a more complete treatment of the problem, see [27], [48], [26], and [49].

B.1.1 The Maxwell-Bloch equations

In deriving the Maxwell-Bloch equations, I will make use of the following approximations,

- **Two-level atom approximation**. I will assume that our atom has only 2 non-degenerate states: a ground state $|g\rangle$, and an excited state $|e\rangle$, whose energies differ by $\hbar\omega_0$.
- **Classical fields (semi-classical) approximation.** Since we are dealing with a large number of photons, we can write the electric field as $\vec{\mathbf{E}} = \hat{\epsilon}\widetilde{E}\cos(\vec{\mathbf{k}}\cdot\vec{\mathbf{r}} - \omega t)$, where $\widetilde{E}$ is a complex amplitude, $\hat{\epsilon}$ is a polarization vector, and the real electric field is the real part of $\vec{\mathbf{E}}$.

- **Electric dipole approximation**. I will assume that our atoms are smaller (< 1 nm) than the wavelength of the light field (671 nm), so we may regard the electric field as nearly constant within the region in which the atomic wavefunctions are peaked.

- **Rotating wave approximation**. I will neglect terms that vary as $e^{i(\omega+\omega_0)t}$ compared to $e^{i(\omega-\omega_0)t}$, where ω and ω_0 are optical frequencies.

If energy of the ground state is defined as zero, then the wavefunction of a two-level system can be written as,

$$|\mathbf{\Psi}(\vec{\mathbf{r}},t)\rangle = c_g(t)\,|g\rangle + c_e(t)e^{-i\omega_0 t}\,|e\rangle \tag{B.1}$$

- make diagram

where $\hbar\omega_0$ is the energy difference between the ground and excited states. We wish to find how the coefficients $c_g(t)$ and $c_e(t)$ change in time due to the Hamiltonian: $\hat{H} = \hat{H}_0 + \hat{V}$, where $\hat{H}_0$ is the Hamiltonian of the unperturbed atom with eigenstates $|g\rangle$ and $|e\rangle$, and $\hat{V} = -e\hat{r}\cdot\vec{\mathbf{E}}$, where e is the charge of the particle, not necesarily that of the electron. Substituting the wavefunction (B.1) into Schrödinger's equation (B.2),

$$i\hbar\frac{\partial\mathbf{\Psi}(\vec{\mathbf{r}},t)}{\partial t} = \hat{H}\mathbf{\Psi}(\vec{\mathbf{r}},t) \tag{B.2}$$

yields two coupled differential equations for the coefficients $c_g(t)$ and $c_e(t)$,

$$i\hbar\frac{dc_e}{dt} = c_g\,\langle e|\,\hat{V}\,|g\rangle\,e^{i\omega_0 t} \tag{B.3}$$

$$i\hbar\frac{dc_g}{dt} = c_e\,\langle g|\,\hat{V}\,|e\rangle\,e^{-i\omega_0 t} \tag{B.4}$$

were

$$V_{eg} = \langle e|\,\hat{V}\,|g\rangle = \langle e|\,-e\vec{\mathbf{r}}\cdot\vec{\mathbf{E}}\,|g\rangle = \langle e|\,-e\vec{\mathbf{r}}\cdot\hat{\epsilon}\widetilde{E}\cos\left(\vec{\mathbf{k}}\cdot\vec{\mathbf{r}}-\omega t\right)|g\rangle \tag{B.5}$$

After using the electric dipole approximation,

$$V_{eg} = \widetilde{E}\cos\left(\vec{\mathbf{k}}\cdot\vec{\mathbf{r_0}}-\omega t\right)\langle e|\,-e\vec{\mathbf{r}}\cdot\hat{\epsilon}\,|g\rangle \tag{B.6}$$

where $\vec{\mathbf{r}}_0$ is at the position of the atom, which without loss of generality we can set to the origin, thus

$$V_{eg} = V_{ge}^* = \langle e| \hat{V} |g\rangle = \widetilde{E}\hat{\mu}_{eg} \cos(\omega t) = \hbar\Omega \cos \omega t \tag{B.7}$$

with,

$$\hat{\mu}_{eg} \equiv \langle e| - e\vec{\mathbf{r}} \cdot \hat{\epsilon} \, |g\rangle \tag{B.8}$$

and,

$$\Omega \equiv \frac{\widetilde{E}}{\hbar} \langle e| - e\vec{\mathbf{r}} \cdot \hat{\epsilon} \, |g\rangle \tag{B.9}$$

$\hat{\mu}_{eg}$ is the electric dipole matrix coefficient, and Ω is called the "Rabi Frequency". Note, however, that Ω is a complex number! The actual Rabi frequency is $|\Omega|$. Substituting equation (B.7) into equations (B.4) and (B.3) and using the complex form of cosine, we get

$$i\hbar \frac{dc_e}{dt} = c_g \hbar\Omega \left(\frac{e^{i(\omega+\omega_0)t} + e^{-i(\omega-\omega_0)t}}{2} \right) \tag{B.10}$$

$$i\hbar \frac{dc_g}{dt} = c_e \hbar\Omega^* \left(\frac{e^{i(\omega-\omega_0)t} + e^{-i(\omega+\omega_0)t}}{2} \right) \tag{B.11}$$

Using the Rotating Wave Approximation, the equations simplify to

$$i\hbar \frac{dc_e}{dt} = c_g \hbar\Omega \frac{e^{-i\delta t}}{2} \tag{B.12}$$

$$i\hbar \frac{dc_g}{dt} = c_e \hbar\Omega^* \frac{e^{i\delta t}}{2} \tag{B.13}$$

Now, the coefficients $c_g(t)$ and $c_e(t)$ change in time due to both parts of the Hamiltonian, $\hat{H}$ and $\hat{V}$. To isolate the time evolution due solely to $\hat{V}$, we transform to the rotating frame. We set $c'_g(t) \equiv c_g(t)$ and $c'_e(t) \equiv c_e(t)e^{+i\delta t}$, so equations (B.12) and (B.13) become

$$i\hbar \frac{d}{dt} \begin{pmatrix} c'_e \\ c'_g \end{pmatrix} = \frac{\hbar}{2} \begin{pmatrix} -2\delta & \Omega \\ \Omega^* & 0 \end{pmatrix} \begin{pmatrix} c'_e \\ c'_g \end{pmatrix} \tag{B.14}$$

$$\hat{H}' = \frac{\hbar}{2} \begin{pmatrix} -2\delta & \Omega \\ \Omega^* & 0 \end{pmatrix} \tag{B.15}$$

where $\hat{H}'$ is an effective Hamiltonian that captures the time evolution due only to $\hat{V}$. Although equation (B.14) captures all the dynamics induced by the interaction Hamiltonian $\hat{V}$, it does not take into account spontaneous emission. Moreover, equation (B.14) describes the evolution of a pure state; spontaneous emission, however, turns pure states into statistical mixtures. Therefore, we must retort to the density matrix formalism [50] if we wish to incorporate spontaneous emission into our analysis. The density matrix is a quantum mechanical operator that can describe both pure and mixed states. For a 2-level system mixed state, the density matrix in the rotating frame can be written as,

$$\hat{\widetilde{\rho}} = \begin{pmatrix} \widetilde{\rho}_{ee} & \widetilde{\rho}_{eg} \\ \widetilde{\rho}_{ge} & \widetilde{\rho}_{gg} \end{pmatrix} \tag{B.16}$$

For a pure state, $\widetilde{\rho}_{ij} = \widetilde{c}_i \widetilde{c}_j^*$

$$\hat{\widetilde{\rho}} = \begin{pmatrix} \widetilde{\rho}_{ee} & \widetilde{\rho}_{eg} \\ \widetilde{\rho}_{ge} & \widetilde{\rho}_{gg} \end{pmatrix} = \begin{pmatrix} \widetilde{c}_e \widetilde{c}_e^* & \widetilde{c}_e \widetilde{c}_g^* \\ \widetilde{c}_g \widetilde{c}_e^* & \widetilde{c}_g \widetilde{c}_g^* \end{pmatrix} \tag{B.17}$$

Combining equations (B.17) and (B.14), we get

$$\frac{d\hat{\widetilde{\rho}}}{dt} = \frac{i}{\hbar}\left[\hat{\widetilde{\rho}}, \hat{H}\right] \tag{B.18}$$

We can now include the effect of spontaneous emission by adding the following term to equation (B.18),

$$\frac{d}{dt}\begin{pmatrix} \widetilde{\rho}_{ee} & \widetilde{\rho}_{ge} \\ \widetilde{\rho}_{eg} & \widetilde{\rho}_{ee} \end{pmatrix}_{spont} = \begin{pmatrix} -\gamma\widetilde{\rho}_{ee} & -\frac{\gamma}{2}\widetilde{\rho}_{ge} \\ -\frac{\gamma}{2}\widetilde{\rho}_{eg} & \gamma\widetilde{\rho}_{ee} \end{pmatrix} \tag{B.19}$$

where γ[1] is the natural decay rate, given by

$$\gamma = \frac{\omega_0^3 \mu^2}{3\pi\epsilon_0 \hbar c^3} \tag{B.20}$$

and the lifetime of the transition is

$$\tau \equiv 1/\gamma \tag{B.21}$$

[1]Note that the units of γ are s^{-1}, while the units of Γ are Hz. γ, with units s^{-1}, should be used when dealing with scattering rates and lifetimes. While Γ, in units of Hz, should be used when dealing with detunings and line broadenings.

Equation (B.18) becomes,

$$\frac{d\hat{\widetilde{\rho}}}{dt} = \frac{i}{\hbar}\left[\hat{\widetilde{\rho}}, \hat{H}\right] - \begin{pmatrix} \gamma\widetilde{\rho}_{ee} & \frac{\gamma}{2}\widetilde{\rho}_{ge} \\ \frac{\gamma}{2}\widetilde{\rho}_{eg} & -\gamma\widetilde{\rho}_{ee} \end{pmatrix} \tag{B.22}$$

whose components are known as the **Maxwell-Bloch** equations:

$$\dot{\widetilde{\rho}}_{ee} = -\frac{i}{2}(\Omega\widetilde{\rho}_{ge} - \Omega^*\widetilde{\rho}_{eg}) - \gamma\widetilde{\rho}_{ee} \tag{B.23}$$

$$\dot{\widetilde{\rho}}_{gg} = \frac{i}{2}(\Omega\widetilde{\rho}_{ge} - \Omega^*\widetilde{\rho}_{eg}) + \gamma\widetilde{\rho}_{ee} \tag{B.24}$$

$$\dot{\widetilde{\rho}}_{ge} = -\frac{i\Omega^*}{2}(\widetilde{\rho}_{ee} - \widetilde{\rho}_{gg}) - i\delta\widetilde{\rho}_{ge} - \frac{\gamma}{2}\widetilde{\rho}_{ge} \tag{B.25}$$

$$\dot{\widetilde{\rho}}_{eg} = \frac{i\Omega}{2}(\widetilde{\rho}_{ee} - \widetilde{\rho}_{gg}) + i\delta\widetilde{\rho}_{eg} - \frac{\gamma}{2}\widetilde{\rho}_{eg} \tag{B.26}$$

Defining $w \equiv \widetilde{\rho}_{gg} - \widetilde{\rho}_{ee}$, and using $\widetilde{\rho}_{gg} + \widetilde{\rho}_{ee} = 1$, we find the steady state solutions

$$\widetilde{\rho}_{ee} = \frac{s}{2(1+s)} \tag{B.27}$$

$$\widetilde{\rho}_{eg} = \frac{-i\Omega}{2(\gamma/2 - i\delta)}\frac{1}{1+s} \tag{B.28}$$

$$w = \frac{1}{1+s} \tag{B.29}$$

where,

$$s \equiv \frac{|\Omega|^2/2}{\delta^2 + \gamma^2/4} = \frac{2|\Omega|^2/\gamma^2}{1 + (2\delta/\gamma)^2} = \frac{s_0}{1 + (2\delta/\gamma)^2} \tag{B.30}$$

with

$$s_0 \equiv 2|\Omega|^2/\gamma^2 = I/I_{sat} \tag{B.31}$$

$$I_{sat} \equiv \frac{2\pi^2\hbar\gamma c}{3\lambda_0^3} \tag{B.32}$$

s is called the *saturation parameter*, and s_0 the *on-resonance saturation parameter*. I_{sat} is called the saturation intensity; it defines the on-resonance intensity level at which the transition starts to saturate. λ_0 is the on resonance transition's wavelength.

B.1.2 Near-resonant forces on atoms

The force exerted by near-resonant light on an ensemble of atoms can be calculated using Eherenfest's theorem,

$$F = \left\langle \hat{\mathbf{F}} \right\rangle = \left\langle \frac{d\hat{\mathbf{p}}}{dt} \right\rangle \tag{B.33}$$

using

$$\frac{d\hat{\mathbf{p}}}{dt} = \frac{i}{\hbar}\left[\hat{\mathbf{H}}, \hat{\mathbf{p}}\right] \tag{B.34}$$

and

$$\left[\hat{\mathbf{H}}, \hat{\mathbf{p}}\right] = i\hbar\frac{\partial\hat{\mathbf{H}}}{\partial z} \tag{B.35}$$

we get

$$F = -\left\langle\frac{\partial\hat{\mathbf{H}}}{\partial z}\right\rangle = -\mathrm{Tr}\left[\widetilde{\rho}\frac{\partial\hat{V}}{\partial z}\right] = -\left(\widetilde{\rho}_{ge}\frac{\partial\hat{\widetilde{V}}_{eg}}{\partial z} + \widetilde{\rho}_{eg}\frac{\partial\hat{\widetilde{V}}_{ge}}{\partial z}\right) \tag{B.36}$$

in the rotating frame,

$$\hat{\widetilde{V}}_{eg} = \hat{V}_{eg}e^{i\omega t} = \frac{1}{2}\widetilde{E}\mu_{eg} = \frac{1}{2}\hbar\Omega \tag{B.37}$$

where (B.7) has been used and the positive term $e^{i\omega t}$ has been discarded due to the rotating wave approximation. If we now let the complex amplitude $\widetilde{E}$ have the form,

$$\widetilde{E} = \widetilde{E}(z) = E(z)e^{ikz} \tag{B.38}$$

where $E(z)$ is a real amplitude, we can subsitute the solution for $\widetilde{\rho}_{eg}$ (equation (B.28)), equation (B.38), and equation (B.37) into (B.36), to get (after some tedious algebra)

$$F = \frac{\hbar}{2}\frac{1}{(1 + I/I_{sat} + (2\delta/\gamma)^2)}\left(k\gamma\frac{I}{I_{sat}} - \delta\frac{\partial}{\partial z}\left(\frac{I}{I_{sat}}\right)\right) \tag{B.39}$$

From which the results,

$$F_{scatt} = \frac{\hbar k\gamma}{2}\frac{I/I_{sat}}{(1 + I/I_{sat} + (2\delta/\gamma)^2} \tag{B.40}$$

$$F_{dipole} = -\frac{\hbar\delta}{2}\frac{1}{(1 + I/I_{sat} + (2\delta/\gamma)^2)}\frac{1}{I_{sat}}\frac{\partial I}{\partial z} \tag{B.41}$$

$$U_{dipole} = \frac{\hbar\delta}{2}\ln\left(1 + I/I_{sat} + (2\delta/\gamma)^2\right) \tag{B.42}$$

can be derived.

Appendix C

Propagation of the electric field through the atomic cloud

First, an expression for the macroscopic electric susceptibility in terms of microscopic quantities will be derived. Then, the differential equation for the attenuation of the electric field of a near resonant beam passing through a medium composed of two-level atoms will be derived.

C.0.3 Electrical Susceptibility of an ensemble of two-level atoms

The macroscopic complex polarization amplitude of our two-level system can be written as,

$$\widetilde{P} = \epsilon_0 \chi \widetilde{E} \tag{C.1}$$

where both χ and $\widetilde{E}$ are complex quantities. The actual polarization being the real part of $\widetilde{P}$.

$$P = \frac{1}{2}\epsilon_0 \chi \widetilde{E} + \frac{1}{2}\epsilon_0 \chi^* \widetilde{E}^* \tag{C.2}$$

From a microscopic point of view the polarization is just

$$P = ne \left\langle \vec{\mathbf{r}} \cdot \hat{\epsilon} \right\rangle, \tag{C.3}$$

where the average denotes a statistical average. Using equation (2.24), we can rewrite this as

$$P = -n \left\langle \mu \right\rangle = -n\mathbf{Tr}[\widetilde{\rho}\mu] = -n\mu_{eg}\widetilde{\rho}_{ge} - n\mu_{ge}\widetilde{\rho}_{eg}$$

$$P = \frac{in\mu_{ge}}{2}\frac{\widetilde{E}\mu_{eg}/\hbar}{(\gamma/2 - i\delta)}\frac{1}{1+s} - \frac{in\mu_{eg}}{2}\frac{\widetilde{E}^*\mu_{ge}/\hbar}{(\gamma/2 + i\delta)}\frac{1}{1+s} \tag{C.4}$$

comparing equations (C.4) and (C.2), we see that

$$\chi = \frac{in\left|\mu_{eg}\right|^2}{\epsilon_0 \hbar(\gamma/2)}\frac{(1 + i(2\delta/\gamma))}{(1 + (2\delta/\gamma)^2)}\frac{1}{1+s} \tag{C.5}$$

using (2.36)

$$\chi = \frac{in\sigma(\delta)}{k}\left(\frac{1+i(2\delta/\gamma)}{1+s}\right) \tag{C.6}$$

C.0.4 Propagation of an electric field through a medium

The wave equation for an electromagnetic wave propagating through a medium is,

$$\nabla^2\vec{\widetilde{\mathbf{E}}} - \frac{1}{c^2}\frac{\partial^2\vec{\widetilde{\mathbf{E}}}}{\partial t^2} = \mu_0\frac{\partial^2\vec{\widetilde{\mathbf{P}}}}{\partial t^2} \tag{C.7}$$

making the slow varying amplitude approximation, we can write the electric field as,

$$\vec{\widetilde{\mathbf{E}}} = \hat{\epsilon}\widetilde{E}(z)e^{(\vec{\mathbf{k}}\cdot\vec{\mathbf{r}}-\omega t)} \tag{C.8}$$

Substituting equation (C.8) into equation (C.7), using $\vec{\widetilde{\mathbf{P}}} = \epsilon_0\chi\vec{\widetilde{\mathbf{E}}}$, and keeping only first order derivatives, we get,

$$\frac{\partial\widetilde{E}(z)}{\partial z} = \frac{1}{2}ik\chi\widetilde{E}(z) \tag{C.9}$$

which can be split into two parts,

$$\frac{\partial\widetilde{E}(z)}{\partial z} = -\frac{1}{2}(\kappa(\delta,s)+i\phi(\delta,s))\widetilde{E}(z) \tag{C.10}$$

where $\kappa(\delta,s)$ and $\phi(\delta,s)$ are the absorption and dispersion coefficients respectively, and are given by:

$$\kappa(\delta,s) = \left(\frac{n\sigma_0}{1+s}\right)\frac{1}{1+(2\delta/\gamma)^2} \tag{C.11}$$

$$\phi(\delta,s) = \left(\frac{n\sigma_0}{1+s}\right)\frac{(2\delta/\gamma)}{1+(2\delta/\gamma)^2} \tag{C.12}$$

Equation C.9 can be rewritten as,

$$\frac{\partial\widetilde{E}(x,y,z)}{\partial z} = -\frac{n\sigma(\delta)}{2}\left(\frac{1+i(2\delta/\gamma)}{1+s}\right)\widetilde{E}(x,y,z) \tag{C.13}$$

where

$$\sigma(\delta) = \frac{\sigma_0}{1+(2\delta/\gamma)^2} \tag{C.14}$$

When the intensity is well below the saturation intensity, $s \ll 1$, then equation (C.13) reduces to,

$$\frac{\partial\widetilde{E}(x,y,z)}{\partial z} = -\frac{n\sigma(\delta)}{2}(1+i(2\delta/\gamma))\widetilde{E}(x,y,z) \tag{C.15}$$

Multiplying by $\widetilde{E}^*$ both sides of equation (C.13), and adding it its own complex conjugate, we get Beer's law:

$$\frac{\partial I}{\partial z} = -n\sigma(\delta)I \tag{C.16}$$

Bibliography

[1] Antikythera. The antikythera mechanisms research project. http://www.antikythera-mechanism.gr/project/overview.

[2] Anders W. Sandvik. Ground states of a frustrated quantum spin chain with long-range interactions. *Phys. Rev. Lett.*, 104:137204, Mar 2010.

[3] T.D. Ladd, F. Jelezko, R. Laflamme, Y. Nakamura, C. Monroe, and J.L. O'Brien. Quantum computers. *Nature*, 464:45, 2010.

[4] Joseph W. et. al. Britton. Engineered two-dimensional ising interactions in a trapped-ion quantum simulator with hundreds of spins. *Nature*, 484:489–492, 2012.

[5] B. E. Kane. A silicon-based nuclear spin quantum computer. *Nature*, 393:133, 1998.

[6] C. Monroe. Quantum information processing with atoms and photons. *Nature*, 416:238, 2002.

[7] D. P. DiVicenzo. The physical implementation of quantum computation. *Fortschritte der Physik*, 48:771, 2000.

[8] D.R. Lide (Ed.). *CRC Handbook of Chemistry and Physics*. CRC Press, Boca Raton, 79th edition, 1998.

[9] C.B. Alcock, V.P. Itkin, and M.K. Horrigan. Vapor pressure equations for the metallic elements: 298 2500 k. *Canadian Metallurgical Quarterly*, 23:309, 1984.

[10] I. Mills, T. Cvitas, K. Homann, N. Kallay, and K. Kuchitsu. *Quantities, Units, and Symbols in Physical Chemistry*. Blackwell Scientific Publishing, Oxford, 1988.

[11] J. Walls, R. Ashby, J.J. Clarke, B. Lu, and W.A. van Wijngaarden. Measurement of isotope shifts, fine and hyperfine structure splittings of the lithium d lines. *The*

European Physical Journal D - Atomic, Molecular, Optical and Plasma Physics, 22(2):159–162, 2003.

[12] M.E. Gehm. Properties of ^{6}Li. physics.ncsu.edu/ jet/techdocs/pdf/ PropertiesOfLi.pdf, February 2003.

[13] Scherf, W. and Khait, O. and Jager, H. and Windholz, L. Re-measurement of the transition frequencies, fine structure splitting and isotope shift of the resonance lines of lithium, sodium and potassium. *Zeitschrift für Physik D Atoms, Molecules and Clusters*, 36(1):31–33, 1996.

[14] W. I. McAlexander, E. R. I. Abraham, R. G. Hulet. Radiative lifetime of the $2p$ state of lithium. *Phys. Rev. A*, 54:R5–R8, Jul 1996.

[15] Arimondo, E. and Inguscio, M. and Violino, P. Experimental determinations of the hyperfine structure in the alkali atoms. *Rev. Mod. Phys.*, 49:31–75, Jan 1977.

[16] Peter J. Mohr, Barry N. Taylor, and David B. Newell. CODATA recommended values of the fundamental physical constants: 2010. *Rev. Mod. Phys.*, 84:1527–1605, Nov 2012.

[17] C. Chin, R. Grimm, P.S. Julienne, and E. Tiesinga. Feshbach resonances in ultracold gases. *Rev. Mod. Phys.*, 82:1225, 2010.

[18] M. Houbiers, H.T.C. Stoof, W.I. McAlexander, and R.G. Hulet. Elastic and inelastic collisions of ^{6}Li atoms in magnetic and optical traps. *Phys. Rev. A*, 57:R1497, 1998.

[19] M. Bartenstein, A. Altmeyer, S. Riedl, R. Geursen, S. Jochim, C. Chin, J. Hecker Denschlag, R. Grimm, A. Simoni, E. Tiesinga, C.J. and Williams, and P.S. Julienne. Precise determination of ^{6}Li cold collision parameters by radio-frequency spectroscopy on weakly bound molecules. *Phys. Rev. Lett.*, 94:103201, 2005.

[20] T.B. Ottenstein. *Few-body physics in ultracold Fermi gases.* PhD thesis, University of Heidelberg, 2010.

[21] R. Grimm, M. Weidemueller, and Y.B. Ovchinnikov. Optical dipole traps for neutral atoms. *Adv. At., Mol. and Opt. Phys.*, 42:95, 2000.

[22] K. Huang. *Statistical Mechanics.* John Wiley and Sons, 1987.

[23] Pethick, C. J.; Smith, H. *Bose-Einstein Condensation in Dilute Gases.* Cambridge University Press, Cambridge, 2002.

[24] G.C. Bjorklund, M.D. Levenson, W. Lenth, and C. Ortiz. Frequency modulation (fm) spectroscopy. *Appl. Phys. B*, 32:145, 1983.

[25] U. Schuenemann, H. Engler, R. Grimm, M. Weidemueller, and M. Zielonkowski. Simple scheme for tunable frequency offset locking of two lasers. *Rev. of Sci. Instr.*, 70:242, 1999.

[26] Christopher J. Foot. *Atomic Physics.* Oxford University Press, Inc., New York, 2005.

[27] Metcalf, Harold J.; van der Straten, Peter. *Laser cooling and trapping.* Springer, New York, 1999.

[28] S.R. Granade, M.E. Gehm, K.M. O'Hara, and J.E. Thomas. All-Optical Production of a Degenerate Fermi Gas. *Phys. Rev. Lett.*, 88:120405, 2002.

[29] K.M. O'Hara, M.E. Gehm, S.R. Granade, and J.E. Thomas. Scaling laws for evaporative cooling in time-dependent optical traps. *Phys. Rev. A*, 64:051403, 2001.

[30] L. Luo, B. Clancy, J. Joseph, J. Kinast, A. Turlapov, and J.E. Thomas. Evaporative cooling of unitary Fermi gas mixtures in optical traps. *New Jour. Phys.*, 8:213, 2006.

[31] A.M. Dudarev, M.G. Raizen, and Q. Niu. Quantum Many-Body Culling: Production of a Definite Number of Ground-State Atoms in a Bose-Einstein Condensate. *Phys. Rev. Lett.*, 98:063001, 2007.

[32] M. Pons, A. del Campo, J.G. Muga, and M.G. Raizen. Preparation of atomic Fock states by trap reduction. *Phys. Rev. A*, 79:033629, 2009.

[33] M.G. Raizen, S.-P. Wan, C. Zhang, and Q. Niu. Ultrahigh-fidelity qubits for quantum computing. *Phys. Rev. A*, 80:030302, 2009.

[34] F. Serwane, G. Zuern, T. Lompe, T.B. Ottenstein, A.N. Wenz, and S. Jochim. Deterministic Preparation of a Tunable Few-Fermion System. *Science*, 332:336, 2011.

[35] Eugen Merzbacher. *Quantum Mechanics*. Wiley, Reading, 1997.

[36] W. Ketterle, D. S. Durfee, and D. M. Stamper-Kurn. Making, probing and understanding Bose-Einstein condensates. *eprint arXiv:cond-mat/9904034*, April 1999.

[37] Kirsten Viering. *Experiments to Control Atom Number and Phase-Space Density in Cold Gases*. PhD thesis, The University of Texas at Austin, 2012.

[38] John Thomas's group. A mathematica program to simulate magnetic fields produced by coils.

[39] Selim Jochim's group. A matlab program to simulate cooling in the zeeman slower.

[40] F. Schreck. iqoqi006.uibk.ac.at/users/c704250.

[41] K.M. O'Hara, S.R. Granade, M.E. Gehm, T.A. Savard, S. Bali, C. Freed, and J.E. Thomas. Ultrastable CO_2 Laser Trapping of Lithium Fermions. *Phys. Rev. Lett.*, 82:4204, 1999.

[42] Viering Kirsten, Medellin David, Mo Jianyong, M.G. Raizen. Atomic laser-beam finder. *Opt. Express*, 20(23):25590–25595, Nov 2012.

[43] T. A. Savard, K. M. O'Hara, and J. E. Thomas. Laser-noise-induced heating in far-off resonance optical traps. *Phys. Rev. A*, 56:R1095–R1098, Aug 1997.

[44] C.-S. Chuu, F. Schreck, T.P. Meyrath, J.L. Hanssen, G.N. Price, and M.G. Raizen. Direct observation of sub-poissonian number statistics in a degenerate bose gas. *Phys. Rev. Lett.*, 95:260403, 2005.

[45] K. Henderson, C. Ryu, C. MacCormick, and M.G. Boshier. Experimental demonstration of painting arbitrary and dynamic potentials for Bose-Einstein condensates. *New Jour. Phys.*, 11:043030, 2009.

[46] Adriano Barenco, Charles H. Bennett, Richard Cleve, David P. DiVincenzo, Norman Margolus, Peter Shor, Tycho Sleator, John A. Smolin, and Harald Weinfurter. Elementary gates for quantum computation. *Phys. Rev. A*, 52:3457–3467, Nov 1995.

[47] A.R. Edmonds. *Angular momentum in quantum mechanics.* Princeton University Press, Princeton, 1974.

[48] Miloni, Peter W.; Eberly, Joseph H. *Lasers.* Wiley, New York, 1988.

[49] Mitchel Weissbluth. *Photon-Atom Interaction.* Academic Press, Inc., San Diego, CA, 1989.

[50] J.J. Sakurai. *Modern Quantum Mechanics.* Addison Wesley, Reading, 1994.